UQAR Université du Québec à Rimouski

Analyse des performances mécaniques des joints soudés au laser sur des tôles en alliages d'aluminium AA5052 et AA6061

Thèse présentée

dans le cadre du programme de doctorat en ingénierie de l'UQAC,

offert par extension à I'UQAR,

en vue de l'obtention du grade de philosophiae doctor (Ph.D)

PAR

© Pedram Farhadipour

Juillet 2025

Composition du jury :

Marc-Denis Rioux, président du jury, Université du Québec à Rimouski

Noureddine Barka, directeur de recherche, Université du Québec à Rimouski

Abderrazak El Ouafi, codirecteur de recherche, Université du Québec à Rimouski

Sofiene Amira, examinateur externe, Centre québécois de recherche et de développement de l'aluminium (CQRDA)

Hendra Hermawan, examinateur externe, Université Laval

Dépôt initial le 11 Décembre 2024 Dépôt final le 21 Juillet 2025

REMERCIEMENTS

Cette thèse est le fruit de plus de quatre années de travail et de recherche intensifs, marquées par un apprentissage approfondi, des échanges d'informations et une étude extensive. Le parcours pour réaliser cette modeste thèse de recherche n'aurait pas été possible sans le soutien et les contributions de nombreuses personnes, auxquelles j'adresse ma plus profonde gratitude.

Tout d'abord, j'exprime mes sincères remerciements à mon directeur de recherche, le Professeur **Noureddine Barka**, de l'Université du Québec à Rimouski. Son encouragement, son soutien et ses conseils inestimables ont été déterminants pour guider ma recherche. Son énergie, sa passion pour l'innovation et sa poursuite incessante de l'excellence ont été une source constante de motivation, m'aidant à surmonter les défis et à atteindre mes objectifs.

Je tiens également à exprimer ma profonde gratitude au Professeur **Abderrazak El Ouafi**, mon codirecteur de l'Université du Québec à Rimouski. Ses conseils, ses idées et son soutien tout au long de ce processus de recherche ont été inestimables et ont grandement contribué au développement et à l'achèvement de cette thèse.

Je suis également profondément reconnaissant à Monsieur **François Nadeau** et à Monsieur **Mohamad Idriss**, chercheurs au Conseil national de recherches Canada (CNRC). Leur expérience industrielle et leur vision de la recherche ont considérablement enrichi ma perspective et contribué à l'avancement de mon travail.

Mes sincères remerciements vont à mes collègues du Laboratoire des Matériaux, Produits et Procédés de pointe (LMP3), en particulier Dr Narges Omidi et M. Asim Iltaf, pour leur aide dans la réalisation des travaux expérimentaux. Leur soutien et leur camaraderie ont été inestimables tout au long de ce parcours.

Des remerciements particuliers sont dus à mes parents et à mon frère. Leur amour indéfectible, leurs efforts, leur soutien et leurs encouragements ont été le pilier de ma motivation. Leur présence et leur foi en moi ont été indispensables, et je reconnais que je ne serais pas où je suis aujourd'hui sans eux.

Enfin, j'adresse ma profonde gratitude à toutes les autres personnes qui, bien que non mentionnées personnellement, ont contribué de manière significative à l'achèvement de cette thèse par leurs conseils et leurs diverses compétences. Votre soutien a été profondément apprécié.

RÉSUMÉ

L'objectif de cette recherche est d'optimiser les processus de soudage au laser et d'analyser le comportement mécanique des alliages d'aluminium pour l'automobile, AA5052 et AA6061, dans différentes conditions. L'étude est divisée en trois phases : optimisation des paramètres de soudage au laser à recouvrement avec oscillation pour des feuilles d'aluminium AA5052-H32 de différentes épaisseurs, examen du comportement de fracture des pièces soudées des deux côtés en Al6061-T6 à des températures élevées, et évaluation des propriétés de traction à haute température des alliages AA5052-H36 et AA6061-T6 soudés au laser pour des applications automobiles.

Dans la première phase, l'accent a été mis sur l'optimisation des paramètres de soudage au laser pour les feuilles AA5052-H32. Les paramètres étudiés comprenaient la puissance du laser, la vitesse de déplacement, la position de la lentille, la forme de l'oscillation et l'amplitude. Les résultats ont montré que le motif d'oscillation a un impact minimal sur la résistance mécanique, tandis que l'intensité de la puissance du laser est cruciale pour maintenir une efficacité de soudage supérieure à 89,9 %. Les mesures de microdureté ont efficacement détecté des défauts tels que la porosité et un apport thermique excessif. Les paramètres de soudage optimaux ont été déterminés comme suit : 2500 W pour la puissance du laser, 5 m/min pour la vitesse de déplacement, 6,0 mm pour la position de la lentille et 1,5 mm pour l'amplitude de l'oscillation.

La deuxième phase a étudié le comportement de fracture des pièces soudées en AA6061-T6 sous des charges de traction et des températures allant de la température ambiante à 200°C. L'analyse microstructurale a révélé une zone affectée par la chaleur (ZAC) en forme de H, séparant deux zones de fusion. La section centrale de la ZAC, caractérisée par de petits grains recristallisés, était particulièrement sujette à la microfissuration. La recherche a indiqué qu'à des températures supérieures à 150°C, ces microfissures initiaient des fissures dans la zone de fusion, tandis qu'à des températures plus basses, l'initiation des fissures est plus sensible aux défauts géométriques dans la ZAC. Ces résultats suggèrent que le comportement de fracture de l'AA6061-T6 est fortement dépendant de la température, avec des implications significatives pour son utilisation dans des applications à haute température.

La troisième phase a examiné les propriétés de traction à haute température des alliages AA5052-H36 et AA6061-T6 soudés au laser. Des tests de traction ont été réalisés à des températures de 25°C à 300°C avec des vitesses de déformation de 0,01 s^{-1} et 0,1 s^{-1}. L'AA5052-H36 a montré une résistance mécanique supérieure, avec une diminution linéaire de la résistance à la traction ultime (UTS) à mesure que la température augmentait, tandis que l'AA6061-T6 a présenté une réduction non linéaire de l'UTS due à des transformations de phases. L'analyse a révélé que l'AA5052-H36 a une meilleure capacité d'absorption d'énergie avant rupture jusqu'à 250°C, après quoi l'absorption d'énergie diminue considérablement, soulevant des préoccupations quant aux risques de défaillance liés au fluage.

En conclusion, cette recherche fournit des informations précieuses sur l'optimisation des paramètres de soudage au laser et la compréhension des performances mécaniques des alliages AA5052 et AA6061 dans différentes conditions thermiques. Les résultats mettent en évidence le rôle critique de la température dans la détermination de la pertinence de ces alliages pour des applications automobiles, notamment dans des environnements où les températures élevées et les charges de traction sont prévalentes. L'AA5052-H36 se révèle être une option plus robuste pour les charges de traction statiques à haute température, bien que l'utilisation de tout alliage au-dessus de 250°C nécessite une gestion prudente pour atténuer les risques de défaillances liées au fluage.

Mots clés : Soudage au laser, alliage d'aluminium, soudage à recouvrement, optimisation, soudure double face, microstructure, température élevée, fractographie

ABSTRACT

The objective of this research is to optimize laser welding processes and analyze the mechanical behavior of automotive aluminum alloys, AA5052 and AA6061, under different conditions. The study is divided into three phases: optimization of overlap laser welding parameters with oscillation for AA5052-H32 aluminum sheets of different thicknesses, examination of the fracture behavior of double-sided welded Al6061-T6 parts at high temperatures, and evaluation of the high-temperature tensile properties of laser-welded AA5052-H36 and AA6061-T6 alloys for automotive applications.

In the first phase, the focus was on optimizing laser welding parameters for AA5052-H32 sheets. The parameters studied included laser power, travel speed, lens position, oscillation shape, and amplitude. The results showed that the oscillation pattern had a minimal impact on mechanical strength, while laser power intensity was crucial in maintaining welding efficiency above 89.9%. Microhardness measurements effectively detected defects such as porosity and excessive heat input. The optimal welding parameters were determined as follows: 2500 W for laser power, 5 m/min for travel speed, 6.0 mm for lens position, and 1.5 mm for oscillation amplitude.

The second phase investigated the fracture behavior of AA6061-T6 welded parts under tensile loads and temperatures ranging from room temperature to 200°C. Microstructural analysis revealed an H-shaped heat-affected zone (HAZ), separating two fusion zones. The central section of the HAZ, characterized by small recrystallized grains, was particularly prone to microcracking. The research indicated that at temperatures above 150°C, these microcracks initiated fractures in the fusion zone, while at lower temperatures, crack initiation was more sensitive to geometric defects in the HAZ. These findings suggest that the fracture behavior of AA6061-T6 is highly temperature-dependent, with significant implications for its use in high-temperature applications.

The third phase examined the high-temperature tensile properties of laser-welded AA5052-H36 and AA6061-T6 alloys. Tensile tests were conducted at temperatures ranging from 25°C to 300°C with strain rates of 0.01 s^{-1} and 0.1 s^{-1}. AA5052-H36 exhibited superior mechanical strength, with a linear decrease in ultimate tensile strength (UTS) as temperature increased, while AA6061-T6 displayed a non-linear reduction in UTS due to phase transformations. The analysis revealed that AA5052-H36 had better energy absorption capacity before fracture up to 250°C, after which energy absorption significantly decreased, raising concerns about creep-related failure risks.

In conclusion, this research provides valuable insights into optimizing laser welding parameters and understanding the mechanical performance of AA5052 and AA6061 alloys under various thermal conditions. The results highlight the critical role of temperature in determining the suitability of these alloys for automotive applications, particularly in environments where high temperatures and tensile loads are prevalent. AA5052-H36 proves to be a more robust option for high-temperature static tensile loads, though the use of any alloy above 250°C requires careful management to mitigate potential creep-related failure risks.

Keywords: Laser welding, Aluminum alloy, Overlap joint welding, Optimization, Double-sided weld, Microstructure, elevated Temperature, Fractography

TABLE DES MATIÈRES

LISTE DES TABLEAUX

LISTE DES FIGURES

LISTE DES ABRÉVIATIONS, DES SIGLES ET DES ACRONYMES

AA	Alliage d'aluminium
AL	Aluminium
ANOVA	Analyse de la variance
ASTM	Société américaine pour les essais et les matériaux
BM	Matériau de base
Cr	Chrome
Cu	Cuivre
CW	Onde continue
DSC	Calorimétrie différentielle à balayage
EDS	Spectroscopie de rayons X dispersifs en énergie
Fe	Fer
FZ	Zone de fusion
GP	Guinier-Preston
HAZ	Zone affectée par la chaleur
HV	Dureté Vickers
Mg	Magnésium
Mn	Manganèse

Nd:YAG	Grenat d'yttrium dopé au néodyme
OM	Microscopie optique
SEM	Microscopie électronique à balayage
Si	Silicium
SR	Taux de déformation
TWB	Flancs soudés sur mesure
UTS	Résistance à la traction ultime
Zn	Zinc

LISTE DES SYMBOLES

Hz	Hertz
J	Joule
kW	Kilowatt
m	Mètre
min	Minute
mm	Millimètre
MPa	Mégapascal
N	Newton
nm	Nanomètre
V	Volt
µm	Micromètre

INTRODUCTION GÉNÉRALE

CONTEXTE GÉNÉRAL

De nos jours, les constructeurs automobiles recherchent constamment de nouvelles technologies pour réduire le poids des véhicules et les coûts de fabrication afin de répondre à des normes de consommation de carburant de plus en plus strictes tout en maintenant la compétitivité économique. Une réponse prometteuse à ces exigences souvent conflictuelles est l'utilisation des techniques de flancs soudés sur mesure (TWB) dans le processus d'assemblage. Les avantages de la technologie TWB comprennent : (1) la réduction des coûts en nécessitant moins de matrices de formage; (2) la réduction du poids en soudant des matériaux en tôles de différentes épaisseurs ou résistances pour répondre aux exigences de performance; (3) l'amélioration de la cohérence dimensionnelle des pièces en éliminant les processus de soudage par points imprécis; (4) une meilleure résistance à la corrosion en supprimant les joints en superposition; et (5) une résistance accrue en remplaçant les soudures par points traditionnelles par des soudures au laser et des soudures par couture [1].

L'utilisation de matériaux légers tels que les alliages d'aluminium et les aciers à haute résistance avancés a progressivement augmenté dans les applications automobiles [2]. L'application des TWB dans les processus d'estampage offre un potentiel significatif pour la réduction de poids requise dans les automobiles actuelles et futures. Cependant, la production de TWB, en particulier à partir de feuilles d'alliage d'aluminium, présente plusieurs défis en raison de leur formabilité inférieure et de leurs exigences de soudabilité moins connues [3].

Le soudage au laser, couramment utilisé dans la production de TWB en acier, est rarement employé pour les TWB en aluminium en raison de la haute réflectivité de l'aluminium, de la présence de couches d'oxyde réfractaire, et de la susceptibilité à la formation de porosité dans la zone fondue, aux modifications de la composition chimique, et même à la fissuration à chaud dans certains alliages d'aluminium [4,5]. Certaines recherches suggèrent que le soudage par friction-malaxage (FSW) peut surmonter certaines des difficultés associées au soudage par fusion des alliages d'aluminium, car il s'agit d'un processus à l'état solide et il est plus facilement appliqué aux matériaux plus tendres [6,7]. Cependant, le soudage au laser offre une productivité supérieure par rapport au FSW, ce qui en fait une approche très attrayante pour les applications de formage à froid, tiède et chaud.

1.1 Processus, Conception des Joints et Défis du Soudage au Laser des Alliages d'Aluminium à Haute Résistance

Le soudage par faisceau laser (LBW) est une technologie de soudage adaptée aux alliages d'aluminium à haute résistance en raison de son faible apport énergétique localisé, ce qui entraîne une déformation minimale, une grande résistance des joints et des vitesses de soudage élevées [8]. Le principe du processus LBW est schématiquement illustré dans la Figure 0-1. Le faisceau laser, généré soit par un laser à l'état solide (généralement Nd:YAG, pompé par diode, laser à disque ou laser à fibre) soit par un laser à gaz (généralement un laser CO_2), est focalisé sur la pièce à usiner. Dans le cas d'un laser à l'état solide avec une longueur d'onde d'environ 1 µm, le faisceau laser est acheminé vers l'optique de focalisation à l'aide d'une fibre (Figure 0-1(a)). Les lasers CO_2, avec une longueur d'onde de sortie de 10,6 µm, nécessitent que le faisceau laser soit dirigé et focalisé sur la pièce à usiner à l'aide d'un système de miroirs en cuivre mobiles et de lentilles ZnSe (Figure 0-1(b)) [9]. Cela présente certains défis pour le système optique des lasers CO_2, notamment pour ajuster la position de mise au point du faisceau laser lors du soudage de géométries complexes.

Le soudage au laser (LBW) des alliages d'aluminium peut être réalisé en mode conduction thermique (Figure 0-1(c)) ou en mode trou de serrure (Figure 0-1(d)). En mode conduction thermique, la densité de puissance du laser est suffisante pour faire fondre le métal, la pénétration du soudage étant obtenue par la chaleur du laser qui se conduit depuis la surface vers l'intérieur du métal. Lorsque l'intensité du laser dépasse un certain seuil, le matériau d'aluminium commence à s'évaporer, créant un trou de serrure. Ce trou de serrure augmente considérablement l'absorption du faisceau laser [10]. L'apport de chaleur concentré pendant la formation du trou de serrure permet une pénétration profonde, entraînant des cordons de petite soudure, mais profonde [8].

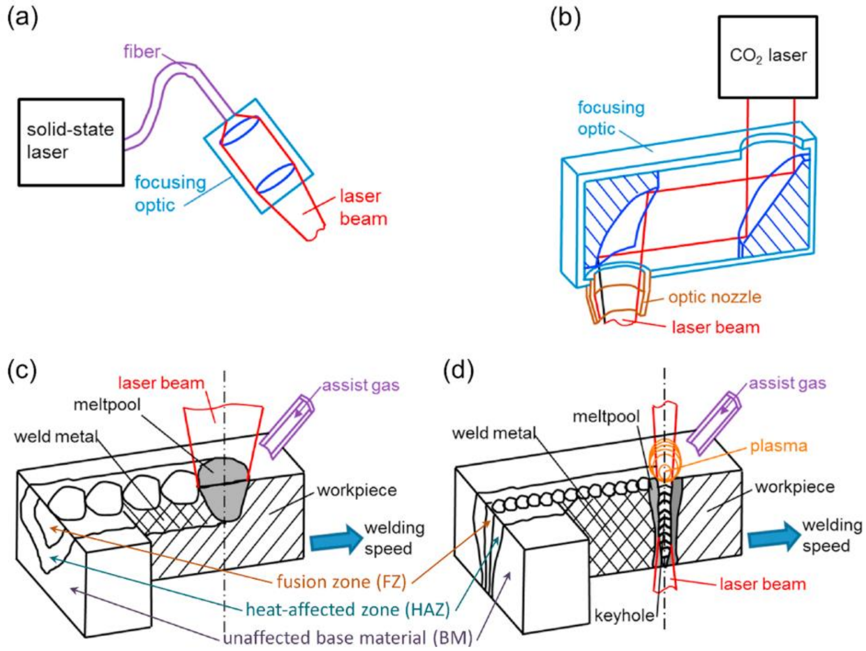

Figure 0-1. Principe du LBW : (a) Laser à l'état solide, (b) Laser CO_2, (c) Soudage par conduction thermique, (d) Soudage par trou de serrure [10].

Démarrer le processus de soudage au laser pour l'aluminium est intrinsèquement difficile en raison de la haute réflectivité du métal pour les radiations laser. Cependant, une fois que le métal liquide se forme, l'absorption des radiations augmente, bien qu'elle reste relativement faible. La technique du trou de serrure est plus couramment utilisée pour l'aluminium en raison de sa vitesse de soudage plus élevée, ce qui est avantageux par rapport aux vitesses de soudage plus lentes associées au mode de conduction thermique. Des vitesses de soudage plus élevées sont plus efficaces d'un point de vue industriel [11].

Au début de la dernière décennie du siècle dernier, les lasers CO_2 et Nd:YAG étaient les deux principaux types de lasers industriels intéressants pour les applications industrielles [12]. Les lasers CO_2 étaient alors disponibles avec des niveaux de puissance allant jusqu'à 6 kW (bien que des machines de soudage au laser CO_2 avec des niveaux de puissance allant jusqu'à 30 kW soient désormais disponibles sur le marché), tandis que les lasers Nd:YAG étaient disponibles avec des niveaux de puissance allant jusqu'à 4 kW. Les lasers Nd:YAG ont suscité de l'intérêt pour l'assemblage de géométries complexes en raison de leur flexibilité de transmission du faisceau par fibre optique [12]. Avec une longueur d'onde de 1,06 µm, les lasers Nd:YAG montrent un bon couplage avec les alliages d'aluminium [13]. En conséquence, les alliages d'aluminium absorbent l'énergie laser plus efficacement [14].

Le faisceau laser CO_2, avec une longueur d'onde de 10,6 µm, est absorbé par des matériaux tels que l'acrylique ou le verre, qui sont couramment utilisés pour les fenêtres dans les systèmes de sécurité laser. Les fenêtres de sécurité laser en acrylique sont généralement moins chères que les fenêtres en verre, nécessaires pour les lasers à état solide fonctionnant à des longueurs d'onde plus courtes. En raison de sa longueur d'onde plus longue, le laser CO_2 présente une haute réflectivité de surface lorsque son faisceau frappe la surface des alliages d'aluminium. Par conséquent, une plus grande quantité d'énergie laser est réfléchie depuis la surface de l'échantillon lors du soudage avec des lasers CO_2. Cela pourrait expliquer pourquoi seuls quelques chercheurs ont récemment étudié le LBW CO_2 des alliages d'aluminium [15]. Cependant, les lasers CO_2 sont également plus efficaces et peuvent générer une puissance plus élevée par rapport aux lasers Nd:YAG [15].

De nombreuses recherches ont été menées sur le soudage au laser des alliages d'aluminium selon divers paramètres. Le Tableau 0-1 résume plusieurs de ces études et l'efficacité du soudage au laser dans différentes conditions.

Tableau 0-1. Valeurs d'efficacité des joints soudés au faisceau laser des alliages d'aluminium à haute résistance.

Matériaux de base / Matériaux d'apport	**Épaisseur mm**	**Résistance du matériau de base MPa**	**Résistance du matériau de soudure au laser MPa**	**Efficacité du joint %**	**Référence**
Alliages Al-Cu-Mg					
AA2024-T3/ autogène	1.25	480	384	80	[16]
AA2024-T3/ autogène	3.0	463	364	79	[17]
AA2024-T3/ AA4043	3.0	463	370	80	[17]
AA2024-T3/ autogène	3.2	480	317	66	[16]
AA2024-T3 (peau)-AA7050-T76 (renfort) / AA4047 (joint en T, contrainte circonférentielle)	2.0 (peau), 2.0 (renfort)	490	445	91	[18]
2A14-T6	2.0	428	262	61	[19]
Al-Cu-Mg-Ag Alloys					
AA2139-T8/ AA4047	3.2	460	350	76	[20]
AA2139-T3/ autogène	3.2	465	320	69	[11]
AA2139-T3/ AA4047	3.2	465	294	63	[11]
AA6156-T4 (peau)-AA2139-T3 (renfort) / AA4047 (joint en T, contrainte circonférentielle, PWHT : peau T6, renfort T8)	3.0 (peau), 2.7 (renfort)	378 (AA6156-T6)	378	100	[21]
Alliages Al-Cu-Li					
AA2198-T3/ AA4047	3.2	461	300	65	[22]
AA2198-T3/ AA4047 (PWHT T8)	3.2	495	341	69	[23]
AA2198-T8/ AA4047	3.2	495	318	64	[23]
AA2198-T3 (peau)-AA2198-T8 (renfort) / AA4047 (joint en T, contrainte circonférentielle)	5.0 (peau), 1.9 (renfort)	430 (AA2198-T3)	335	78	[24,25]
AA2198-T8 (peau)-AA2196-T8 (renfort) / AA4047 (joint en T, contrainte circonférentielle)	3.2 (peau), 1.6 (renfort)	481 (AA2198-T8)	435	90	[26]
AA2060-T8/ AA4047	2.0	500	416	83	[27]

Tableau 0-1. Valeurs d'efficacité des joints soudés au faisceau laser des alliages d'aluminium à haute résistance (suite).

Matériaux de base / Matériaux d'apport	**Épaisseur mm**	**Résistance du matériau de base MPa**	**Résistance du matériau de soudure au laser MPa**	**Efficacité du joint %**	**Référence**
AA2060-T8/ AA5087	2.0	498	317	64	[28]
AA2060-T8 (peau)-AA2099-T83 (renfort) / AA4047 (joint en T, contrainte circonférentielle)	2.0 (peau), 2.0 (renfort)	501 (AA2060-T8)	391	78	[29]
AA2060-T8 (peau)-AA2099-T83 (renfort) / Al-6,2 %Cu-5,4 %Si (joint en T, contrainte circonférentielle)	2.0 (peau), 2.0 (renfort)	501 (AA2060-T8)	411	82	[29]
2A97-T3/ autogène	1.5	390	235	60	[30]
2A97-T3/ AA2319	1.5	390	191	49	[30]
2A97-T4/ autogène	2.0	446	370	83	[31]
Alliages Al-Mg-Li					
AA1420 / AA2319 (soudage hybride laser-MIG)	5.0	391	223	57	[32]
AA1420 / AA2319 (soudage hybride laser-MIG)	5.0	391	267	68	[32]
Alliages Al-Mg-Si					
AA6013-T4/ AlMg5	1.6	345	282	82	[33]
AA6013-T6/ AlMg5 (PWHT)	1.6	397	310	78	[33]
AA6013-T6/ AlMg5	1.6	397	276	70	[33]
AA6013-T4/ AA4046	1.6	345	301	87	[33]
AA6013-T6/ AA4046 (PWHT)	1.6	397	361	91	[33]
AA6013-T6/ AA4046	1.6	397	288	73	[33]
AA6013-T4/ AA4047	1.6	345	316	92	[33]
AA6013-T6/ AA4047 (PWHT)	1.6	397	362	91	[33]
AA6013-T6/ AA4047	1.6	397	300	76	[33]
AA6013-T4 (skin)-AA6013-T4 (stringer)/ autogène	1.6 (peau), 1.6 (renfort)	323	278	86	[34]

Tableau 0-1. Valeurs d'efficacité des joints soudés au faisceau laser des alliages d'aluminium à haute résistance (suite).

Matériaux de base / Matériaux d'apport	**Épaisseur mm**	**Résistance du matériau de base MPa**	**Résistance du matériau de soudure au laser MPa**	**Efficacité du joint %**	**Référence**
AA6056-T4/ AA4047	1.6 (2.5)	-	-	77	[35]
AA6056-T6/ AA4047	6.0	371	275	74	[36]
<u>Alliages Al-Zn-Mg-Cu</u>					
7xxx-T6/ autogène	2.0	676	471	70	[37]
AA7075-T6 / (Feuille V + AA5087)	2.0	592	151 (118, surfaces fraisées)	26, 20 (surfaces fraisées)	[38]
AA7075-T6/ autogène	2.0	592	358 (408, surfaces fraisées)	60, 68 (surfaces fraisées)	[38]

1.2 Flancs soudés sur mesure en alliage d'aluminium (TWB) dans l'industrie automobile

Parmi les matériaux légers, l'aluminium a gagné en popularité comme candidat pour remplacer les tôles d'acier, car il répond aux exigences de torsion et de rigidité pour la construction des châssis. L'utilisation de l'aluminium s'est principalement concentrée sur le moulage de composants individuels tels que les blocs-moteur, les carters de transmission et les roues [39]. Kelkar et al. ont suggéré que l'utilisation des alliages d'aluminium comme remplacement de l'acier dans les assemblages de carrosserie (BIW) offre le potentiel le plus significatif pour la réduction du poids, puisque la carrosserie peut représenter jusqu'à 27 % de la masse d'un véhicule [40]. Par exemple, Muraoka et Miyaoka ont rapporté que la carrosserie du Honda NSX [41], fabriquée en aluminium, était 140 kg plus légère qu'une carrosserie en acier avec une résistance spécifique et une rigidité équivalentes (Figure 0-2). Dans l'assemblage de la carrosserie du Honda NSX, les composants du cadre ont été produits par extrusion à épaisseur variable, et les composants en tôle ont été formés par formage par étirement.

De plus, les recherches menées par Ito et Kobayashi montrent que l'aluminium poreux donne des résultats favorables pour les éléments structurels tels que les longerons avant, les montants B et les boîtes d’écrasement, en raison de ses faibles variations de charge lors des tests de collision [42]. Comme l'a présenté Dieffenbach, les deux approches les plus populaires pour construire les châssis de véhicules en aluminium sont la construction en cadre spatial avec de l'aluminium extrudé et la construction monocoque avec des pièces de carrosserie estampées [43]. Parmi ces méthodes, l'estampage est plus économique pour la production à grande échelle.

Comme le montre la Figure 0-2, les séries 5000 et 6000 sont les alliages d'aluminium les plus couramment utilisés dans l'industrie automobile, et ces deux alliages sont donc l'objet de ce projet.

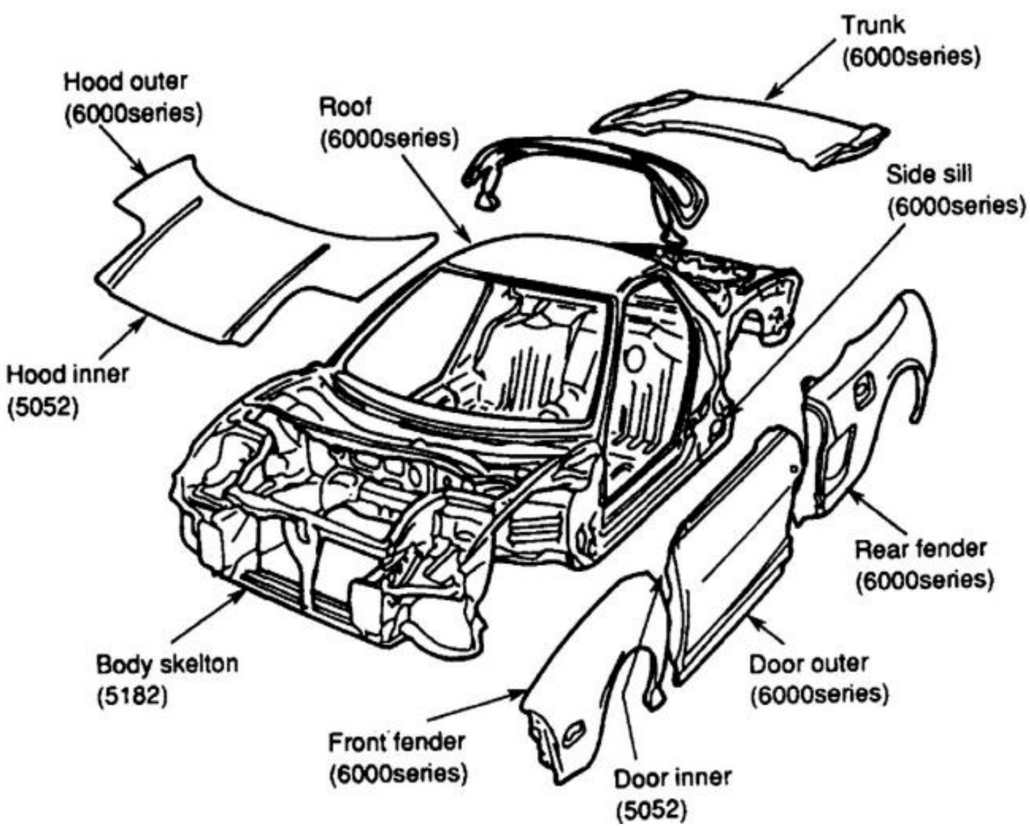

Figure 0-2. Alliages d'aluminium utilisés dans le Honda NSX [41].

1.3 Géométrie des joints soudés dans les flancs soudés sur mesure

L'un des plus grands défis dans le processus de blancs soudés sur mesure est la survenue de défauts géométriques. Les conditions pré-soudure géométriques telles que le décalage, les espaces et les manques de remplissage sont courantes dans les applications industrielles et peuvent entraîner des défauts de soudage, y compris les sous-épaisseurs et la porosité interne. Plusieurs chercheurs ont exploré ce domaine, visant à améliorer la qualité du soudage en ajustant les paramètres ou même en modifiant la composition chimique. Un résumé de certains de ces efforts de recherche est présenté dans le Tableau 0-2.

Tableau 0-2. Résumé des méthodes dans les blancs soudés sur mesure (TWB) : Changements de composition chimique, techniques de laser pulsé et gestion des écarts

Méthode	Détails	Configuration	Référence
Configuration de soudage	Écart avec entretoises	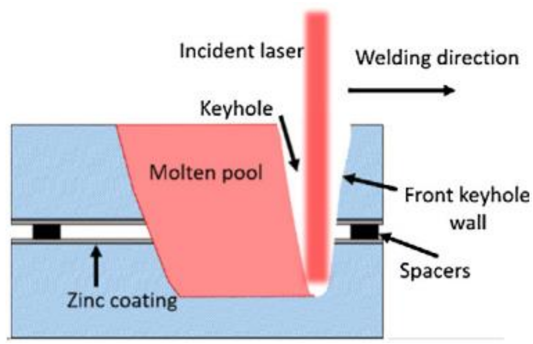	[44,45]
	Écart généré par le laser	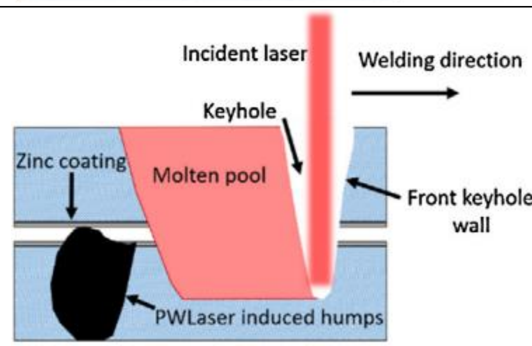	[46]

Tableau 0-2. Résumé des méthodes dans les blancs soudés sur mesure (TWB) : Changements de composition chimique, techniques de laser pulsé et gestion des écarts (suite)

Méthode	Détails	Configuration	Référence
	Feuilles à grand rayon	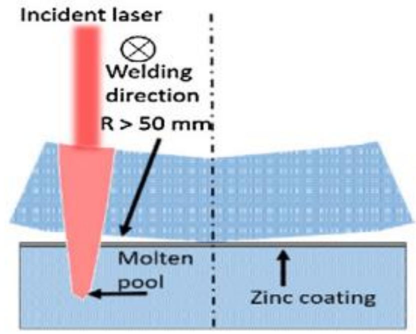	[47]
	Soudage des bords	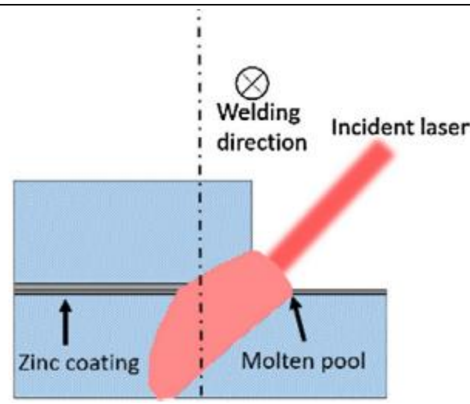	[48]
	Trou de pré-perçage au laser	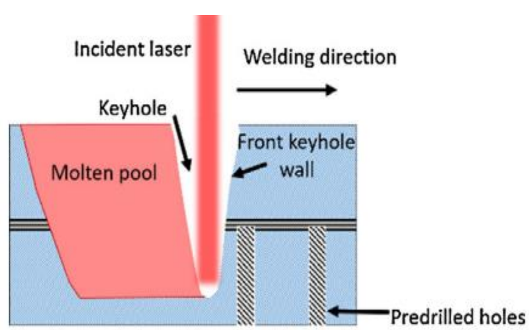	[49]
	Fente d'échappement créée par le faisceau laser direct	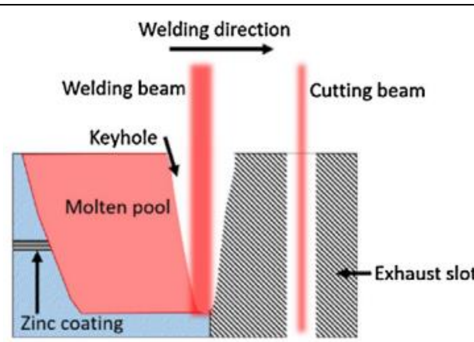	[50]

Tableau 0-2. Résumé des méthodes dans les blancs soudés sur mesure (TWB) : Changements de composition chimique, techniques de laser pulsé et gestion des écarts (suite)

Méthode	Détails	Configuration	Référence
Composition chimique	Couche intérieure en cuivre	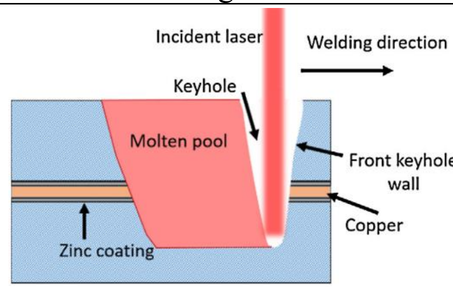	[51]
	Couche intérieure en aluminium	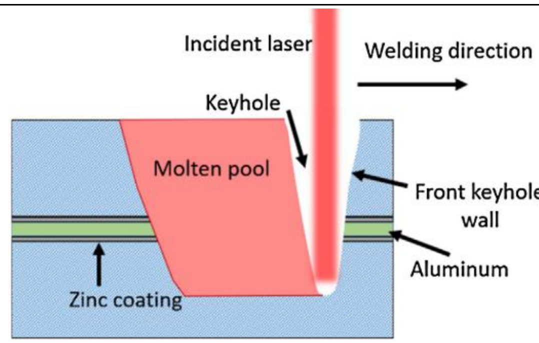	[52]
Lasers pulsés	Refusion à l'aide de lasers pulsés	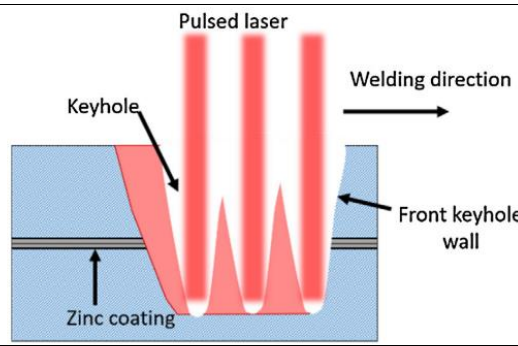	[53,54]

1.4 Comportement en déformation à la traction des alliages d'aluminium à des températures de formage tièdes / chaudes

Malgré une augmentation significative de l'utilisation des alliages d'aluminium dans l'industrie automobile ces dernières années, les alliages d'aluminium en feuille sont encore beaucoup moins utilisés par rapport aux aciers en feuille à faible teneur en carbone, principalement en raison de leur coût plus élevé et de leur moins bonne formabilité à température ambiante. L'élongation à la traction des alliages d'aluminium à température ambiante est généralement inférieure à 30% [55], tandis que la valeur correspondante pour les aciers tués à l'aluminium (A-K) est d'environ 50%. En termes de comportement de formage, les alliages d'aluminium présentent une contrainte limite de formage d'environ 25% dans des conditions de déformation plane à température ambiante, contre environ 45% pour les aciers A-K dans les mêmes conditions [56].

Il a été documenté que la ductilité médiocre des alliages d'aluminium à température ambiante peut être améliorée en modifiant la température de formage, soit vers des températures cryogéniques [57–59], soit vers des températures élevées [60–62]. Le formage de feuilles à des températures légèrement élevées est plus favorable pour les opérations industrielles que le formage cryogénique et entraîne généralement une meilleure productivité. Des essais de formage sur des alliages d'aluminium ont été précédemment réalisés à des températures élevées, spécifiquement dans la plage de températures de formage tiède de 200 à 350 °C, avec des résultats prometteurs [63]. Ces investigations ont montré une amélioration significative de la formabilité des alliages d'aluminium avec l'augmentation des températures de formage, bien que potentiellement à des vitesses de déformation plus lentes que l'estampillage conventionnel. Néanmoins, ces résultats fournissent une base pour explorer l'optimisation des alliages et des taux de formage élevés pour le potentiel de formage tiède/chaud des feuilles d'aluminium dans les applications automobiles.

La formabilité des tôles métalliques dépend à la fois de paramètres intrinsèques, tels que la microstructure du matériau, les inclusions et les propriétés constitutives, ainsi que de facteurs extrinsèques liés à l'opération de formage, notamment la température, le taux de déformation, le chemin de déformation, les conditions de formage et les outils. Actuellement, les données sur le comportement constitutif en fonction du taux de déformation et de la température de formage sont limitées, et les critères de localisation des déformations sont soit incomplets, soit hypothétiques. De plus, pour optimiser les alliages, leur microstructure et les conditions de formage (par exemple, température, niveau de déformation, taux de déformation, chargement et environnement), les tests de dépistage comparatifs sont précieux. Parmi les différents tests de dépistage, le test de traction uniaxiale est le plus courant, car il fournit les propriétés constitutives du matériau et permet de comparer l'allongement total, ainsi que les valeurs d'allongement uniforme et post-uniforme. C'est également le test le plus facile à adapter et à contrôler à des températures élevées.

Malgré les défis associés à l'application directe des propriétés de traction dans le formage biaxial, le comportement constitutif obtenu à partir de la traction uniaxiale est crucial pour estimer les effets des différents facteurs influençant la formabilité sous des conditions de chargement plus complexes. Le durcissement par déformation et le durcissement par taux de déformation—deux propriétés clés mesurées par des tests de traction uniaxiale—influencent fortement la déformation limite de formage, comme l'indiquent les recherches sur les aspects expérimentaux [63,64] et analytiques [65,66] du comportement de formage.

PROBLÉMATIQUE

La littérature sur le soudage au laser des alliages d'aluminium, en particulier les séries AA5000 et AA6000, démontre que ce processus offre un potentiel significatif pour la production de composants légers et de haute qualité essentiels pour l'industrie automobile. Les études ont montré que le soudage au laser peut réaliser des joints précis, solides et résistants à la corrosion tout en permettant des géométries complexes et une distorsion thermique minimale. Cependant, le processus est parsemé de défis en raison des propriétés physiques inhérentes à l'aluminium et des complexités introduites pendant le soudage, telles que la porosité par trou de clé [67], les fissures de solidification [68], et la formation d'undercut [69].

Lorsqu'il s'agit de souder en recouvrement des alliages d'aluminium de différentes épaisseurs, ces défis deviennent encore plus prononcés. Les cycles thermiques subis par le matériau pendant le processus, combinés aux variations d'épaisseur, entraînent une distribution inégale de la chaleur, ce qui affecte la pénétration du soudage et augmente le risque de défauts. Obtenir une qualité de soudure constante à travers des épaisseurs différentes nécessite un contrôle précis de plusieurs paramètres, notamment la puissance du laser, la vitesse de déplacement, la position du foyer, l'amplitude et le motif de l'oscillation. Cependant, la compréhension actuelle de l'interaction entre ces paramètres et leur impact sur les performances de soudure reste limitée. Malgré les avancées dans la technologie de soudage au laser, il existe un écart notable dans la littérature concernant l'optimisation de ces paramètres pour les alliages d'aluminium de différentes épaisseurs, en particulier AA5052. Le manque d'études complètes sur cette configuration spécifique entrave la capacité à prédire et à contrôler la qualité de la soudure, ce qui pourrait conduire à des performances sous-optimales dans les applications industrielles.

En plus de ces défis, le comportement de l'aluminium 6061-T6, un autre alliage largement utilisé dans les applications automobiles et aérospatiales, nécessite une exploration plus approfondie. En particulier, le comportement en rupture des joints soudés au laser double face dans cet alliage, notamment sous des températures et des taux de déformation variables, reste insuffisamment compris. Bien que les études précédentes aient principalement porté sur la microstructure et les propriétés mécaniques des alliages d'aluminium soudés au laser à température ambiante, il existe un écart de connaissance significatif concernant leur comportement à des températures élevées, qui sont des conditions souvent rencontrées dans les environnements opérationnels réels. De plus, bien que le soudage double face soit fréquemment utilisé pour minimiser les défauts tels que la fissuration par solidification et la porosité, la nature séquentielle de ce processus de soudage introduit des changements microstructuraux complexes, notamment dans la zone affectée par la chaleur, qui ne sont pas bien documentés dans la littérature existante. Ce manque de compréhension pose des défis pour prédire les performances et assurer la fiabilité des structures soudées dans diverses conditions d'exploitation, soulignant la nécessité d'études approfondies pour combler ces lacunes critiques.

Bien que les alliages d'aluminium AA5052 et AA6061 soient largement utilisés dans l'industrie automobile, il reste un manque de données complètes sur leurs propriétés mécaniques comparatives, notamment après soudage au laser à des températures élevées. Les études précédentes se sont principalement concentrées sur leurs performances à température ambiante, négligeant les différences critiques dans la façon dont ces alliages réagissent aux charges de traction à haute température. L'AA6061, un alliage traitable thermiquement, est connu pour sa résistance, mais ses propriétés mécaniques se dégradent considérablement à des températures plus élevées en raison de la dissolution des phases de renforcement. En revanche, l'AA5052, un alliage non traitable thermiquement, maintient des propriétés plus stables à des températures élevées, grâce à sa résistance aux changements de phases de précipitation. Cette divergence de comportement entre les deux alliages crée un défi pour déterminer quel alliage est le plus adapté aux applications exposées à des contraintes thermiques. Sans une compréhension claire de la manière dont leur résistance à la traction, leur ductilité et leur comportement en rupture se comparent dans des conditions de haute température, le choix du matériau approprié pour les composants automobiles critiques pour la sécurité devient difficile. Des recherches sont nécessaires pour combler cette lacune de connaissance par une comparaison détaillée des propriétés de traction à haute température de l'AA5052 et de l'AA6061 soudés au laser, fournissant des informations essentielles pour faire des choix de matériaux éclairés dans des environnements thermiques exigeants.

OBJECTIFS

L'objectif de cette thèse est d'améliorer la compréhension des procédés de soudage et de la performance mécanique des alliages d'aluminium, en particulier pour les alliages AA5052 et AA6061, sous différentes conditions. Cela inclut l'optimisation des paramètres de soudage au laser, l'étude des influences microstructurales sur le comportement en rupture, et l'évaluation des propriétés de traction à haute température de ces alliages. Pour atteindre ces objectifs, la recherche est structurée autour d'objectifs spécifiques qui correspondent à des étapes critiques de l'investigation, chacun abordant un aspect distinct des défis associés au soudage au laser des alliages d'aluminium proposés dans ce projet.

Le premier objectif est d'optimiser les paramètres pour le soudage au laser par superposition des feuilles d'aluminium AA5052-H32 de différentes épaisseurs. Les principaux paramètres de soudage au laser, y compris la puissance du laser, la vitesse de déplacement, la position focale, l'amplitude d'oscillation et le motif d'oscillation, seront étudiés pour améliorer la géométrie, la résistance, l'efficacité du soudage et le contrôle de la porosité, tout en minimisant les défauts tels que les échancrures. Cet objectif se concentre sur la résolution des défis liés au soudage au laser des alliages d'aluminium, notamment dans l'industrie automobile, en examinant le comportement mécanique et la qualité du soudage des feuilles d'AA5052-H32 avec des épaisseurs variées. Les résultats fourniront une analyse détaillée de l'impact de ces paramètres sur la qualité du soudage et la performance mécanique, dans le but d'atteindre des conditions de soudage optimales garantissant une haute efficacité et un minimum de défauts.

Le deuxième objectif est d'examiner la relation microstructurale avec le comportement de fracture des soudures double-face dans l'alliage d'aluminium 6061-T6, en particulier dans des conditions de température élevée et de taux de déformation variables pendant le chargement en traction. Cet objectif vise à combler les lacunes existantes dans la littérature en analysant l'influence des techniques de soudage double-face sur l'intégrité structurelle et la performance du matériau d'aluminium 6061-T6 épais. À travers un examen détaillée des changements microstructuraux et de leurs effets sur le comportement de fracture, des informations précieuses sont attendues, ce qui pourrait aider à optimiser les processus de soudage. Les résultats devraient avoir des implications significatives pour améliorer la fiabilité et la performance des alliages d'aluminium dans des applications critiques, telles que dans les industries automobile et aérospatiale.

Le troisième objectif est d'examiner et de comparer les propriétés de traction à haute température des alliages d'aluminium AA5052-H36 et AA6061-T6 soudés au laser. L'objectif est de comprendre comment la température et le taux de déformation affectent la performance mécanique de ces alliages après le soudage au laser, en se concentrant sur la détermination de l'alliage qui démontre des propriétés mécaniques supérieures, telles que la résistance et la ductilité, dans des conditions de formage à chaud. Cet objectif vise à fournir des informations précieuses pour sélectionner le matériau soudé le plus adapté aux applications à haute température, telles que les composants de moteur soudés et les systèmes d'échappement dans l'industrie automobile.

MÉTHODOLOGIE

La première phase de ce projet vise à optimiser les paramètres clés pour le soudage au laser en chevauchement des tôles d'aluminium AA5052-H32 de différentes épaisseurs. Pour ce faire, cinq paramètres critiques sont sélectionnés à partir de la littérature, à savoir la puissance du laser, la vitesse de déplacement, la position focale, l'amplitude d'oscillation et le motif d'oscillation. Ces paramètres sont variés systématiquement dans des plages spécifiques pour évaluer leurs effets sur la qualité du soudage, y compris la résistance mécanique, la porosité et la formation d'entaille.

Une approche expérimentale systématique est adoptée, où les échantillons sont soudés en utilisant différentes combinaisons des paramètres sélectionnés selon un plan d'expériences bien structuré (DOE). Les soudures sont ensuite soumises à divers tests, y compris des mesures de microdureté et des essais de résistance à la traction, pour évaluer la performance mécanique. La microstructure des soudures est examinée par microscopie optique, permettant de détecter les porosités et d'évaluer la qualité de la pénétration de la soudure. Les résultats expérimentaux sont analysés à l'aide d'outils statistiques tels que l'ANOVA pour déterminer l'influence de chaque paramètre sur la performance de la soudure. Cette analyse fournit des informations précieuses sur les interactions entre les paramètres et permet de développer des modèles empiriques pour prédire la qualité de la soudure en fonction des variables d'entrée. L'objectif final de cette phase est d'identifier les paramètres de soudage optimaux pour obtenir des soudures de haute qualité et sans défaut, ce qui servira de base aux phases ultérieures du projet.

La deuxième phase de ce projet plus vaste vise à étudier le comportement de fracture des soudures en aluminium 6061-T6 à double face, notamment sous des températures et des taux de déformation variés. Pour atteindre cet objectif, une configuration expérimentale a été conçue pour étudier la microstructure et les propriétés mécaniques des joints soudés. Divers paramètres, notamment la température (allant de 25°C à 200°C) et les taux de déformation (0.01 s^{-1} et 0.1 s^{-1}), ont été systématiquement variés pour observer leurs effets sur le comportement de fracture du matériau. L'examen microstructural a été réalisé à l'aide de la microscopie optique et de la microscopie électronique à balayage pour analyser les changements dans la zone affectée par la chaleur et les zones de fusion. De plus, des mesures de microdureté et des essais de traction ont été effectués en laboratoire pour évaluer les propriétés mécaniques des soudures sous différentes conditions thermiques et de chargement. Les résultats de cette phase fourniront des informations plus approfondies sur la manière dont la température et le taux de déformation du formage influent sur le comportement de fracture et la performance mécanique du matériau soudé, contribuant ainsi à l'optimisation des processus de soudage au laser pour les alliages d'aluminium.

La phase finale de ce projet est axée sur l'analyse des propriétés de traction à haute température des alliages d'aluminium AA5052-H36 et AA6061-T6 soudés au laser pour les applications automobiles. Le plan expérimental implique la réalisation d'essais de traction à diverses températures allant de 25°C à 300°C, avec des taux de déformation de 0.01 s^{-1} et 0.1 s^{-1}. Les propriétés mécaniques, telles que la résistance à la traction ultime et la déformation de rupture, sont mesurées et comparées entre les deux alliages soudés et les matériaux de base. L'évolution microstructurale est étudiée à l'aide de la microscopie optique et de la microscopie électronique à balayage pour évaluer la croissance des grains et les transformations de phase dans la zone de fusion et la zone affectée par la chaleur. Une analyse statistique, y compris l'ANOVA, est employée pour évaluer l'influence de la température et du taux de déformation sur les propriétés de traction des matériaux soudés. Un modèle de régression est développé pour prédire l'UTS et la déformation de rupture en fonction de la température et du taux de déformation. Les conclusions finales sont tirées en comparant les performances mécaniques des deux alliages soudés à haute température, fournissant des informations sur leur adéquation pour une utilisation dans les applications automobiles.

ORGANISATION DE LA THÈSE

Cette thèse de recherche est divisée en trois chapitres, sous forme d'articles, qui abordent les objectifs mentionnés ci-dessus. Le premier chapitre se concentre sur l'optimisation des paramètres clés dans le soudage par laser en recouvrement des feuilles d'alliage d'aluminium AA5052-H32 de différentes épaisseurs. L'étude examine les effets de la puissance du laser, de la vitesse de déplacement, de la position focale, de l'amplitude d'oscillation et du motif d'oscillation sur la qualité de la soudure. L'objectif principal est de prédire et d'améliorer la résistance mécanique, de minimiser les défauts tels que la porosité et l'entaillage, et d'améliorer la performance globale de la soudure en ajustant systématiquement ces paramètres de processus.

Le deuxième chapitre se concentre sur l'étude des propriétés mécaniques et du comportement de fracture des soudures laser double-face de l'alliage d'aluminium 6061-T6 sous différentes températures et vitesses de déformation. La recherche examine comment différentes températures et vitesses de déformation affectent la microstructure et les propriétés mécaniques des soudures, en particulier dans la zone affectée par la chaleur et les zones de fusion. L'objectif est de mieux comprendre comment les conditions de chargement des échantillons soudés influencent l'intégrité structurelle et la performance du matériau, fournissant des informations critiques pour l'optimisation des processus de soudage laser dans les applications automobiles et aérospatiales.

Le dernier chapitre aborde l'analyse comparative des propriétés mécaniques en traction à haute température des alliages d'aluminium AA5052-H36 et AA6061-T6 soudés au laser. L'étude examine les effets de la température et de la vitesse de déformation sur la performance mécanique de ces alliages, y compris la résistance à la traction ultime, la déformation de fracture et l'absorption d'énergie. Grâce à une combinaison d'essais de traction, d'analyses microstructurales et d'évaluations statistiques, ce chapitre vise à fournir une compréhension détaillée du comportement de ces alliages soudés sous des températures élevées, offrant des informations critiques pour leur application dans des composants automobiles exposés à des charges thermiques et mécaniques.

CHAPITRE 1
APPROCHE SYSTEMATIQUE POUR AMELIORER LE SOUDAGE PAR LASER A RECOUVREMENT DE L'AA5052-H32 AVEC DES EPAISSEURS DIFFERENTES EN EVALUANT LA PERFORMANCE MECANIQUE, L'EVIDEMENT ET LA PENETRATION DU SOUDAGE

Pedram Farhadipour[1], Narges Omidi[1], Noureddine Barka[1], François Nadeau[2], Mohamad Idriss[2], Abderrazak El Ouafi[1]

[1] Université du Québec à Rimouski, Québec, Canada

[2] Conseil national de recherches Canada, Québec, Canada

1.1 RÉSUMÉ EN FRANÇAIS DU PREMIER ARTICLE

L'AA5052 est un alliage d'aluminium largement utilisé dans l'industrie automobile en raison de son excellente soudabilité, de ses propriétés mécaniques et de sa résistance à la corrosion. Cette étude vise à optimiser les paramètres pour le soudage par laser à recouvrement avec oscillation des feuilles d'aluminium AA5052-H32 de différentes épaisseurs. Les paramètres étudiés incluent la puissance du laser, la vitesse de déplacement, la position de la lentille, la forme de l'oscillation et l'amplitude de l'oscillation. Les résultats révèlent que le motif d'oscillation a un effet minime sur la résistance mécanique. De plus, la plage d'intensité de puissance de 13,2 à 20 J/mm² a été identifiée pour garantir que l'efficacité du soudage reste au-dessus de 89,9 %. Cependant, étant donné l'importance de la valeur de l'évidement pour obtenir une ligne de soudure plus lisse, il est nécessaire de maintenir l'amplitude de l'oscillation à une valeur minimale de 1,5 mm. Le motif de microdureté s'avère être une méthode précieuse pour détecter les défauts tels que les porosités sous-jacentes et les déviations causées par un apport thermique excessif sur la feuille supérieure. Les paramètres de traitement optimisés pour les feuilles d'aluminium AA5052-H32 d'une

épaisseur de 1 à 1,5 mm sont déterminés comme suit : 2500 W pour la puissance du laser, 5 m/min pour la vitesse de déplacement, 6,0 mm pour la position de la lentille et 1,5 mm pour l'amplitude de l'oscillation.

Cet article, intitulé « *Systematic approach to improve overlap laser welding of AA5052-H32 with dissimilar thickness by evaluation of mechanical performance, undercut, and welding penetration* », a été accepté pour publication dans *The International Journal of Advanced Manufacturing Technology* et publié en ligne en janvier 2024. En tant que premier auteur, j'ai contribué à la recherche bibliographique, réalisé les essais expérimentaux, effectué les analyses statistiques, interprété les résultats et rédigé le manuscrit. Dr Narges Omidi, deuxième auteure, a révisé l'article et assisté à la rédaction. Le professeur Noureddine Barka, troisième auteur, a proposé l'idée originale, développé la méthodologie et révisé l'article. Dr François Nadeau et Dr Mohamad Idriss, respectivement quatrième et cinquième auteurs, ont apporté des conseils industriels et contribué à la révision de l'article. Le professeur Abderrazak El Ouafi, sixième auteur, a également contribué au développement de la méthodologie.

1.2 SYSTEMATIC APPROACH TO IMPROVE OVERLAP LASER WELDING OF AA5052-H32 WITH DISSIMILAR THICKNESS BY EVALUATION OF MECHANICAL PERFORMANCE, UNDERCUT, AND WELDING PENETRATION

1.2.1 Abstract

AA5052 is a widely used aluminum alloy in the automotive industry due to its excellent weldability, mechanical properties, and corrosion resistance. This study aims to optimize the parameters for wobbling overlap laser welding of dissimilar thickness aluminum AA5052-H32 sheets. The investigated parameters include laser power, travel speed, focal position, oscillation shape, and oscillation amplitude. The results reveal that the oscillation pattern has a minimal effect on mechanical strength. Additionally, the power intensity range of 13.2-20 J/mm2 has been identified to ensure that weld efficiency remains above 89.9%. However, considering the significance of the undercut value for achieving a smoother weld line it is necessary to maintain the oscillation amplitude at a minimum value of 1.5 mm. The microhardness pattern proves to be a valuable method for detecting defects such as underlying porosities and deflection caused by excessive thermal input on the top sheet. The optimized processing parameters for 1-1.5 mm thickness aluminum AA5052-H32 are determined as 2500 W, 5 m/min, 6.0 mm, and 1.5 mm for laser power, travel speed, focal position, and oscillation amplitude, respectively.

Keywords: Laser welding, Aluminum alloy, Overlap joint welding, Optimization

1.2.2 Nomenclature

AA	Aluminum alloy
ANOVA	Analysis of variance
ASTM	American Society for Testing and Materials
CW	Continuous wave
HAZ	Heat-affected zone
HV	Vickers hardness

Hz	Hertz
J	Joule
kW	Kilowatt
m	Meter
min	Minute
mm	Millimeter
MPa	Megapascal
N	Newton
Nd: YAG	neodymium-doped yttrium aluminum garnet
nm	Nanometer
V	Volt
μm	Micrometer

1.2.3 Introduction

Aluminum alloys are non-ferrous lightweight materials, widely used in industrial applications because of their low weight, excellent strength, formability, weldability, and excellent corrosion resistance [15]. Regarding those unique characteristics, aluminum alloys have broader applications, especially in the automotive and transportation industries [70,71].

Spot welding and laser welding are two common methods for joining materials in the industry. Spot welding generally results in weaker joints and higher levels of residual stress, which can lead to distortion [72]. Laser welding, on the other hand, is recognized as a promising method for joining aluminum alloys, offering several advantages such as precise and controlled heat input, minimal thermal distortion, high accuracy, and rapid welding rates. Additionally, laser welding simplifies the design and preparation of joints [73]. The mechanical properties of laser-welded joints depend on various factors, including welding defects and solidified microstructures. These factors are influenced by processing parameters such as laser power, welding speed, oscillation (wobbling), and focal distance, among others [74,75]. However, it is important to note that laser welding of aluminum alloys faces inherent challenges, including issues like keyhole porosity, underfill, and solidification cracks. These challenges can compromise the overall strength of the weld [68,76–78]. To prevent solidification cracks, nanoparticle addition has been proposed. In previous studies, the addition of TiC nanoparticles during solidification of the melting zone resulted in modified α-grain and secondary phase morphologies, ultimately yielding a crack-free fusion joint for AA7075 welds [79,80]. This successful method has also been applied to aluminum series AA6063 with positive outcomes [81]. Additionally, the incorporation of TiC and TiB2 nanoparticles into aluminum alloys 7075, 6061, and 2024 has demonstrated effectiveness in averting potential cracks [82]. In addition to nanoparticle interventions, ultrahigh-speed synchrotron x-ray imaging has been employed to observe keyhole dynamics and establish thresholds for the keyhole to conduction mode transition, dependent on processing parameters [83].

Laser welding of aluminum series 5000 is highly applicable in the automotive industry. Optimization of laser processing parameters is crucial for industrial applications, specifically to achieve highly qualified welds with the least porosity and undercut, maximum ultimate strength, and efficient formability [70]. Park et al. [76] studied the productivity and laser butt weld quality by optimizing laser welding parameters for AA5182/AA5356, recommending values of 4 kW for power, 8.5 m/min for speed, and 2.4 m/min for wire feed. El-Bethany et al. [68] optimized the same parameters for AA5083, AA5052, and AA6061 for different thicknesses (2 mm and 3 mm). They found that speeds exceeding 4 m/min cause porosity and solidification cracking. Arya PK et al. [84] investigated the effect of laser power and speed on 2 mm thick AA6061-AA2024 butt joint fiber laser welding. Their study revealed that lower laser power resulted in inadequate heat transmission, poor surface morphology, and mechanical properties. Yufrng Li et al. [85] optimized the laser power, laser speed, and focal position of 2 mm thickness AA6061 sheets for minimum energy consumption and highest weld quality. Lei Wang et al. [74] investigated oscillation patterns and discovered that although they minimally impacted weld tensile strength, they had a notable influence on ductility. Circular oscillation yielded the finest grain size, the most equiaxed grains, and a significant increase in elongation, around 38%. Idriss M et al. [86] compared pulsed and continuous laser welding for AA5052 sheets, with continuous welding yielding almost defect-free structures. Conversely, Hou J et al. [87] observed in their Al-25Si-4Cu-Mg study that pulsed laser welding reduced defects, including porosity, and resulted in welds with more strength than the base material, attributed to finer, more uniform grain size. These findings demonstrate the effectiveness of both welding techniques in achieving optimal mechanical performance in aluminum alloys. Furthermore, the choice of aluminum alloy combinations also influences the success of these welding methods.

Less effort has been dedicated to examining the influence of laser welding parameters on the mechanical behavior of AA5052-H32. Kim et al. [88] studied the effect of laser welding parameters on the weldability (bead formation, and percentage of porosity) of 1 mm thickness AA5052 alloy during overlap welding. Their research indicates that reducing the heat input results in a more uniform appearance and reduced porosity of the bead. T. E. Abioye et al. [89] used statistical methods to analyze and predict the tensile strength of 2.0 mm thickness butt joint laser-welded AA5052-H32. Also, in a similar study, H. Ramiarison et al. [90] applied a statistical approach, and they found that maximum strength is reached for specific point energy for AA5052 butt joints.

Despite these insights, there is still a noticeable lack of dissimilar thickness overlap laser welding of AA5052-H32. In this research paper, a systematic investigation of key parameters of overlap laser welding including laser power, laser speed, focal distance, oscillation amplitude, and oscillating pattern has been conducted. The optimization process was performed through different criteria, such as weld geometry, weld strength, weld efficiency, porosity, and undercut.

This research is motivated by the automotive industry's urgent need to understand the complexities of welding materials with varying thicknesses. It represents a timely and highly relevant study that marks the beginning of further exploration into cold and hot forming applied to overlapping welded metals—a pivotal area in the future of automotive research.

1.2.4 Materials and Methods

In this study, cold-rolled AA5052-H32 sheets are used. The chemical composition and the mechanical properties of the initial material have been examined and presented in Table 1-1 and Table 1-2, respectively.

Table 1-1. Chemical composition of AA5052

Element	Al	Cr	Cu	Fe	Mg	Mn	Si	Zn
Weight (wt. %)	Balance	0.35	0.1	0.4	2.6	0.1	0.25	0.1

Table 1-2. Mechanical properties of Aluminum AA5052

Material	*Ultimate strength (MPa)*	*Yield strength (MPa)*	*Elongation at maximum strength (%)*
AA5052- H32	233	187	10

A Nd: YAG laser welding machine, which is equipped with an IPG Photonics YLS3000 laser source, with a maximum voltage of 600 V and laser wavelength of 1070 nm is used for the welding process. The maximum laser power of the machine is 3 kW, with a nominal 0.25 mm spot focal diameter. The machine is also equipped with a FANUC robotic arm with a 0.07 mm precision. A 100 µm continuous wave (CW) Nd: YAG optical fiber is used for the welding process. The oscillation frequency is kept constant at 300 Hz. The schematic of the overlap weld joint configuration is shown in Figure 1-1-a. Three types of oscillation patterns including sinusoidal, triangular, and rectangular are studied (Figure 1-1-b, Figure 1-1-c, and Figure 1-1-d). The laser welding processing setups are shown in Figure 1-1-e, and Figure 1-1-f. Figure 1-1-e shows a weld length controlling gauge used first to guarantee the same weld length for all the samples and prevent the defects that can occur at the beginning and end points. The start point defect is caused by the laser beam being turned on before it has reached the optimal welding conditions, such as the correct focus, power level, and speed. This can result in a lack of fusion, porosity, or other imperfections at the beginning of the weld. The end point defect is caused by the laser beam being turned off too quickly. This can result in a depression or crater at the end of the weld, which can lead to cracking or other defects if not properly addressed [91]. Prior to laser welding, the aluminum sheets were cleaned with acetone to remove the organic contaminants. In addition, the oxide layer was also removed using a 600-grit sandpaper. The dimensions of the top and bottom sheets for the welding process are similar, measuring 100 mm × 70 mm. However, they have two different thicknesses, with the top sheet being 1 mm thick and the bottom sheet being 1.5 mm thick (refer to Figure 1-1-f).

In this study, laser welding processes are systematically optimized through a three-stage approach (Figure 1-2). Firstly, the impact of various oscillation patterns on weld efficiency is investigated (Table 1-3), with the most effective pattern being selected for subsequent experiments. Also, the effect of the key parameters such as laser power, travel speed, focal positions, and oscillation amplitude on the porosity are investigated (Table 1-4). In the final stage, the impact of power intensity on both weld geometry and mechanical performance is examined (Table 1-5).

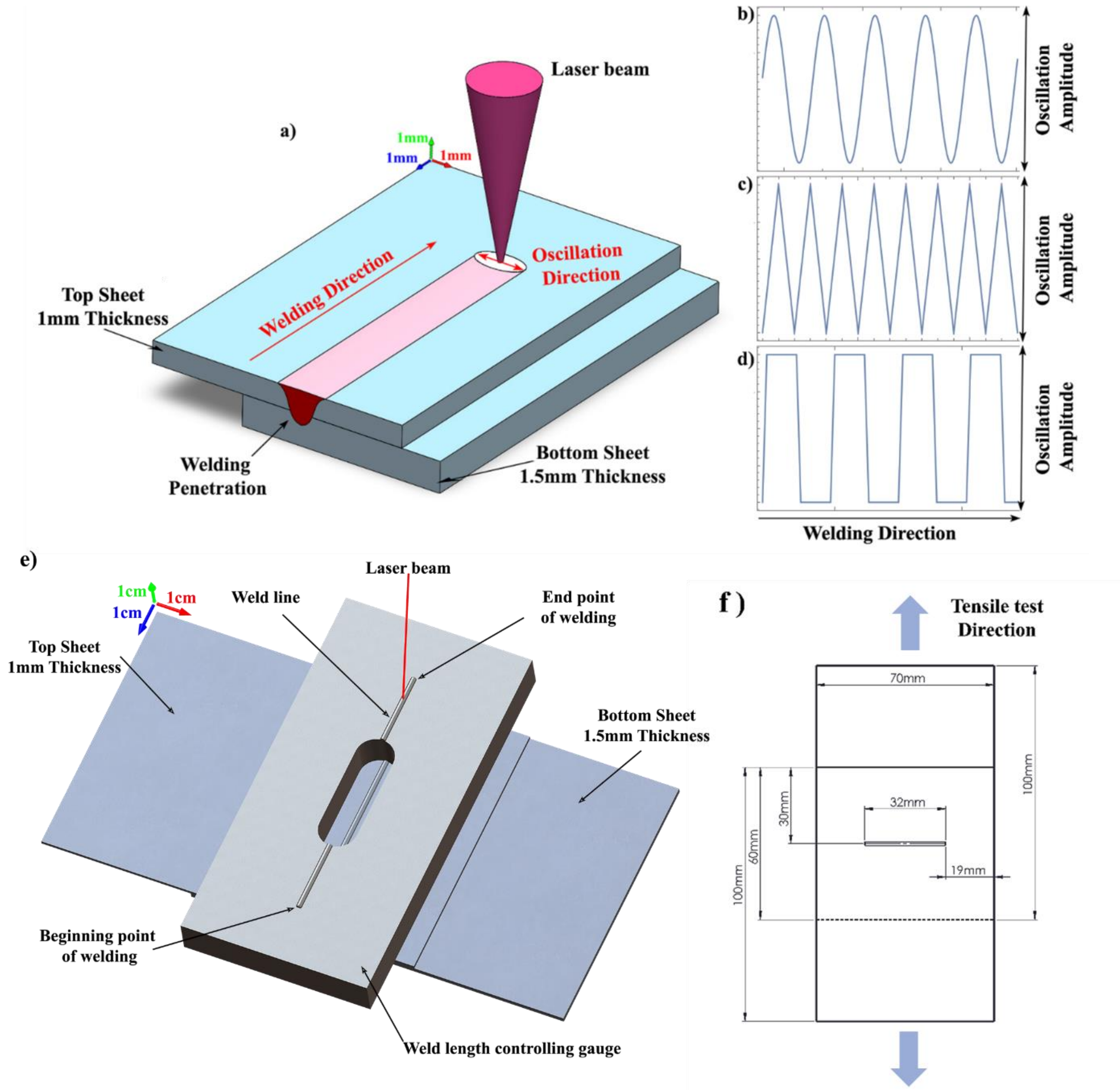

Figure 1-1. Schematic of a) joint configuration and oscillation patterns, including b) sinusoidal pattern, c) triangular pattern, d) rectangular pattern, e) laser welding process setup, and f) sample dimension and direction for tensile test

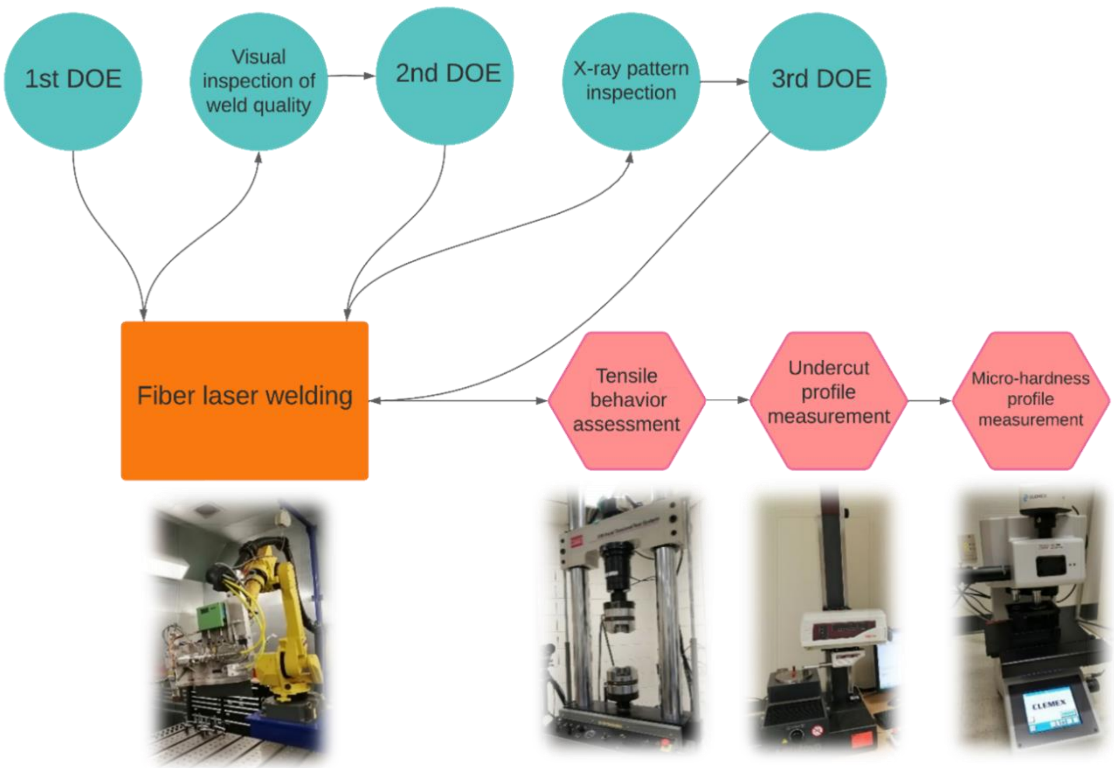

Figure 1-2. Flow chart of the experimental strategy

Table 1-3. The 1st DOE for oscillation pattern, laser power, travel speed, focal position, and oscillation amplitude

ID	*Oscillation pattern*	*Laser power (W)*	*Travel speed (m/min)*	*Focal position (mm)*	*Oscillation amplitude (mm)*
1	Sinusoidal				
2	Triangular	2750	3.0	0	2.0
3	Rectangular				
4	Sinusoidal				
5	Triangular	2500	2.7	0	1.0
6	Rectangular				
7	Sinusoidal				
8	Triangular	3000	2.4	0	1.5
9	Rectangular				
10	Sinusoidal				
11	Triangular	2500	3	1	1.5
12	Rectangular				

13	Sinusoidal				
14	Triangular	3000	2.7	1	2.0
15	Rectangular				
16	Sinusoidal				
17	Triangular	2750	2.4	1	1.0
18	Rectangular				
19	Sinusoidal				
20	Triangular	3000	3	2	1.0
21	Rectangular				
22	Sinusoidal				
23	Triangular	2750	2.7	2	1.5
24	Rectangular				
25	Sinusoidal				
26	Triangular	2500	2.4	2	2.0
27	Rectangular				

Table 1-4. The 2nd DOE for laser power, travel speed, focal position, and oscillation amplitude

ID	*Laser power (W)*	*Travel speed (m/min)*	*Focal position (mm)*	*Oscillation amplitude (mm)*	*Power intensity (J/mm^2)*
1	2500	5.0	3.0	1.0	30.0
2	2750	6.0	3.0	1.5	18.4
3	3000	7.0	3.0	2.0	12.8
4	2750	5.0	1.5	2.0	16.5
5	3000	6.0	1.5	1.0	30.0
6	2500	7.0	1.5	1.5	14.3
7	3000	5.0	0.0	1.5	24.0
8	2500	6.0	0.0	2.0	12.5
9	2750	7.0	0.0	1.0	23.6

Table 1-5. The 3rd DOE with a focus on the 2nd DOE results

ID	*Laser power (W)*	*Travel speed (m/min)*	*Focal position (mm)*	*Oscillation amplitude (mm)*	*Power intensity (J/mm^2)*
1	2500	5.0	6.0	1.5	20.0
2	2750	6.0	6.0	2.0	13.7
3	3000	7.0	6.0	2.5	10.3
4	2750	5.0	4.0	2.5	13.2
5	3000	6.0	4.0	1.5	20.0

6	2500	7.0	4.0	2.0	10.7
7	3000	5.0	2.0	2.0	18.0
8	2500	6.0	2.0	2.5	10.0
9	2750	7.0	2.0	1.5	15.7

For microstructural observation, a Nikon Eclipse MA100 optical microscope is used. Samples are chemically etched by Tucker's reagent. Optical microscopy images are used to measure the weld penetration and penetration quality. The Mitutoyo SV-C3100 form tracker machine with a $\mp 1 \mu m$ precision is used for surface mapping and undercut measurement.

Micro-indentation hardness tests would be a helpful method for the evaluation of welding quality [92]. The Vickers microhardness is measured using the MMT-X7B microhardness tester machine with a 100 g force indentation with a holding time of 10 seconds [93]. This measurement operation involves examining a polished cross-section of each weld, employing a matrix consisting of 18 rows and 37 columns of indentation points, spaced at 150 µm horizontally and 150 µm vertically (Figure 1-3-a). The resulting microhardness profile of the weld provides valuable insights into the weld's geometry through microhardness measurements taken at the cross-section of the weld. By identifying areas of low microhardness using specific indentation points, as illustrated in Figure 1-3-b, voids, pores, and micro-cracks can be easily detected [94]. Additionally, this approach allows for the estimation of the average weld width at a depth halfway into the weld. To visualize the microhardness distribution across the weld, hardness profiles can be generated from the matrix of microhardness tests.

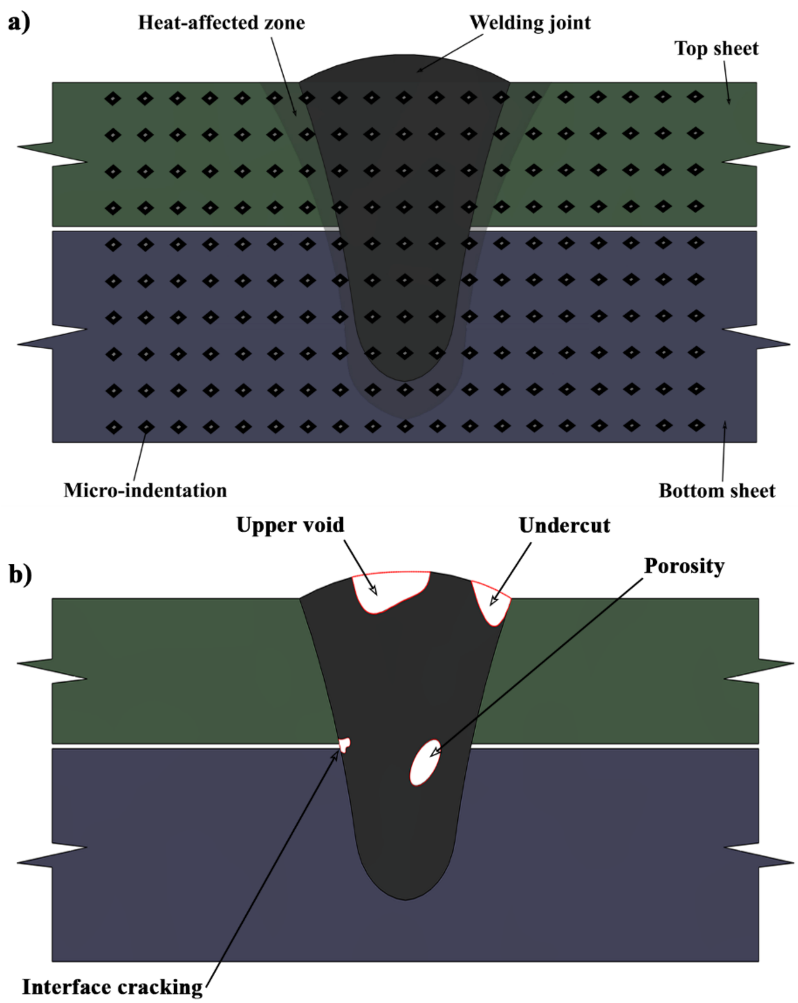

Figure 1-3. a) Schematic of micro-indentation pattern and hardness measurement of the weld cross and b) Geometric characteristic of welding

The MTS810 tensile test machine is used to conduct uniaxial tensile tests at room temperature. This study presents the average of the measurements obtained after three repetitions of the test. The sample size and preparation for the test were in accordance with ASTM B557 [95]. The test is done with a strain rate of 10^{-3} s^{-1}. The initial data of the test result was the maximum load a sample can withstand prior to failure, as well as the deformation[1] of the samples at the point of failure. From this initial data, the mechanical

[1] In this study deformation refers to the crosshead displacement.

properties of the welded joint, including the R-ratio, weld efficiency, and energy absorption, were calculated. The R-ratio represents the maximum load per unit of weld length that samples can withstand prior to fracture and is calculated using Eq. 1-1. The term “Weld efficiency” is used to refer to the ratio of relative strength of a welded metal to the strength of the base metal [96], which is calculated using Eq. 1-2. It should be noted that the strength of welded aluminum joints for aluminum alloys is always less than the strength of the base material mainly due to heat input where we lose the as-received temper of the material [97]. In the case of AA5052-H32, the material goes from the cold-worked (relatively high strength) H32 temper to the annealed temper (relatively low strength). The other reasons correspond to welding defects such as porosity, solidification cracks, and undercut [98]. Therefore, the welding efficiency value would always be less than 100%. Finally, absorbed energy which is an indicator of the formability of the weld, is the energy absorbed per unit of weld length by the weld line prior to failure, as calculated by Eq. 1-3.

$$\text{"R"}\ ratio\ (\frac{N}{mm}) = \frac{Maximum\ Load\ (N)}{Weld\ length\ (mm)}$$

Eq. 1-1

$$Weld\ efficiency\ (\%) = \frac{Maximum\ load\ per\ weld\ length\ (\frac{N}{mm})}{Maximum\ load\ base\ material\ per\ length\ (\frac{N}{mm})}$$

Eq. 1-2

$$Energy\ Absorption\ (\frac{J}{mm}) = \int \text{"R"} ratio\ dx$$

Eq. 1-3

As calculated by Eq. 1-4, the laser power intensity is used to discuss the effect of several input laser parameters (laser power, travel speed, and oscillation amplitude) on the weld properties.

$$Power\ Intensity\ (\frac{J}{mm^2}) = \frac{Laser\ Power\ (w)}{Travel\ speed\ \left(\frac{mm}{s}\right) \times Oscillation\ amplitude (mm)}$$

Eq. 1-4

1.2.5 Results and discussion

1.2.5.1 Effect of amplitude pattern

Figure 1-4 illustrates a comparison of the R-ratio, which represents the maximum mechanical strength per length of the weld, as calculated in Eq. 1-1, for different oscillation patterns. It could be seen that three oscillation patterns cause nearly the same R-ratio values. The maximum variation occurs between samples 4, 5, and 6, with a 9.7% difference respectively 96.2 N/mm, 87.8 N/mm, and 86.9 N/mm. Conversely, the minimum difference is observed in samples 19, 20, and 21, at approximately 1.1%. These results align with findings by Lei Wang et al. [74], who investigated oscillation patterns and found minimal impact on weld tensile strength. The slight variation in the R-ratio is attributed to the similar effective cross-section of the joint area which is calculated by 32mm multiple by oscillation amplitude (Figure 1-1-b to Figure 1-1-f). For every set of three samples with different patterns, the effective cross-section of the weld remains similar since the oscillation amplitude is the same. The statistical ANOVA method was also utilized to validate our experimental results. It was found that only 0.03% of the total results could be attributed to the oscillation pattern, highlighting the limited impact of this parameter on weld joint strength, as demonstrated in Table 1-6.

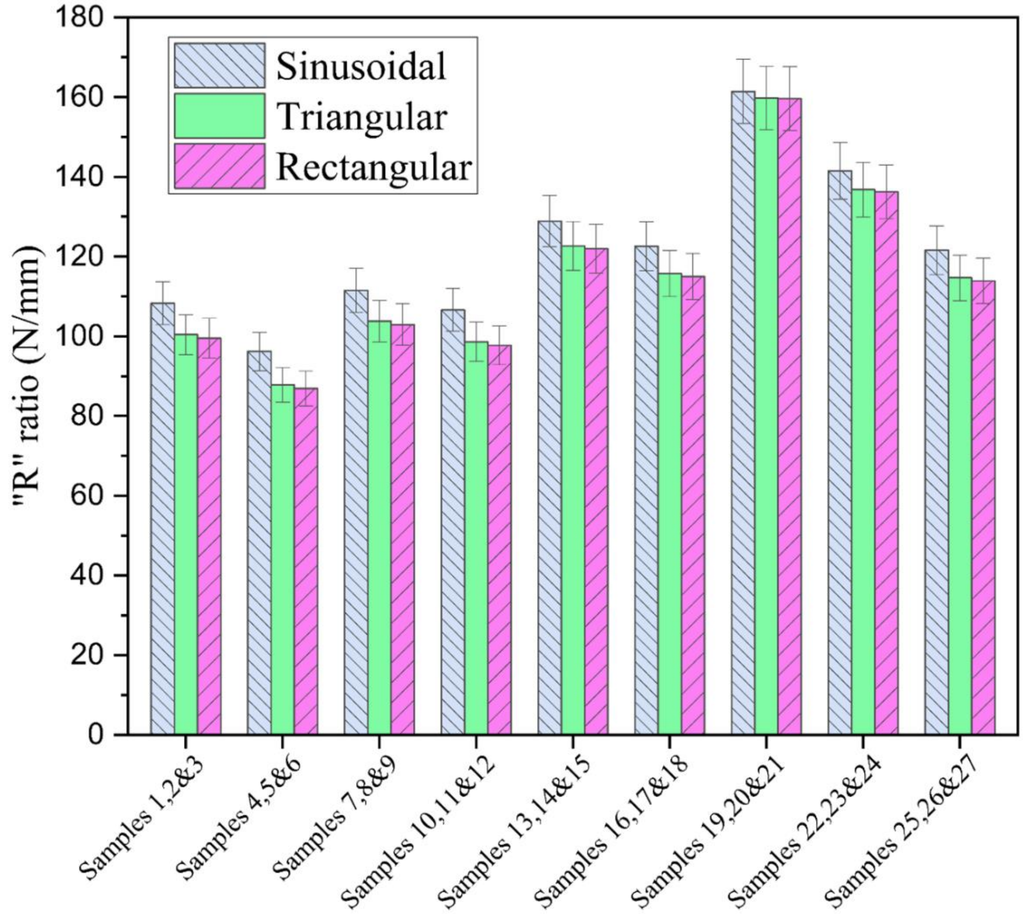

Figure 1-4. R-ratio of the first batch of samples

Table 1-6. ANOVA table of the first batch of samples

Source	DF	Seq SS	Contribution	Adj SS	Adj MS	F-Value	P-Value
Laser power (W)	1	4170.9	37.64%	4170.89	4170.89	70.67	0.000
Travel speed (m/min)	1	632.5	5.71%	632.49	632.49	10.72	0.004
Focal position (mm)	1	4730.4	42.69%	4730.40	4730.40	80.15	0.000
Oscillation amplitude (mm)	1	305.0	2.75%	305.04	305.04	5.17	0.034
Oscillation Shape	1	3.6	0.03%	3.64	3.64	0.06	0.806
Error	21	1239.4	11.18%	1239.43	59.02		
Total	26	11081.9	100.00%				

1.2.5.2 Porosity and weld penetration

The presence of porosity in aluminum laser welding is attributed to the keyhole mode affected by the flow of molten material within the welded track. Extensive research on this phenomenon has been conducted and well-documented [67]. In this study, the dynamics of the molten pool have been found to contribute to keyhole porosity, in samples 7, 8, and 9, which is detected by X-ray image in Figure 1-5. Notably, the degree of porosity is more pronounced in samples with a focal position of zero, which emphasizes the significance of focal position in influencing the flow dynamics and geometric characteristics of the keyhole mode. It is worth noting that, within this study, porosity within samples 7 and 8 are within the acceptable range as defined by ISO13919-2021 [99] standards, whereas in sample number 9, the size of the observed porosity exceeds the acceptable threshold.

The effect of a focal position on the dynamics of the keyhole mode in steel materials is studied by Schaefer et al. [100]. The study reveals a higher distribution of melt flow velocity in cases with a lower focal position, consequently increasing the likelihood of keyhole porosity. The results of this study show the same conclusion for 1mm to 1.5 mm thick aluminum laser-welded sheets, where focal position plays a significant role in keyhole stability and keyhole porosity. The reason is attributed to the instantaneous energy for different focal diameters. In samples 7, 8, and 9, where the focal diameter is set to zero, the laser beam is concentrated at the minimum focal diameter of 0.25 mm. Conversely, in sample 1, the focal position is increased to 3 mm, resulting in a larger focal diameter of 0.34 mm. Reduction in focal diameters results in more instantaneous energy which leads to an increase in the likelihood of porosity formation. The results indicate that to prevent porosity, a focal position of more than 1.5 mm is necessary.

Weld penetration is also another crucial factor for weld line quality evaluation. Figure 1-5-a, and Figure 1-5-b depict both sides of the 9 weld lines. Figure 1-5-b (bottom sheet) shows over-welding for lines 1, 5, 7, and 9, which have laser power intensities of 30, 30, 24, and 23.6 J/mm^2, respectively. That indicates the power intensity of 23.6 J/mm^2 and above leads to over-welding.

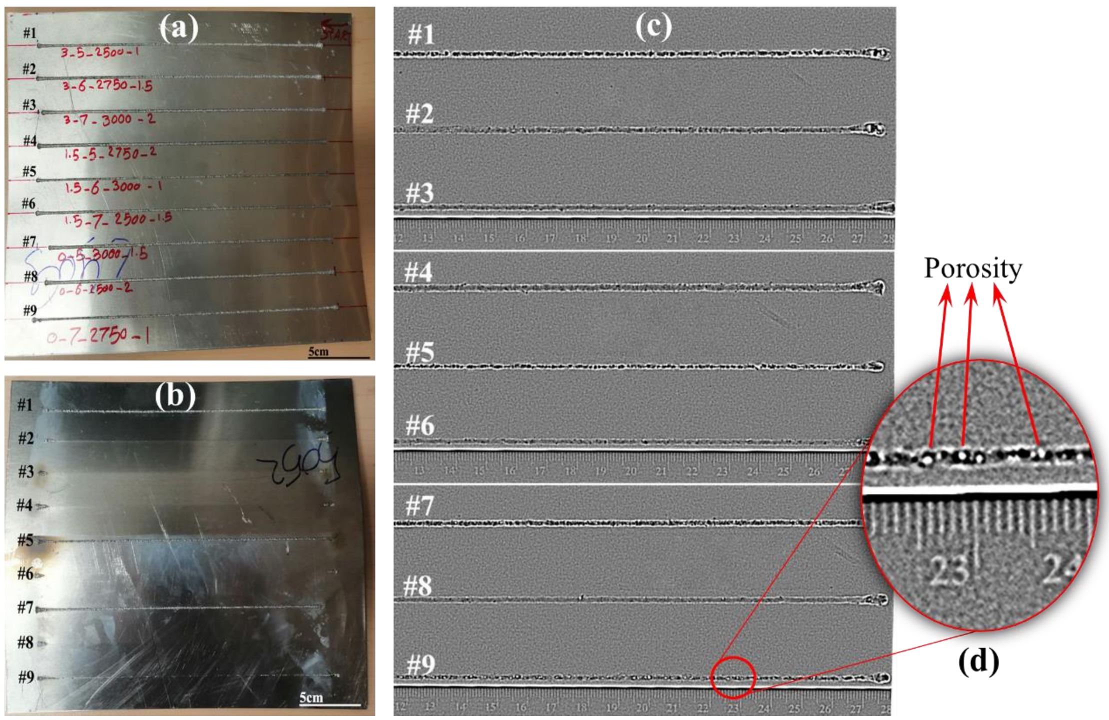

Figure 1-5. Nine weld lines for 2nd DOE from a)top sheet view, b)bottom sheet view, c) X-ray pattern, d) porosities

1.2.5.3 Tensile test results and weld geometry

Tensile test results of the samples with processing parameters specified in Table 1-5 are given in Table 1-7 and Figure 1-6. The tensile test shows two different failure types; fracture from weld joint and fracture from base material. For samples 3, 6, and 8, the fracture starts from the weld line, indicating that the strength of the weld joint is less than that of the base material. For the rest of the samples, the fracture starts from the base material, indicating the weld line has equal or more strength when compared to the base material. Figure 1-6 shows a direct relationship between the power intensity, the R-ratio, the welding efficiency, the deformation, and the formability of the weld. An increase in the power intensity results in increased welding efficiency. The minimum weld efficiency is seen alongside the minimum power intensities, at 10.3, 10.7, and 10 J/mm2, which correspond to sets number 3, 6, and 8, respectively. The weld efficiency for these samples are 20.1 ± 0.3%, 47.8 ± 0.7%, and 43.9 ± 1.2%, all under 50%. If the power intensity rises to around 13.2 J/mm2, the weld efficiency increases significantly to 97.7 ± 1.9% (around 50% increase as compared to samples 3, 6, and 8), and the material breaks from the base material. Thus, a power intensity of 13.2 J/mm2 is the minimum required power intensity for an acceptable weld quality. For samples 1, 2, 5, 7, and 9, where the power intensity is higher than 13.2 J/mm2, the weld efficiency stays above around 90%, which is a significant improvement. Therefore, the minimum acceptable value of the power intensity for a weld efficiency above 90% is 13.2 J/mm2.

Similar to the weld efficiency, there is an abrupt increase in the R-ratio as the power intensity increases from 10.7 J/mm2 to 13.2 J/mm2 (Figure 1-6). For the power intensity above 13.2 J/mm2, the R-ratio does not change significantly. This is justified by the formula of the r-ratio, which represents the strength of the weld joint. Since, for the samples, the failure starts from the base material, the weld strength becomes the same as the base material, and the r-ratio approaches that of the base material. It cannot increase beyond a certain value, which is the strength of the base material. In the same trend, there is a significant increase in formability for the power intensities from 10.7 to 13.2 J/mm2 and a gradual increasing change above 13.2 J/mm2.

In contrast, there is a gradual increase in deformation for power intensities from 10 to 20 J/mm2, and the maximum deformation of 0.95 ± 0.04 mm occurs when the power intensity is at a maximum.

Table 1-7. Tensile test results

ID	*Maximum Load (N)*	*R-ratio (N/mm)*	*Deformation (mm)*	*Welding efficiency (%)*	*Energy absorption (J/mm)*
1	8369.7 ± 30.3	239.1 ± 0.9	0.95 ± 0.04	99.6 ± 0.4	183.6
2	8329.9 ± 96.3	237.9 ± 2.8	0.83 ± 0.02	99.2 ± 1.1	153.8
3	1686.5 ± 27.8	48.2 ± 0.8	0.48 ± 0.01	20.1 ± 0.3	16.5
4	8205.1 ± 158.8	234.4 ± 4.5	0.77 ± 0.01	97.7 ± 1.9	145.5
5	8253.5 ± 18.7	235.8 ± 0.5	0.96 ± 0.00	98.3 ± 0.2	179.3
6	4014.0 ± 58.0	114.7 ± 1.7	0.57 ± 0.01	47.8 ± 0.7	46.7
7	8384.4 ± 15.6	239.6 ± 0.5	0.82 ± 0.04	99.8 ± 0.2	140.6
8	3685.3 ± 98.3	105.3 ± 2.8	0.47 ± 0.01	43.9 ± 1.2	43.7
9	7549.5 ± 180.9	215.7 ± 5.2	0.94 ± 0.03	89.9 ± 2.2	156.4

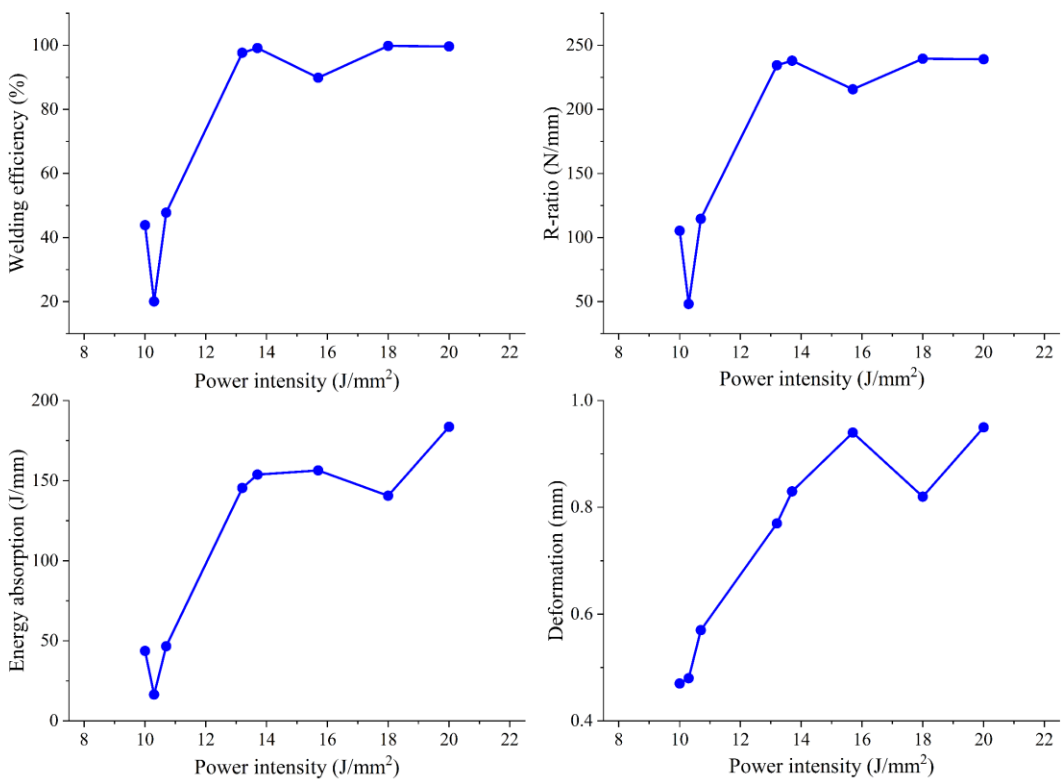

Figure 1-6. Welding efficiency, R-ratio, energy absorption, and deformation versus Power intensity

Figure 1-7 displays cross-sections of the weld lines for samples with power intensities exceeding 13.2 J/mm^2, including the measurement of the effective weld width length. Despite achieving a welding efficiency of over 90%, welding cross-section analysis of samples with power intensity above 13.2 J/mm^2 revealed that the welding line at the sheet interface was discontinuous for samples number 2 and 4 (Figure 1-7-b and Figure 1-7-c). To ensure a continuous weld line in the cross-section, it is recommended to use a power intensity above 15.7 J/mm^2.

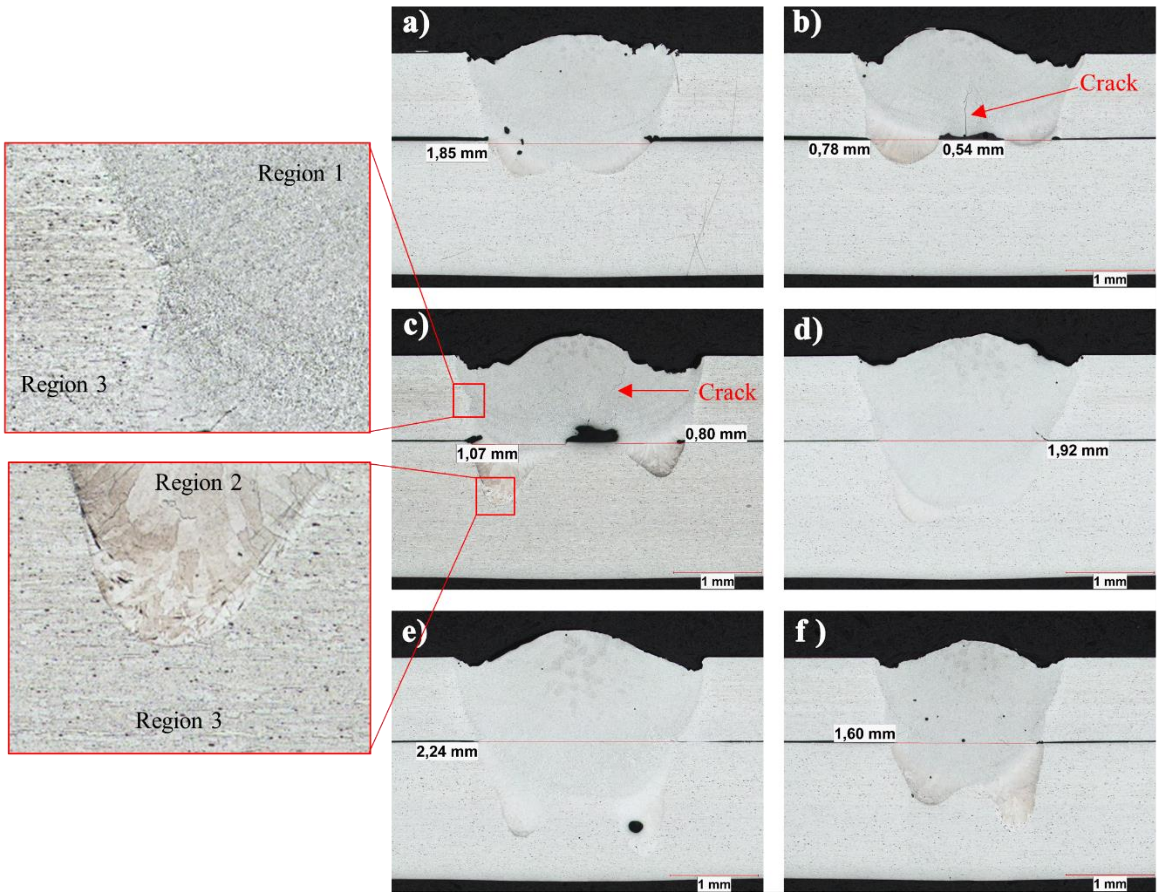

Figure 1-7. Welding cross-section for samples number a) 1, b) 2, c) 4, d) 5, e) 7, and f) 9 which are welded with power intensity more than 13.2 J/mm^2

The undercut value, as well as weld width for power intensities within the acceptable range (according to the tensile performance) of 13.2-20 J/mm^2 are given in Table 1-8. The undercut values and weld width at the interface between the two sheets were measured by the average value of the parameters u and w, respectively (Figure 1-8). The undercut values for samples 1, 2, 4, 5, 7, and 9 are less than 0.25 mm. The minimum undercut of 0.131mm belongs to sample 9, with a power intensity of 15.7 J/mm^2, and then sample 1 (0.161 mm), with a maximum power intensity of 20 J/mm^2. The information suggests a generally positive relationship between power intensity and weld width, which is understandable because higher power intensity typically results in greater penetration and, consequently, a wider weld. However, when it comes to undercut, it becomes evident that it is highly dependent on the oscillation amplitude. In this case, the minimum undercut is achieved with a minimal amplitude of 1.5 mm. This observation highlights the complex relationship between these parameters, indicating that while increased power intensity may lead to wider welds, the control of undercut requires careful adjustment of the oscillation amplitude.

Table 1-8. Measured undercut and weld width value

Sample Number	*#1*	*#2*	*#4*	*#5*	*#7*	*#9*
Undercut (mm)	0.161	0.183	0.250	0.185	0.201	0.131
Weld width (mm)	1.85	1.32	1.87	1.92	2.24	1.60

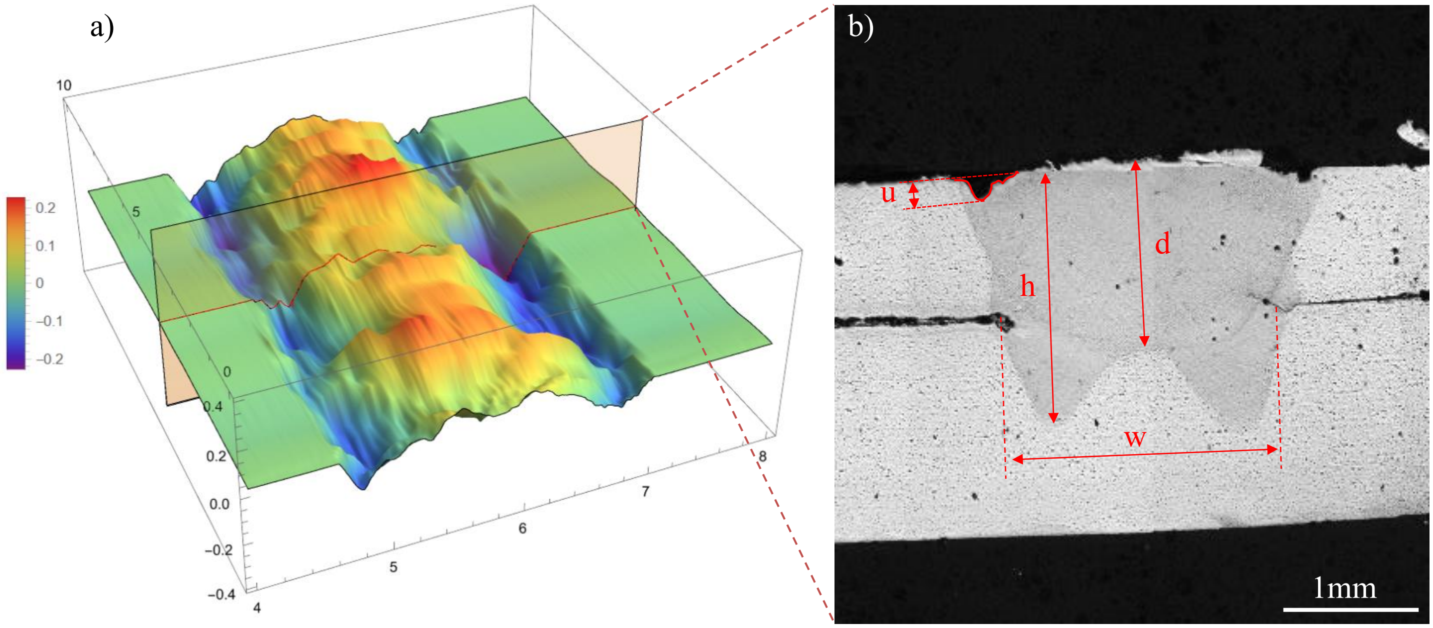

Figure 1-8. a) Scanning of weld surface by multiaxial form tracker machine and b) Optical microscopy of cross section of sample 9

1.2.5.4 Microhardness profile

The microhardness profile of the welded area is presented in Figure 1-9. Recently, Karganroudi et al. [94] used the microhardness profile of the welded area to evaluate the weld line porosity and voids of galvanized steel welded joints. According to their study, a smooth pattern of the microhardness profile is proof of a uniform weld line and any abrupt increase or decrease in microhardness value indicates weld defects. Figure 1-9 shows the microhardness pattern of samples 1, 2, 5, and 9, which were shown to have minimum undercut values from the previous section. Figure 1-9-a indicates an isometric 3D map of the microhardness profile illustrating the top and bottom sheets for sample number 1. A smooth reduction in microhardness can be seen in the weld pool, which is due to changes in microstructure. During the laser welding process with wobbling, the stretched grains remelt, and resolidify into rounded-shape grains, which is one of the reasons for the reduction in microhardness value [74]. The reduction in microhardness value in AA5052 can also be attributed to the evaporation of magnesium. Since magnesium is harder than aluminum, its evaporation in the weld region results in the formation of voids, causing a reduction in microhardness levels within the heat-affected zone and the fusion zone [86]. In this study, as depicted in Figure 1-7-c, the microstructure within the weld pool notably differs from that presented in the literature without wobbling, which is known as the keyhole phenomenon [101]. In this study, the weld pool exhibits a tooth-shaped morphology, with the majority of the area characterized by refined grains (region 1). At the root of the tooth-shaped area, the grains are bigger and elongated, indicating a significant increase in size (region 2), compared to the grains in the region1. Finally, the grains in the base material show slightly elongated grains due to the roll forming and cold working (region 3). Generally, the microhardness value of the weld pool is less than that of the base material, attributed to the inherent hardness of the cold-worked base material. After laser welding, the effect of cold working will be removed from the base material and cause a drop in microhardness in the weld pool.

Figure 1-9-b to Figure 1-9-e indicate 2D a microhardness pattern in samples 1, 2, 5, and 9, respectively. Different types of defects are highlighted in this image, including interface cracking, undercut, porosity, and lack of fusion. Comparing the microhardness patterns, a significant drop (around 50 HV) in the middle of the weld line can be seen for samples 2 (Figure 1-9-c) and 9 (Figure 1-9-e). This reduction is due to the lack of fusion for sample number 2 (Figure 1-7-b) and porosity for sample number 9. This drop in the middle of the weld line is attributed to the penetration geometry, which is tooth-shaped (Figure 1-8-b). The penetration geometry is presented by parameters h and d in Figure 1-8-b; these indicate maximum and minimum penetration, respectively. Values d and h (Figure 1-8-b) will decrease at lower power intensities, indicating less penetration under these conditions. Therefore, for samples 2 and 9, with power intensities of 13.7 and 15.7 J/mm2, less penetration occurs as compared to samples 1 and 5, with a 20 J/mm2 power intensity. Even though a fully penetrated weld (h more than the thickness of the top sheet) can be seen in the weld cross-section of sample 2, the d value is less than the thickness of the top sheet, which is in accordance with Figure 1-7-b. However, the microhardness results of sample number 9 reveal that, despite having a fully penetrated joint (Figure 1-7-f), the very low values observed in the area indicate the presence of porosity in the weld bead. In the same deduction, a fully penetrated weld will occur for samples 1 (Figure 1-9-b) and 5 (Figure 1-9-d) due to the uniform microhardness profile.

Another valuable insight that can be concluded from the microhardness profiles is the extent of distortion occurring within the welded sheets. The presence of blue-colored areas at the interface between the two sheets, accompanied by a sharp reduction in microhardness values, could be an indicator of a gap between the top and bottom sheets. Since all samples are subjected to the same clamping force, this change in microhardness reflects the distortion in the top sheet during welding. This distortion, observed in samples 2 and 9, along with the lack of fusion despite similar or slightly higher power intensities, underscores the fact that the top sheet absorbs the majority of the energy and heat. Consequently, this higher energy absorption results in increased distortion in the top sheet, ultimately leading to the formation of a gap between the two sheets. Notably, this critical information, revealing the extent of distortion and gap formation, could not be recognized through optical microscopy images, as illustrated in Figure 1-7, where this gap formation is less pronounced but clear in the microhardness patterns.

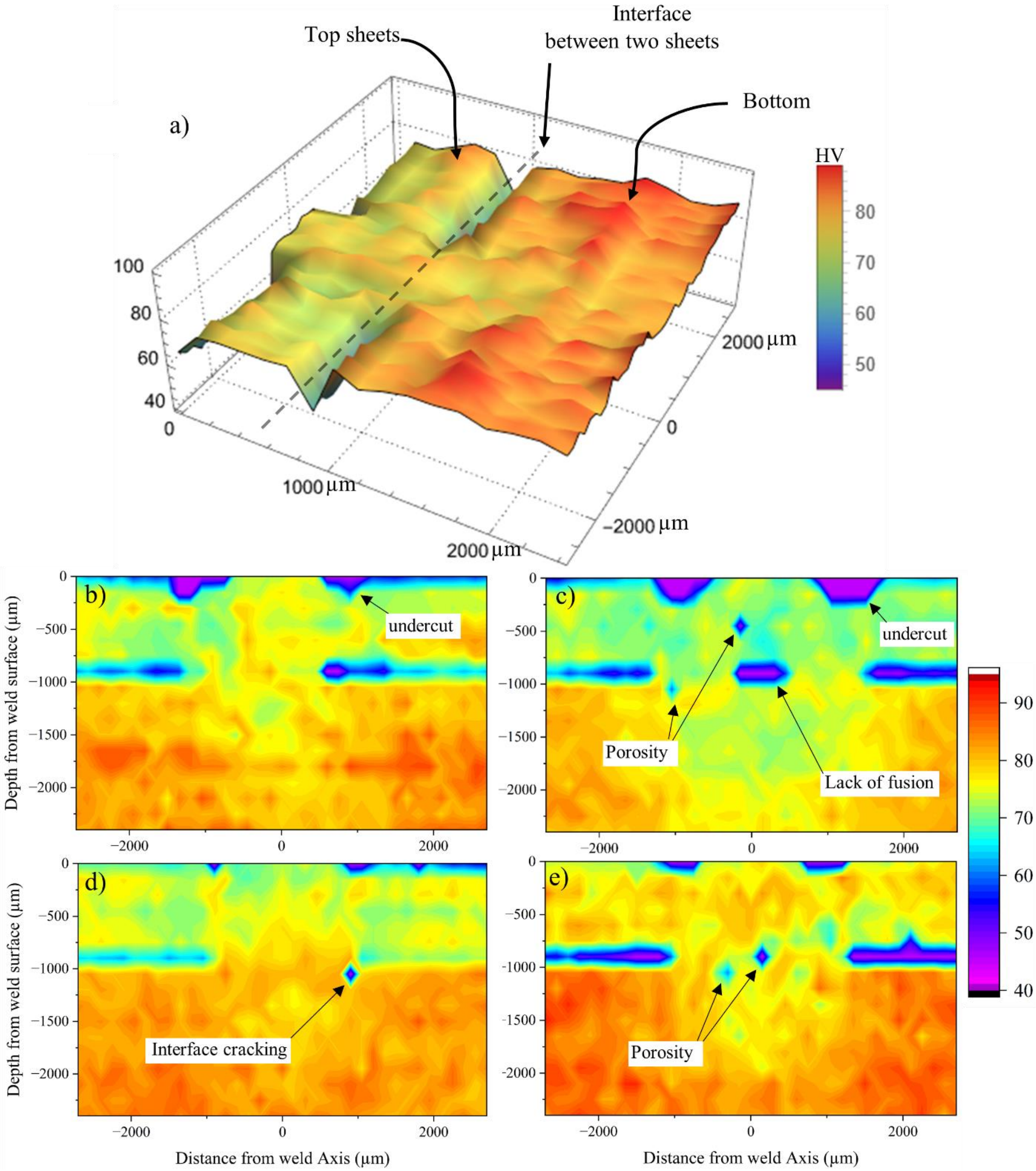

Figure 1-9. Microhardness pattern (HV) of weld cross section a) isometric view, and 2D view for sample number b) 1, c)2, d)5 and e)9

1.2.6 Conclusion

Laser welding processing parameters for overlap joining AA5052-H32 dissimilar thickness sheets (1mm to 1.5 mm) were optimized through several experimental steps. The optimized parameters were the oscillation amplitude, the oscillation shape, the laser power, the travel speed, and the focal position, all represented by a single power intensity parameter. The criteria for the optimization were the weld appearance, weld defects, tensile properties of the weld line, the undercut, and the microhardness pattern. The following conclusions can be drawn from this study:

1. The weld's joint strength is not affected by the oscillation pattern.
2. The acceptable power intensity range for a qualified weld is between 13.2-20 J/mm2, with over-welding becoming an issue for intensities above 23.6 J/mm2. Within the range of 13.2-20 J/mm2, the weld efficiency above 89.9% can be achieved. However, if the power intensity falls below 13 J/mm2, there is a significant decrease in welding efficiency, dropping to under 50%.
3. No direct correlation could be established between power intensity and the undercut value. The undercut value is primarily influenced by oscillation amplitude, with the minimum undercut achievable at an oscillation amplitude of 1.5 mm.
4. Microhardness pattern measurement is shown to be a promising method for detecting weld deficiencies including interface cracking, lack of fusion, underlying porosity, and importantly the welded sheet deflection. The microhardness profile provides valuable information about sheet deflection, which may not be detectable through optical microscopy.

The optimization of welding parameters for AA5052-H32 has been achieved through this research. Further investigations are required to explore the effects of welding orientation on mechanical properties and microstructure.

CHAPITRE 2
UNE ETUDE PHENOMENOLOGIQUE DE L'INFLUENCE DE LA TEMPERATURE ET DE LA VITESSE DE DEFORMATION SUR LE COMPORTEMENT DE FRACTURE DES JOINTS EN BOUT D'ALLIAGE AL-MG-SI SOUDES PAR LASER DOUBLE FACE

Pedram Farhadipour[1], Narges Omidi[1], Noureddine Barka[1], Asim Iltaf[1], Mohamad Idriss[2], François Nadeau[2], Abderrazak El Ouafi[1]

[1] Université du Québec à Rimouski, Québec, Canada

[2] Conseil national de recherches Canada, Québec, Canada

2.1 RÉSUMÉ EN FRANÇAIS DU DEUXIÈME ARTICLE

Les alliages d'aluminium de la série 6XXX sont largement utilisés dans l'industrie automobile en raison de leur résistance, formabilité et résistance à la corrosion. Les soudures double face sont couramment utilisées dans les flans soudés sur mesure (tailor-welded blanks), qui peuvent être formés à des températures élevées. Cette étude examine le comportement à la rupture de l'alliage Al6061-T6 soudé double face sous une charge de traction à des températures variant de la température ambiante à 200 °C et à différentes vitesses de déformation allant de 0,1 à 0,01 s^{-1}. La microstructure de la zone soudée par laser révèle deux zones de fusion situées dans les régions supérieure et inférieure du joint, avec une zone affectée thermiquement (ZAT) en forme de H. La partie centrale de la ZAT, qui sépare les deux zones de fusion, présente une microstructure distincte par rapport aux autres sections de la ZAT. Cette zone est constituée de petits grains recristallisés, autour desquels apparaissent des microfissures le long des joints de grains. Les résultats montrent qu'une augmentation de la température, de la température ambiante à 200 °C, entraîne une réduction significative de la résistance ultime à la traction (UTS) et de la limite d'élasticité, tandis que

la déformation et l'absorption d'énergie augmentent avec la température. La sensibilité à la vitesse de déformation, dans la plage quasi-statique de 0,01 à 0,1 s^{-1}, est minimale, avec un impact négligeable sur l'UTS et l'absorption d'énergie, ce qui suggère une stabilité de ces propriétés dans cette plage. Toutefois, la vitesse de déformation a un effet notable sur la contrainte à l'écoulement et la déformation à la rupture : des vitesses de déformation plus faibles entraînent une déformation à la rupture plus élevée et une limite d'élasticité plus faible. L'analyse statistique confirme ces résultats, indiquant que la température est le facteur dominant influençant les propriétés mécaniques, tandis que la vitesse de déformation joue un rôle secondaire. L'analyse de la fractographie révèle qu'à des températures supérieures à 150 °C, des microfissures dans la zone fondue agissent comme sites d'amorçage de fissures. En revanche, à des températures plus basses, l'amorçage des fissures est plus sensible aux défauts géométriques dans la zone affectée thermiquement.

Cet article, intitulé « *A phenomenological study of the influence of temperature and strain rate on the fracture behavior of double-sided laser-welded Al-Mg-Si alloy butt joint* », a été accepté pour publication dans *Journal of Materials Engineering and Performance* et publié en ligne en Avril 2025. En tant que premier auteur, j'ai contribué à la recherche de l'état de l'art, à la réalisation des essais expérimentaux, à l'analyse statistique, à l'interprétation des résultats et à la rédaction du manuscrit. Dr Narges Omidi, deuxième auteure, a révisé l'article. Le professeur Noureddine Barka, troisième auteur, a proposé l'idée originale, développé la méthodologie et également révisé l'article. M. Asim Iltaf, quatrième auteur, a assisté dans la réalisation des tests de fractographie et leur analyse. Dr Mohamad Idriss et Dr François Nadeau, respectivement cinquième et sixième auteurs, ont fourni des conseils industriels, amélioré la méthodologie et contribué à la révision de l'article. Le professeur Abderrazak El Ouafi, septième auteur, a également contribué au développement de la méthodologie.

2.2 A PHENOMENOLOGICAL STUDY OF THE INFLUENCE OF TEMPERATURE AND STRAIN RATE ON THE FRACTURE BEHAVIOR OF DOUBLE-SIDED LASER-WELDED AL-MG-SI ALLOY BUTT JOINT

2.2.1 Abstract

Aluminum 6XXX series alloys are widely used in the automotive industry for their strength, formability, and corrosion resistance. Double-sided welds are commonly applied in tailor-welded blanks, which could form the welded material at elevated temperatures. This study examines the fracture behavior of double-sided welded Al6061-T6 under tensile load at temperatures ranging from room temperature to 200°C and different strain rates of 0.1-0.01 s^{-1}. The microstructure of the laser-welded area reveals two fusion zones situated in the upper and lower regions of the joint, with an H-shaped heat-affected zone (HAZ). The central portion of the HAZ, which separates the two fusion zones, displays a distinct microstructure compared to other sections of the HAZ. This area consists of small recrystallized grains, which exhibit microcracks around the grain boundaries. The results show that increasing temperature from room temperature to 200°C leads to a significant reduction in UTS and yield strength, while strain and energy absorption increase with temperature. Strain rate sensitivity, within the quasi-static range of 0.01–0.1 s^{-1}, is minimal, with negligible impact on UTS and energy absorption, suggesting that these properties remain stable across this range. However, strain rate has a noticeable effect on yield stress and fracture strain, with lower strain rates resulting in higher fracture strain and lower yield stress. Statistical analysis confirms these findings, indicating that temperature is the dominant factor influencing mechanical properties, while strain rate has a lesser impact. Fractography analysis reveals that at temperatures exceeding 150°C, microcracks in the fusion zone act as crack initiation sites. In contrast, at lower temperatures, crack initiation is more sensitive to geometrical defects in the heat-affected zone.

Keywords: Double-sided weld, Aluminium Alloys, Microstructure, elevated Temperature, Fractography

2.2.2 Abbreviations

Al	Aluminum
BM	Base material
Cr	Chromium
Cu	Copper
EDS	Energy-dispersive X-ray spectroscopy
FZ	Fusion zone
HAZ	Heat-affected zone
Mg	Magnesium
OM	Optical microscopy
SEM	Scanning electron microscopy
Si	Silicon
SR	Strain rate
Zn	Zinc

2.2.3 Introduction

Aluminum 6061-T6 is a widely used alloy across various industries due to its lightweight nature, high strength-to-weight ratio, and superior corrosion resistance [102]. It stands out among aluminum alloys for its ease of fabrication and weldability, making it particularly suitable for applications in the automotive, aerospace, and construction sectors. The alloy's performance benefits significantly from its key alloying elements: magnesium (0.8% to 1.2%) enhances strength and heat treatability, while silicon (0.4% to 0.8%) improves fluidity during casting and contributes to both strength and corrosion resistance [103].

In recent years, laser welding has emerged as a highly effective technique for joining aluminum alloys, especially in the automotive sectors, due to its high precision, minimal heat input, and reduced distortion [104]. One notable application of laser welding is the production of tailor-welded blanks, which involves joining sheets of different thicknesses or materials to create large, complex automotive parts. These blanks are welded together and then undergo deep drawing which often requires higher temperatures to increase formability and reduce the risk of tearing [105].

The microstructure and mechanical properties of 6XXX series aluminum laser welds at room temperature have been studied extensively. Particularly in the context of various laser welding techniques. Narsimhachary et al. [106] conducted a study using CO2 laser welding, highlighting the importance of welding parameters to achieve defect-free welds. Their results indicated the presence of a heat-affected zone (HAZ) with significant hardness reduction due to temperature effects during welding, which caused a loss of aging properties. Similarly, Fan et al. [107] explored the microstructure and mechanical properties of 6061 aluminum alloy using laser-MIG hybrid welding. They found that the joints exhibited two main types of precipitates, with the tensile strength of the joint being 70.2% of the base metal, largely due to porosity defects affecting fatigue performance. Chu et al. [108] investigated the effects of laser beam welding on 6061 aluminum alloy, observing that the microstructure predominantly consisted of coarse columnar and equiaxed dendrites, with a strong cube texture in columnar dendrites negatively impacting weld strength. Their study also noted slight softening in the HAZ due to recrystallization.

Recent studies have extensively investigated the fracture behavior in laser welding of aluminum alloys (at room temperature), highlighting key factors that influence weld integrity, including thermal conductivity, solidification characteristics, and microstructural evolution. Sun et al. [109] examined the challenges associated with fillet lap joints in 6xxx-series aluminum alloys, identifying keyhole instability and centerline cracking as primary concerns due to rapid solidification and volatile element evaporation. Their findings emphasized the role of filler wire selection in mitigating solidification cracks by refining the fusion zone (FZ) microstructure. Wang et al. [110] explored butt joint configurations and demonstrated that beam oscillation techniques improved weld quality by refining grain structures and enhancing ductility, with circular oscillation achieving the most favorable mechanical properties. Chu et al. [111] further investigated heat input effects on AA6061 welds, revealing that higher equiaxed grain ratios enhanced strength and fracture resistance, while columnar dendrites with strong cube textures were more susceptible to failure. Similarly, Deng et al. [112] analyzed solidification cracking mechanisms, concluding that higher Mg content in filler wires reduced cracking susceptibility by modifying grain boundary characteristics and dendrite arm spacing. Additional studies by Karami et al. [113] and Rakhi et al. [114] examined the effects of welding speed, filler metal composition, and heat input on hot cracking and fatigue resistance, highlighting the importance of process optimization in reducing defects. Numerical simulations by Su et al. [115] and experimental investigations by Kim et al. [116] and Kang et al. [117] provided insights into residual stress distribution, porosity formation, and post-weld heat treatment, demonstrating that proper thermal and metallurgical management significantly enhances weld performance. Miyagi et al. [118] further elucidated the role of alloy composition in keyhole stability, revealing that trace element content directly impacts molten pool dynamics and weld seam integrity. Collectively, these studies underscore the critical relationship between microstructural control, alloy selection, and welding parameters in determining fracture behavior, providing a foundation for optimizing laser welding strategies to improve structural reliability in aluminum alloys. However, the mechanical and fracture behavior of aluminum laser-welded joints at elevated temperatures remains an area of limited research.

The mechanical properties and microstructure of laser-welded 6xxx-series aluminum alloys are highly dependent on welding parameters, so the choice between single-sided and double-sided welding plays a crucial role in determining weld quality and structural integrity. Single-sided welding can lead to asymmetric heat distribution, keyhole instability, and increased porosity due to inefficient gas escape, which compromises mechanical performance. In contrast, double-sided welding ensures more uniform heat input and fusion, addressing these limitations. Numerical simulations of double-sided laser beam welding on T-joints for aerospace applications demonstrated that synchronized heat input from both sides creates a bilaterally symmetrical temperature distribution, stabilizing the keyhole and improving weld penetration [119]. Experimental studies further confirmed that simultaneous double-sided welding results in a more uniform equiaxed grain structure and significantly fewer porosity defects than successive welding, where reheating effects cause grain coarsening and trap gas in the weld[120]. Additionally, optimized heat input and keyhole connectivity in double-sided welding minimize porosity by promoting stable melt flow, as observed in AA6056-T4/AA6156-T6 aluminum alloy T-joints [121]. Studies on dual-sided laser welding of aluminum-lithium alloys further highlight the importance of element distribution, with embedded filler wire techniques reducing crack susceptibility and enhancing grain boundary strength [122]. Microstructural analysis of mirror welding in 2219 aluminum alloys confirms that simultaneous welding leads to more uniform grain distribution compared to asynchronous methods, improving tensile strength and fracture resistance. The effect of welding parameters on mechanical performance has also been demonstrated in dissimilar aluminum alloy joints, where controlled focal offset and optimized welding speed significantly improve penetration, hardness, and joint strength [123]. Post-weld heat treatment (PWHT) in double-sided welding has been shown to restore strengthening phases, enhancing both strength and ductility, with aged and solution-treated joints achieving up to 98% of the base metal's tensile strength [124]. Furthermore, laser oscillation and beam incident angles play a critical role in porosity reduction and grain refinement, with optimized oscillation improving mechanical performance by up to 89.5% of the base metal strength [125]. These findings collectively demonstrate that double-sided welding offers superior microstructural control, reduced defect formation, and enhanced mechanical properties compared to single-sided welding, making it the preferred choice for high-performance aluminum structures.

While simultaneous double-sided welding offers significant advantages in terms of symmetry, porosity control, and microstructural uniformity, it is not always the optimal choice, especially in thick-section aluminum alloys where achieving full penetration requires high power intensity. In Al 6061-T6 laser welding, excessive heat input can lead to defects such as solidification cracking, magnesium evaporation, and keyhole porosity, ultimately compromising joint integrity [126]. Additionally, geometrical defects like undercutting, blowholes, and surface roughness may further deteriorate the weld quality [103]. To address these challenges, double-sided welding is often employed to ensure full penetration while minimizing defects. The microstructure of double-sided laser-welded aluminum joints has been extensively studied when welds are conducted simultaneously, typically exhibiting a fusion line surrounding the melting pool with a HAZ along the fusion line, where elongated grains are oriented towards the weld center [127–129]. However, in configurations where simultaneous welding is not feasible—such as in double-sided butt joints—the sequence of laser passes may significantly affect the microstructure and mechanical properties of the weld. Given that the HAZ is often considered the weak point of welded joints, and crack propagation typically initiates in this region [130,131], understanding the effects of successive welding is crucial. In such cases, welding one side first before proceeding to the other allows for better penetration control and precise heat input management. Janasekaran et al. [132] demonstrated that in the welding of dissimilar aluminum alloys (AA2024-O and AA7075-T6), successive welding helped mitigate challenges such as uneven melting and keyhole instability. This approach is particularly useful for alloys with different thermal conductivities, as it reduces the risk of excessive heat accumulation that could compromise weld integrity. Moreover, in cases where lower-power lasers are used, successive welding ensures adequate fusion that might not be achievable through simultaneous welding. However, one drawback of successive welding is the potential for higher porosity levels compared to simultaneous welding, as trapped gas has less opportunity to escape before the second weld pass is completed. While this method has been explored in steel welding, reports on its application in aluminum alloys remain limited. The scarcity of research in this area highlights the need for further investigation into optimizing successive welding parameters to balance heat input, defect control, and mechanical performance for aluminum structures.

Despite the advancements in laser welding research, critical gaps remain in understanding the mechanical properties and defect formation in high-thickness 6061-T6 aluminum welded using the successive double-sided welding method in a butt joint configuration. Most existing studies have focused on simultaneous double-sided welding, often in different joint configurations, leaving the effects of successive welding on microstructure and mechanical behavior underexplored. Moreover, while the high-temperature mechanical behavior of aluminum alloys has been widely studied, research on the mechanical response of butt-welded aluminum joints at elevated temperatures remains scarce. This is particularly crucial for automotive applications, where tailored welded joints undergo high thermal loads, influencing their structural performance. Understanding the evolution of mechanical properties and defect formation at elevated temperatures is essential for ensuring reliability in such demanding environments. This study is particularly important for advancing the application of laser-welded aluminum alloys in industries such as automotive and aerospace, where lightweight, high-strength structures are required to withstand both mechanical and thermal stresses. By investigating the mechanical properties and defect characteristics of high-thickness 6061-T6 aluminum alloy welded using successive double-sided welding in a butt joint configuration, this study provides crucial insights into how welding parameters influence weld quality, structural integrity, and performance at elevated temperatures. The findings will contribute to the optimization of welding strategies, enabling the production of stronger and more reliable aluminum welded joints for high-performance applications.

2.2.4 Materials and method

Cold-rolled AA6061-T6 sheets with 1.5mm thickness were used, with the chemical composition in Table 2-1. The chemical composition of the sheets was determined using standard compositional data, verified through the supplier's datasheet, and confirmed by EDS analysis. Understanding these baseline characteristics is crucial for analyzing the effects of double-sided welding and optimizing welding techniques to enhance material performance.

Table 2-1. Chemical composition of AA6061

Element	Al	Cr	Cu	Fe	Mg	Mn	Si	Zn
Weight (wt. %)	Balance	0.3	0.25	0.2	1.2	0.1	0.75	0.2

The welding process uses a Nd: YAG laser machine with an IPG Photonics YLS3000 laser source. It operates at a maximum voltage of 600 V, with a laser wavelength of 1070 nm and a maximum power of 3 kW. The process uses a FANUC robotic arm with 0.07 mm precision and a 100 μm continuous wave (CW) Nd: YAG optical fiber, with an oscillation frequency set at 300 Hz. Figure 2-1-a shows the butt joint weld configuration. The laser welding variables including laser power, travel speed, focal position, and oscillation amplitude were selected based on a previous study by the authors, optimized for minimal weld defects, and maximum UTS and strain at the fracture point [133,134]. The chosen parameters are 2500 W laser power, 5 m/min travel speed, 6.0 mm focal position, and 1.5 mm oscillation amplitude.

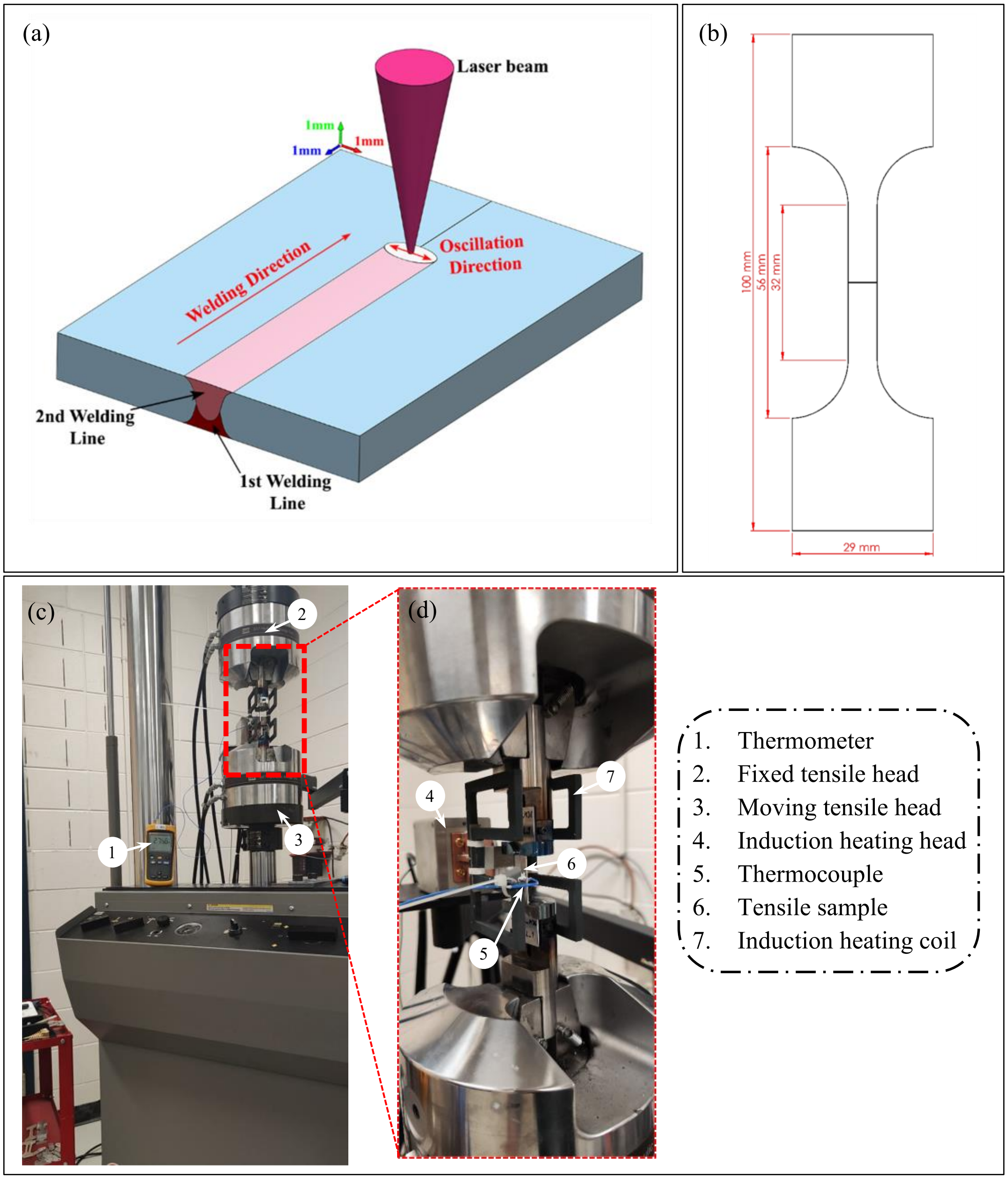

Figure 2-1. (a) Schematic of double laser-welded butt joint showing the weld configuration, weld direction, and the first and second laser pass, (b) Sample dimensions, (c) and (d) high-temperature tensile test equipment

Microstructural observations were performed using a Nikon Eclipse MA100 optical microscope. Samples were chemically etched with a 20% NaOH solution for 45-60 seconds at 50°C. The Vickers microhardness of the welded area was measured using a Clemex MMT-

X7B microhardness tester, applying a 100 g force indentation with a holding time of 10 seconds. Uniaxial tensile tests at different temperatures ranging from room temperature (25°C) to 200°C, and strain rates of 0.01 s^{-1} and 0.1 s^{-1} were conducted using an MTS809 tensile test machine. The study reports the average results from three test repetitions. Sample size and preparation followed the ASTM B557 standard [135]. The schematic of the prepared sample for the tensile test is shown in Figure 2-1-b. High-temperature tensile test equipment is shown in Figure 2-1-c and Figure 2-1-d. To discuss the effect of temperature and strain rate, Ultimate tensile strength (UTS), yield strength, and energy absorption are considered. Energy absorption is calculated based on the equation from previous research by the authors and is shown as the area under the tensile test diagram [133]. Also, reduction factors (R_f) and increasing factors (I_f) have been calculated and discussed using Eq. 2-1, where X represents the mechanical properties, including UTS, yield strength, absorbed energy, and strain, and indicator Y denotes these properties at specified temperatures.

$$R_f \text{ or } I_f = {}^{X_Y}/_{X_{25°C}} \qquad \text{Eq. 2-1}$$

Finally, the SEM electron microscope model SNE-4500M was employed for fractographic and elemental analysis of the weld joints.

2.2.5 Results and discussion

2.2.5.1 Microstructure

The cross-section of the welded joint, shown in Figure 2-2, demonstrates a fully penetrated weld without solidification cracks within the fusion zones, and there is no evidence of keyhole or gas porosity defects. The undercut is within acceptable limits for high-quality welds, which is less than 2 mm [133]. The macrostructure of the welded area comprises four regions: the base material (BM), the first fusion zone (from the initial laser pass - 1st FZ), the second fusion zone (from the subsequent laser pass - 2nd FZ), and the HAZ, as depicted in Figure 2-2-a.

The microstructure of the base material shows coarse grains due to the tempering with an average grain size of ≈7µm (Figure 2-2-f). The microstructure in the FZ shows mixed coarse and elongated grains average grain size of ≈2-5 µm (Figure 2-2-g). The HAZ exhibits an H-shaped pattern, with a majority of it formed between the BM and the FZs, and the central part formed between the 2nd FZ and 1st FZ. These two areas are shown in Figure 2-2-c and Figure 2-2-d respectively. The width of the HAZ between the BM and FZs increases when transitioning from the undercut to the remelted zone. This is Due to the differences in heat dissipation and thermal exposure. In the undercut region, rapid heat dissipation limits the HAZ width, whereas, in the remelted zone, prolonged thermal exposure and multiple heating cycles lead to increased thermal diffusion into the BM, resulting in a wider HAZ. This area displays a microstructure similar to prior studies for single-pass laser-welded joints of aluminum [68,136]. The central area of the HAZ features slightly larger and more rounded grains with less orientation compared to other areas of the weld (Figure 2-2-b). This microstructure is similar to double-sided T-welded aluminum as reported in the literature [127]. However, evidence of microcracks is apparent in this region, likely resulting from residual stresses induced during the second laser pass, leading to cracking within the HAZ.

Elemental analysis along the A-A line in the HAZ indicates stable levels of Al, Mg, and Si in this area. Moving from the base material towards the first FZ, represented by elemental changes through the B-B line and elemental map, reveals stable Si levels with no significant change. However, there is a noticeable decrease in Mg content percentage and an increase in aluminum content percentage within the FZ. This reduction in Mg content is a well-documented phenomenon in laser welding of aluminum, attributed to magnesium evaporation during the welding process [137–141]. Notably, previous studies on Al 6061 suggest that compared to other aluminum alloys with higher Mg content, such as Al 5054, and Al 5083, Mg evaporation is less pronounced [142]. Studies by Narsimhachary et al. [106] on single laser welding joints of Al 6061 reported stable Mg and Si elements throughout the weld area. In contrast, studies by Cieslak et al. [143], and Chen et al. [137] showed a slight decrease in Mg content in the fusion zone for single laser tracks. The pronounced reduction in Mg content observed in this study is likely due to the double-sided weld joints, where the weld undergoes melting twice, doubling the duration for element evaporation. Regarding Si, while some studies have reported the evaporation of this element, Si levels in this study remained stable across all zones [144]. This stability can be attributed to the welding temperature in this study, which was insufficient to cause the evaporation of Al and Si. Finally, the slight increase in Al content can be attributed to the reduction in Mg content.

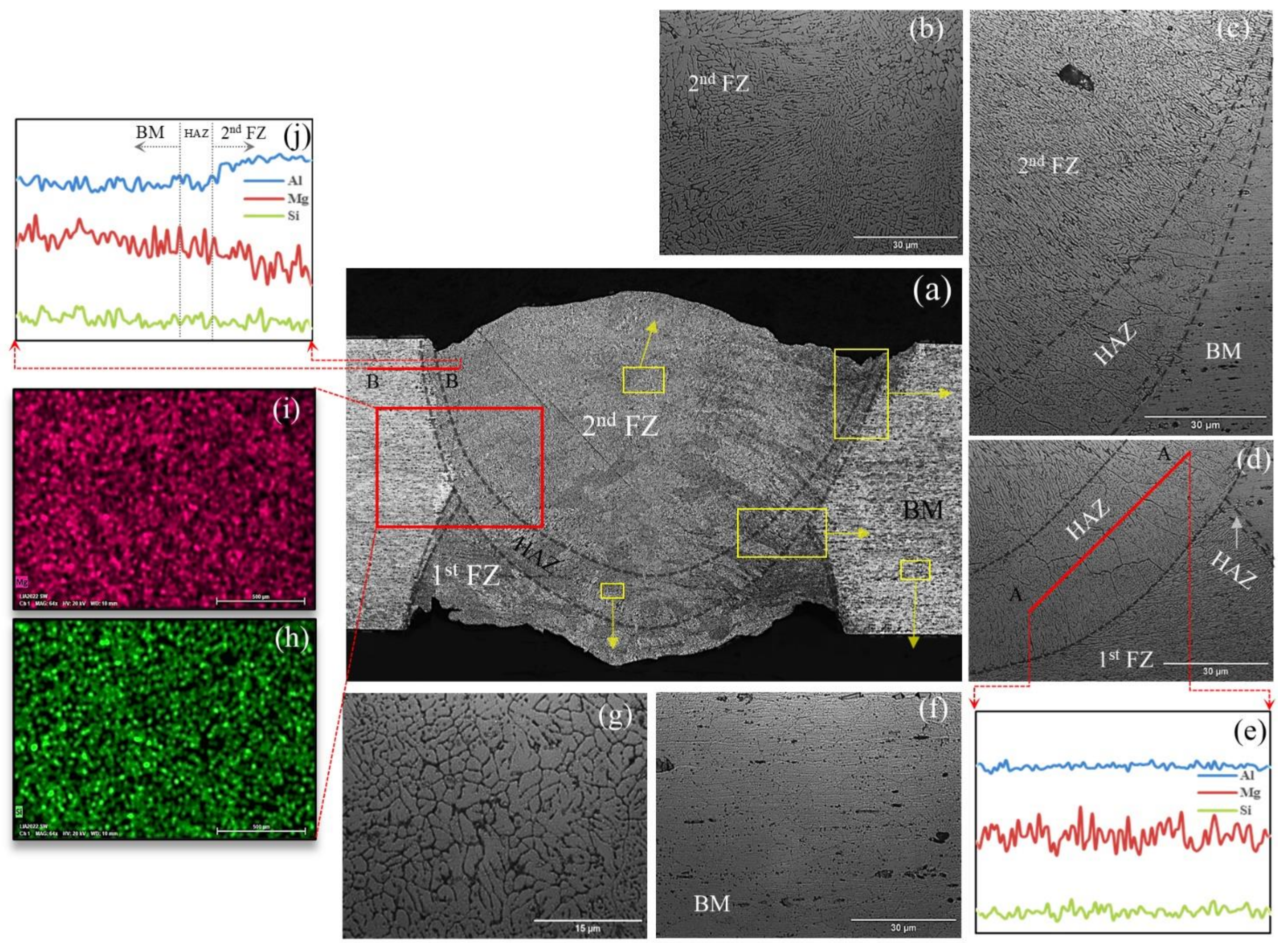

Figure 2-2. Microstructural observation of the welded area depicted in OM images: (a) microstructure of the welded cross-section with elemental changes analysis, (b) microstructure in the FZ, (c) microstructure in the HAZ, (d) and (e) higher magnification in the HAZ alongside elemental change analysis, (f) microstructure in the BM, (g) microstructure in the central area of the HAZ, (h) Si element map, (i) Mg element map, and (j) elemental change analysis alongside the transition line from BM to FZ

In Figure 2-3-a, cracks originating around the grain boundaries in the central region of the HAZ are visible, as highlighted in the higher magnification image in Figure 2-3-b. Unlike typical solidification cracks seen in the FZ, these cracks originate in the HAZ. The source of these cracks may be attributed to the bending force imposed on the welded joint. During the solidification after the first laser pass, shrinkage applies uniform compression force to the weld pool, as depicted in Figure 2-3-c. Similarly, during solidification after the second laser pass, it undergoes shrinkage and compression forces. However, the material underneath resists, resulting in tensile forces (Figure 2-3-d). Consequently, the upper side of the solidifying part experiences compression force, while the lower side of the weld undergoes tensile force. This combination of compressive and tensile forces acting on different parts of the welded joint creates residual stress, which contributes to the initiation of cracks. The initiation of cracks in the HAZ, as shown in our observations, is closely linked to the residual stress fields generated during the welding process.

According to Garcia et al. [145], residual stress fields, including both tensile and compressive forces, significantly influence crack initiation and propagation. Tensile residual stresses, in particular, increase the stress intensity factor at the crack tip, accelerating crack growth, whereas compressive residual stresses can decelerate crack growth by promoting crack closure effects.

Residual stresses in welded joints develop due to the non-uniform heating and cooling cycles inherent in the welding process. As the laser moves along the weld path, a highly localized heat source causes rapid thermal expansion of the molten metal. According to Colegrove et al. [146], during the heating phase, compressive stresses initially form in the weld pool as the surrounding cooler material constrains its expansion. However, upon cooling, the weld metal contracts, and since the surrounding material has already solidified, this contraction induces tensile stresses in the FZ while generating compressive stresses further away in the base material. De and DebRoy [147] further explained that the solid-state phase transformations occurring during cooling contribute to residual stress evolution, as differential volumetric changes between phases introduce additional stress fields. Li et al.

[148] demonstrated that tensile stress peaks at the weld centerline due to the restrained shrinkage of the solidified metal, while compressive stresses develop in the HAZ as the surrounding base metal resists the contraction of the FZ. Zhao et al. [149]confirmed through finite element modeling that these stress distributions follow a predictable pattern, where tensile residual stress accumulates at the weld bead and compressive stress dominates the surrounding regions, leading to the observed crack formation in the HAZ.

Residual stress formation in laser welding has been widely studied, confirming that tensile and compressive residual stresses coexist within the weld bead and HAZ. According to Rong et al. [150], multipass laser welding amplifies these effects, as each subsequent weld pass alters the stress equilibrium, redistributing tensile and compressive fields across the joint. Colegrove et al. [146], validated that the peak tensile residual stress aligns with the weld centerline, with compressive stress forming in the outer HAZ, reinforcing the role of stress redistribution in crack formation.

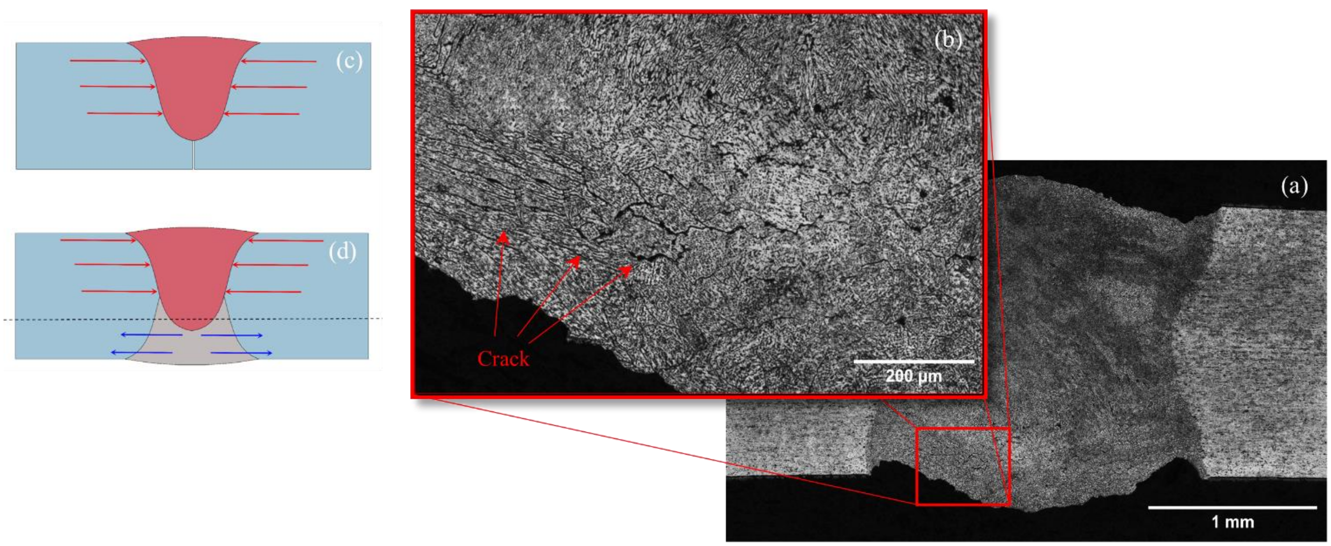

Figure 2-3. OM images of etched cross-sections of the weld showing (a) low magnification and (b) higher magnification, highlighting cracks in the central area of the HAZ, and Schematics of the heat transfer and applied force during in the (c) first laser pass, and (d) second laser pass.

2.2.5.2 Microhardness

The microhardness distribution across the welded cross-section is depicted in Figure 2-4-a. Within the base material, an average microhardness of approximately 81 HV is observed, a characteristic attributed to the presence of strengthening phases inherent to the Al-Mg-Si alloy [151]. Moving into FZs, a slight reduction in microhardness is noted, with values averaging around 70 HV at the center. However, in the central region of the HAZ, a more significant decrease in microhardness is observed, with values dropping to approximately 55 HV.

The microhardness map in double-sided laser welding is different from that in single-pass laser welding. The microhardness value in the FZ is lower than in the base material due to two main reasons. Firstly, magnesium evaporation leads to a decrease in the formation of Mg_2Si precipitates—an intermetallic compound that increases hardness [152]. Secondly, rapid cooling during the process interrupts the precipitation-hardening mechanism. The precipitation hardening sequence of metastable phases in the aluminum 6061-T6 alloy, which contains Mg and Si as dominant alloying elements, is shown in Eq. 2-2:

$$\alpha' \rightarrow \alpha + G,P \rightarrow \alpha + \beta'' \rightarrow \alpha + \beta' \rightarrow \alpha + \beta \qquad \text{Eq. 2-2 [106]}$$

A supersaturated solid solution α is created by heating and then quickly cooling the alloy (solutionizing and quenching). This solution forms small clusters named Gunnier–Preston (G.P.) zones during aging below 160°C. As aging continues, phases called β'' and β' develop within the aluminum matrix. The β'' phase strengthens the alloy and is stable below 260°C. During welding in the first weld line, the HAZ reaches temperatures above 260°C. This high temperature causes the β'' phase to transform into the β' phase. This transformation softens the alloy because the β' phase is not as effective at hardening the material as the β'' phase [106]. When the material is subjected to the second weld line, the remelted zone undergoes this transformation again. As a result, the material becomes softer and reaches its minimum hardness.

Figure 2-4-b illustrates the microhardness profiles along three lines traversing the upper, central, and lower regions of the weld bead. Consistent with the microhardness map provided in the preceding paragraph, all lines in bead regions exhibit a decrease in microhardness. Notably, a substantial drop in microhardness is observed in the lower part, which can be attributed to the presence of microcracks evident in the microstructure section. These microcracks significantly contribute to the material's susceptibility to indentation and subsequent weakening.

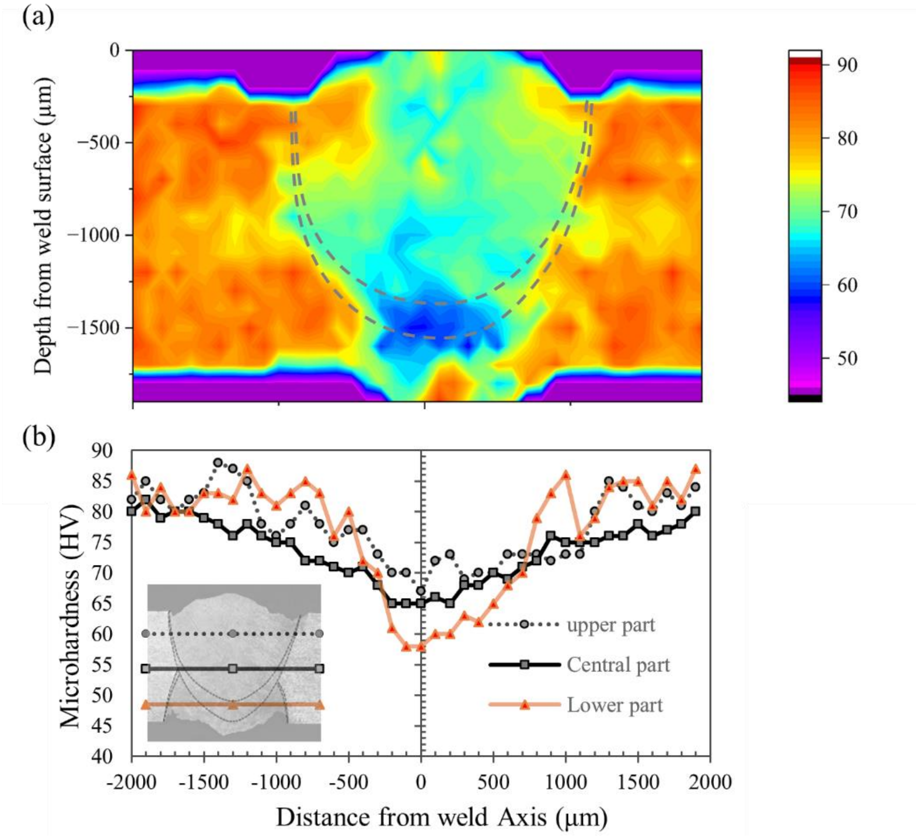

Figure 2-4. Microhardness (a) map of the cross-section of the weld, and (b) profile through the three lines at different depth

2.2.5.3 Tensile behavior

Tensile test results including UTS, yield stress, strain, and absorbed energy at various temperatures, including room temperature (25°C), 50°C, 100°C, 150°C, and 200°C, and two different strain rates (0.01 and 0.1 s^{-1}) are given in Figure 2-5. As temperature increases, there is a noticeable decline in both UTS and yield stress (Figure 2-5-a, and Figure 2-5-b). For instance, at 0.01 s^{-1} strain rate, UTS decreases from 237.6 MPa at room temperature to 192.5 MPa at 200°C, and yield stress decreases from 170 MPa to 150 MPa over the same temperature range. Similarly, for a strain rate of 0.1 s^{-1}, UTS falls from 240.3 MPa at room temperature to 193.9 MPa at 200°C, and yield stress decreases from 178.5 MPa to 157.5 MPa. This decline in mechanical strength is likely attributed to thermal softening, enhancing dislocation movement [153,154]. Thermal softening occurs as the increased thermal energy at higher temperatures reduces the effective stress required to initiate dislocation movement, lowering the material's strength. Additionally, elevated temperatures may lead to dislocation annihilation and grain boundary sliding, further decreasing the material's resistance to deformation.

Conversely, the fracture strain and absorbed energy exhibit an opposite trend, increasing with temperature (Figure 2-5-c, and Figure 2-5-d). At a strain rate of 0.01 s^{-1}, the strain rises from 0.042 at room temperature to 0.074 at 200°C, while energy absorption goes from 2.158 J to 3.4 J. This trend is consistent with the other strain rate of 0.1 s^{-1}, where strain increases from 0.036 to 0.063, and absorbed energy increases from 2.297 J to 3.449 J. The increase in strain and absorbed energy suggests that the material becomes more ductile and deformable at higher temperatures, allowing it to absorb more energy before failure. Elevated temperatures promote greater atomic mobility and diffusion, leading to increased plastic deformation before fracture. This allows the material to accommodate more strain without failure.

In the range of strain rates tested (0.01 and 0.1 s^{-1}), the impact on UTS (Figure 2-5-a) and absorbed energy (Figure 2-5-d) is minimal, suggesting that these properties are relatively insensitive to strain rate variations within this range. However, yield stress and fracture strain, shown in Figure 2-5-b and Figure 2-5-c, respectively, exhibit greater sensitivity to strain rate changes. In Figure 2-5-b, a higher strain rate during the test leads to an increase in yield strength, while in Figure 2-5-c, it reduces fracture strain. This occurs because, at lower strain rates, the material has more time for dislocation motion and other deformation mechanisms, allowing it to undergo more deformation before reaching the yield point [155]. Chen et al. [156] explained that AA6xxx series aluminum alloys exhibit low strain rate sensitivity due to their dominant strengthening mechanisms and uniform microstructure. These alloys are primarily strengthened by Mg_2Si precipitates and solid solution hardening, which impose weaker resistance to dislocation motion. As a result, their flow stress remains nearly constant across different strain rates. Additionally, the lower work hardening rate reduces the additional stress required for plastic deformation at high strain rates. With a uniform microstructure and fewer obstacles to dislocation glide, the mechanical properties of AA6xxx alloys remain stable, allowing them to be treated as strain-rate insensitive, making them ideal for applications requiring predictable deformation behavior. Scapin et al. [157] explained the effect of strain rate on the mechanical behavior of Al6061-T6 alloy can be explained through dislocation dynamics and thermomechanical interactions. At low strain rates ($<10^3$ s^{-1}), plastic deformation is governed by thermally activated dislocation glide, allowing dislocations to bypass obstacles such as grain boundaries and precipitates with minimal resistance. Since dislocations have sufficient time to overcome barriers through thermal activation, the applied stress required for plastic deformation remains nearly constant, resulting in minimal strain rate sensitivity. Additionally, the weak interaction between dislocations and Mg_2Si precipitates at low strain rates prevents significant strain-rate-dependent strengthening effects [158].

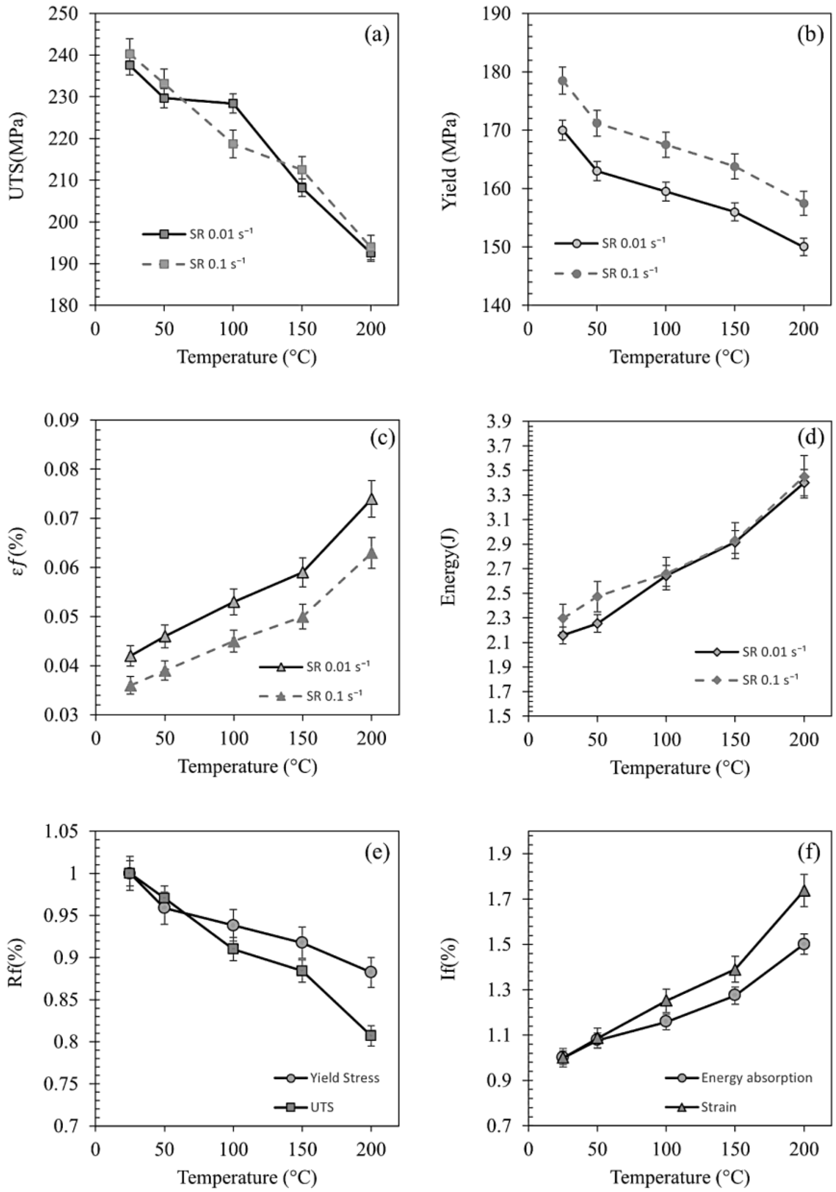

Figure 2-5. Mechanical properties versus tensile test temperature, indicating (a) UTS, (b) yield strength, (c) fracture strain, and (d) absorbed energy before fracture, all measured at two different strain rates. (e) the reduction factor for yield strength and UTS, and (f) the increase factor for absorbed energy and fracture strain

The reduction factors of UTS and yield stress are given in (Figure 2-5-e). Reduction factors decrease with increasing temperature, indicating a decline in strength as the temperature rises. This trend can be attributed to the softening of the material at higher temperatures, which reduces its ability to withstand loads. As the temperature increases, the dislocation movement becomes easier, and the material loses strength due to the relaxation of internal stresses and the potential initiation of recrystallization [159]. As the temperature approaches the upper limit of the tested range, the material experiences significant softening, causing a more pronounced decrease in strength. This non-linear behavior is likely due to different mechanisms, such as dynamic recrystallization and grain boundary sliding, becoming more prominent at higher temperatures, further affecting the material's strength and leading to the observed decrease in the reduction factor.

On the other hand, the strain and energy-increasing factors exhibit an upward trend with temperature. This trend suggests that the material becomes more ductile and capable of absorbing more energy as the temperature rises. The increased ductility allows the material to deform more before reaching the point of failure. At higher temperatures, the activation of thermally-driven mechanisms such as dynamic recrystallization and grain boundary sliding contributes to increased strain and energy absorption.

At elevated temperatures, the strain rate sensitivity of AA 6061-T6 increases due to the combined effects of thermally activated dislocation motion, precipitate coarsening, and dynamic recovery. At low temperatures, plastic deformation is primarily controlled by lattice resistance and interactions with Mg_2Si precipitates, resulting in minimal strain rate sensitivity. However, as temperature increases, thermal energy facilitates dislocation glide, reducing the stress required for plastic flow and making strain rate effects more pronounced. Additionally, the coarsening and partial dissolution of strengthening precipitates weaken their ability to pin dislocations, further increasing strain rate sensitivity. At temperatures above 200°C, dynamic recovery mechanisms become significant, allowing dislocations to rearrange into lower-energy configurations, reducing work hardening and enhancing strain rate dependence. Furthermore, the dominant damage mechanism shifts from particle fracture at room temperature to interfacial decohesion at 300°C, which is inherently more strain-rate sensitive. These factors collectively explain the observed increase in the strain rate sensitivity parameter [160,161].

2.2.5.4 Statistical analysis

A two-way analysis of variance (ANOVA) was performed to evaluate the influence of temperature and strain rate on the material's mechanical properties, including ultimate UTS, yield strength, strain, and energy absorption. ANOVA is a widely used statistical tool that partitions the total variation in the data into components attributable to various sources, allowing for the determination of which factors significantly affect the response variables. In the ANOVA table, Degrees of Freedom (DF) indicate the number of independent values or quantities that can vary in the analysis. Sequential Sum of Squares (Seq SS) represents the portion of the total variation explained by each factor or interaction. Contribution expresses the percentage of the total variation attributable to each factor. Adjusted Sum of Squares (Adj SS) and Adjusted Mean Square (Adj MS) account for the effects of other factors or sources of variability, providing a more accurate estimation of the factor’s influence. The F-Value is the ratio of the adjusted mean square of a factor to the adjusted mean square of the error term, and it serves as an indicator of how much more variability is explained by the factor compared to the residual error. A higher F-value suggests a more significant effect. The P-Value is the probability that the observed effect is due to random chance; a P-value less than 0.05 indicates that the factor has a statistically significant effect on the response variable.

The ANOVA results in Table 2-2 are in accordance with the experimental findings, confirming that temperature has a significant effect on the mechanical properties of the material, while strain rate has minimal impact. For ultimate tensile strength (UTS), temperature accounted for 97.51% of the total variation, with an F-value of 39.45 and a P-value of 0.002, indicating a statistically significant effect. In contrast, strain rate contributed only 0.02% to the variation in UTS, with a P-value of 0.873, which is well above the significance threshold. Similarly, temperature contributed 74.68% to the variation in yield strength, with an F-value of 1629.97 and a P-value of 0.000, showing its dominant influence. The strain rate contributed 25.28% but was still highly significant, with a P-value of 0.000. For strain, temperature contributed 85.98%, while strain rate's effect was minimal at 13.43%. In the case of energy absorption, temperature again accounted for 98.11% of the variation, with a highly significant P-value of 0.000, while strain rate contributed only 1.01%, with a P-value of 0.097, indicating no significant effect. These results demonstrate that while strain rate has little effect on most mechanical properties, temperature is the dominant factor influencing the material's behavior.

Table 2-2. ANOVA table

Source	DF	Seq SS	Contribution	Adj SS	Adj MS	F-Value	P-Value
				UTS			
Source	DF	Seq SS	Contribution	Adj SS	Adj MS	F-Value	P-Value
Strain Rate (1/s)	1	0.48	0.02%	0.48	0.484	0.03	0.873
Temprature (C)	4	2625.84	97.51%	2625.84	656.460	39.45	0.002
Error	4	66.56	2.47%	66.56	16.639		
Total	9	2692.88	100.00%				
				Yield			
Source	DF	Seq SS	Contribution	Adj SS	Adj MS	F-Value	P-Value
Strain Rate (1/s)	1	160.000	25.28%	160.000	160.000	2206.90	0.000
Temprature (C)	4	472.690	74.68%	472.690	118.172	1629.97	0.000
Error	4	0.290	0.05%	0.290	0.072		
Total	9	632.980	100.00%				
				Strain			
Source	DF	Seq SS	Contribution	Adj SS	Adj MS	F-Value	P-Value
Strain Rate (1/s)	1	0.000168	13.43%	0.000168	0.000168	90.86	0.001
Temprature (C)	4	0.001077	85.98%	0.001077	0.000269	145.49	0.000
Error	4	0.000007	0.59%	0.000007	0.000002		
Total	9	0.001252	100.00%				
				Energy absorption			
Source	DF	Seq SS	Contribution	Adj SS	Adj MS	F-Value	P-Value
Strain Rate (1/s)	1	0.01884	1.01%	0.01884	0.018836	4.65	0.097
Temprature (C)	4	1.82147	98.11%	1.82147	0.455366	112.43	0.000
Error	4	0.01620	0.87%	0.01620	0.004050		
Total	9	1.85650	100.00%				

Although the effect of strain rate on the material's mechanical properties is minimal, it remains statistically significant and quantifiable. The main effects plots in Figure 2-6 show that an increase in strain rate slightly raises the yield stress, while its impact on UTS is negligible. Conversely, strain decreases with increasing strain rate, indicating reduced ductility. Energy absorption also exhibits a minor increasing trend with strain rate.

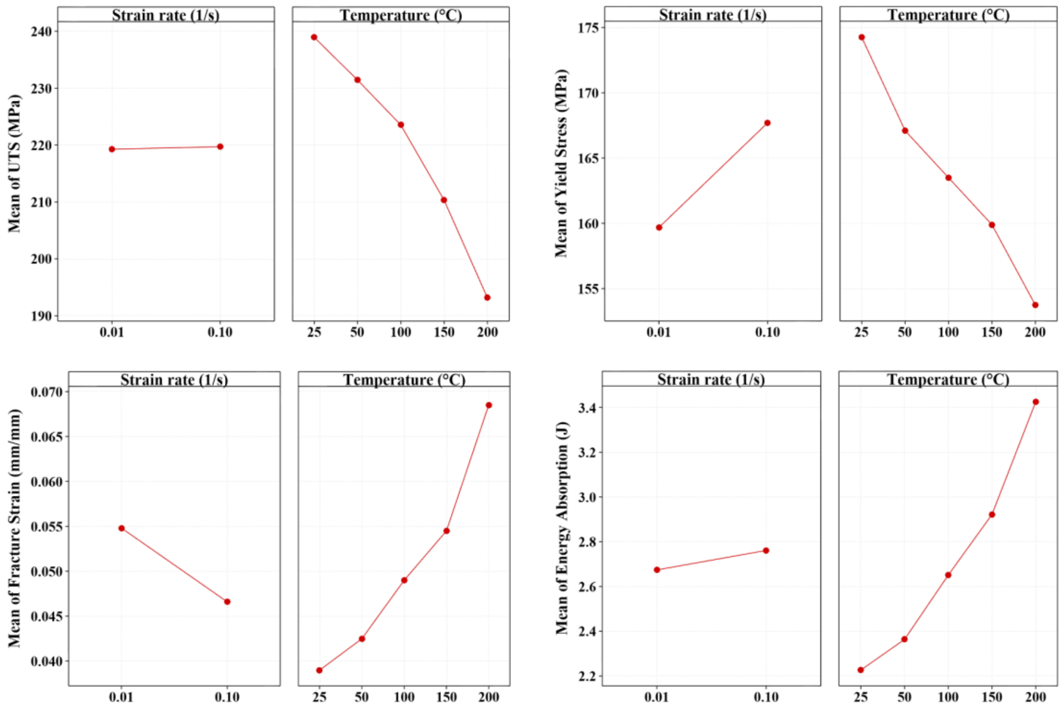

Figure 2-6. Main effect plots for a) UTS, b) yield strength, c) strain, d) energy absorption

2.2.5.5 Fractography

Figure 2-7-a presents a representative fracture image for the material tested at both room temperature and 50°C, illustrating that fractures originated from the HAZ. Figure 2-7-c shows the low magnification of the fractured surface at room temperature. At room temperature, the dominant fracture mode is cleavage, with crack propagation following specific crystallographic planes, typical in materials with a high brittle-to-ductile transition temperature. The fracture surface shows sharp, jagged edges indicative of rapid crack propagation with minimal plastic deformation. Shiny, flat facets interspersed with river patterns map the direction of crack growth. The smoothness and flatness of these facets indicate minimal energy absorption before fracture, with little to no plastic deformation. Bonds between atoms break suddenly, leading to rapid crack propagation. The overall fracture pattern and extent of cleavage across the surface emphasize its brittle nature. At higher magnification, as shown in Figure 2-7-d, specific fracture features such as river markings and sharp cleavage facets are visible. Figure 2-7-e, at low magnification of the fracture surface at 50°C, still shows areas with brittle characteristics, but the initiation of micro void coalescence can be seen. These microvoids, forming at the sites of particles or second-phase inclusions within the metal matrix, begin to grow and link under applied stress, forming dimples upon fracture. The appearance of these dimples, even if sparse, marks the beginning of energy absorption through mechanisms other than cleavage. This slight temperature increase reduces the material's yield strength slightly, allowing for more noticeable plastic deformation. Figure 2-7-e displays a mix of brittle characteristics with areas beginning to show ductility. Figure 2-7-f shows isolated and sparse dimples at high magnification, indicating areas where microvoids have started to form and grow, marking the initial stages of plastic deformation. Figure 2-7-b compares the tensile diagram of the material at room temperature with 50°C, showing an increase in fracture strain, indicating a more ductile fracture. The slight transition to a more ductile fracture is observable in Figure 2-7-e and Figure 2-7-f, which show surface fractography at 50°C. Specifically, in Figure 2-7-f compared to Figure 2-7-d, larger dimples are observed, indicating a more ductile fracture.

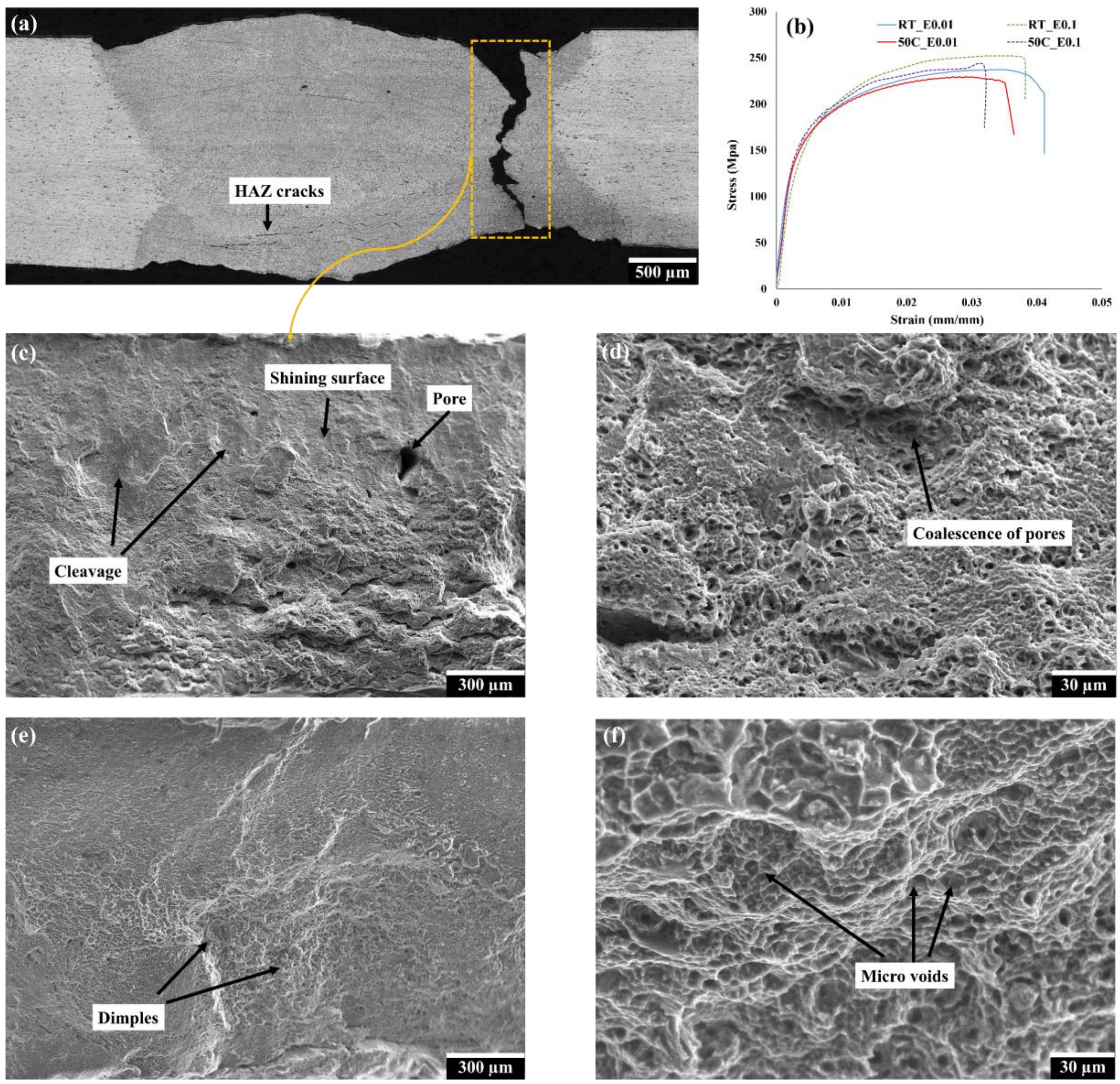

Figure 2-7. (a) Fractured area from HAZ at room temperature, (b) Tensile test diagram, (c) Top view of the fractured surface at room temperature at low magnification, (d) Top view of the fractured surface at room temperature at high magnification, (e) Top view of the fractured surface at 50°C at low magnification, (f) Top view of the fractured surface at 50°C at high magnification.

At 100°C, the fracture surface shown in Figure 2-8-a further develops towards a ductile failure mode, showing a slight degree of ductility compared to the tensile load direction, indicating a more ductile fracture compared to Figure 2-7-a. Figure 2-8-b shows the tensile test results at 100°C, which correlate with the SEM images by indicating an increase in fracture strain and reduction in tensile strength, characteristic of a more ductile material behavior. Figure 2-8-c, an SEM image, shows the low magnification of the fractured surface area with a clearer presence of ductile features such as larger and more evenly distributed dimples, indicating a significant amount of plastic deformation. This image shows a mixture of larger dimples and regions still exhibiting some brittle characteristics, like minor cleavage facets. The dimples are more pronounced and evenly distributed, formed by the coalescence of micro-voids under tensile stress. This indicates a significant amount of energy absorption and plastic deformation, as the elevated temperature facilitates easier dislocation movement, reducing the material's propensity for sudden brittle failure. This image depicts a mixed fracture surface with regions of ductility interspersed with residual brittle features, representing an intermediate stage of the ductile transition. Figure 2-8-d, at high magnification, reveals the morphology of the dimples and the presence of tear ridges, which signify where the material has undergone considerable stretching and necking prior to failure. Additionally, tear ridges, which are raised lips around the dimples, are also visible, indicating where the material has stretched and necked before finally fracturing.

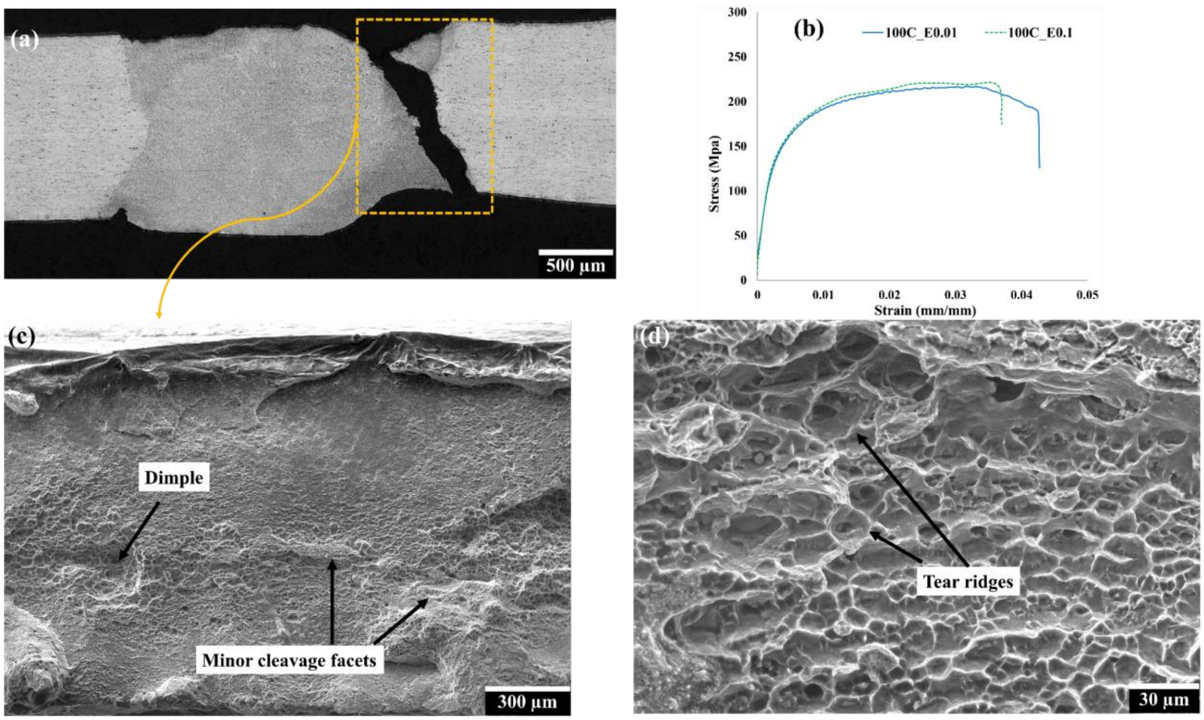

Figure 2-8. (a) Fractured area from HAZ at 100°C, (b) Tensile test diagram, (c) Top view of the fractured surface at low magnification, (d) Top view of the fractured surface at high magnification

Figure 2-9-a presents a representative fracture image for the material tested at 150°C and 200°C, highlighting significant changes in fracture location compared to room temperature and 100°C. It can be observed clearly that the fracture occurred in the FZ rather than HAZ as seen in Figure 2-7-a, Figure 2-8-a. The transition from HAZ fracture to FZ could be due to the presence of cracks as shown in Figure 2-9-a. At these elevated temperatures, the fracture surface exhibits increased ductility, characterized by significant dislocation movement. The fracture angle, approaching 45 degrees, suggests the presence of both shear and tensile stress components, indicative of a mixed-mode fracture. This mixed-mode fracture, combining elements of both Mode I (opening) and Mode II (sliding) fractures, results in a more ductile failure mechanism [162]. The enhanced ductility at 150°C and 200°C allows for greater plastic deformation before fracture, in contrast to the more brittle fractures observed at room temperature and 100°C. The higher fracture angle and the presence of dislocation movement are clear markers of this transition from brittle to ductile fracture behavior.

Figure 2-9-c and Figure 2-9-e show the low magnification of the fracture surfaces at 150°C and 200°C, respectively. The two FZs from the first laser track and the second laser track can be clearly distinguished in the figures. The second FZ is characterized by shear lips and tear ridges, indicating shear deformation. The presence of cracks in this zone is pronounced, particularly at the last step of deformation, acting as stress concentrators and initiating the fracture process. These features lead to a brittle fracture mechanism in this region. In contrast, the first FZ shows a larger surface area with fewer cracks and cleavage surfaces, indicating a mixed-mode rupture that combines both brittle and ductile characteristics. This suggests that while there is some plastic deformation, brittle fracture features are still present. In Figure 2-9-c at 150°C, the fracture surface displays a rough texture with large dimples throughout, suggesting a high degree of toughness and energy absorption. However, Figure 2-9-e at 200°C shows a thoroughly ductile fracture surface, characterized by very large, well-formed dimples that are homogeneously distributed across the fracture face. The material at this temperature absorbs the maximum amount of energy before fracturing, which is evident from the thick, rounded walls of the dimples and the extensive plastic deformation. The material's ability to deform plastically is maximized due to the high mobility of dislocations and the softening of the material as it approaches or exceeds its recrystallization temperature. This temperature represents a regime where the mechanical behavior of the material is dominated by ductile mechanisms, highlighting its high toughness and resilience under tensile stress.

Figure 2-9-d and Figure 2-9-f show high magnification of the fracture surfaces at 150°C and 200°C, respectively. Upon examining these fracture surfaces at higher magnification, increased porosity and more prominent microvoids were observed at 150°C and 200°C, indicating a shift toward ductile fracture mechanisms. Higher temperatures facilitated more significant plastic deformation, as evidenced by larger and more numerous microvoids, especially at 200°C. This transition from a mixed mode with both brittle and ductile features at 150°C to a predominantly ductile fracture at 200°C highlighted the material's enhanced ability to absorb energy before fracturing, thereby improving its toughness at higher temperatures. Furthermore, Figure 2-9-d, the high magnification view, illustrates deep dimple formation and potential secondary features such as microcracks emanating from the dimple edges, reflecting the intense stress experienced by the material before failure. Figure 2-9-f emphasizes the uniform ductility across the fracture surface, showcasing the material's resilience and toughness at elevated temperatures. The high-magnification SEM image in Figure 2-9-d revealed the thick, rounded walls of the dimples, which were evidence of extensive plastic flow and maximum energy absorption before fracture.

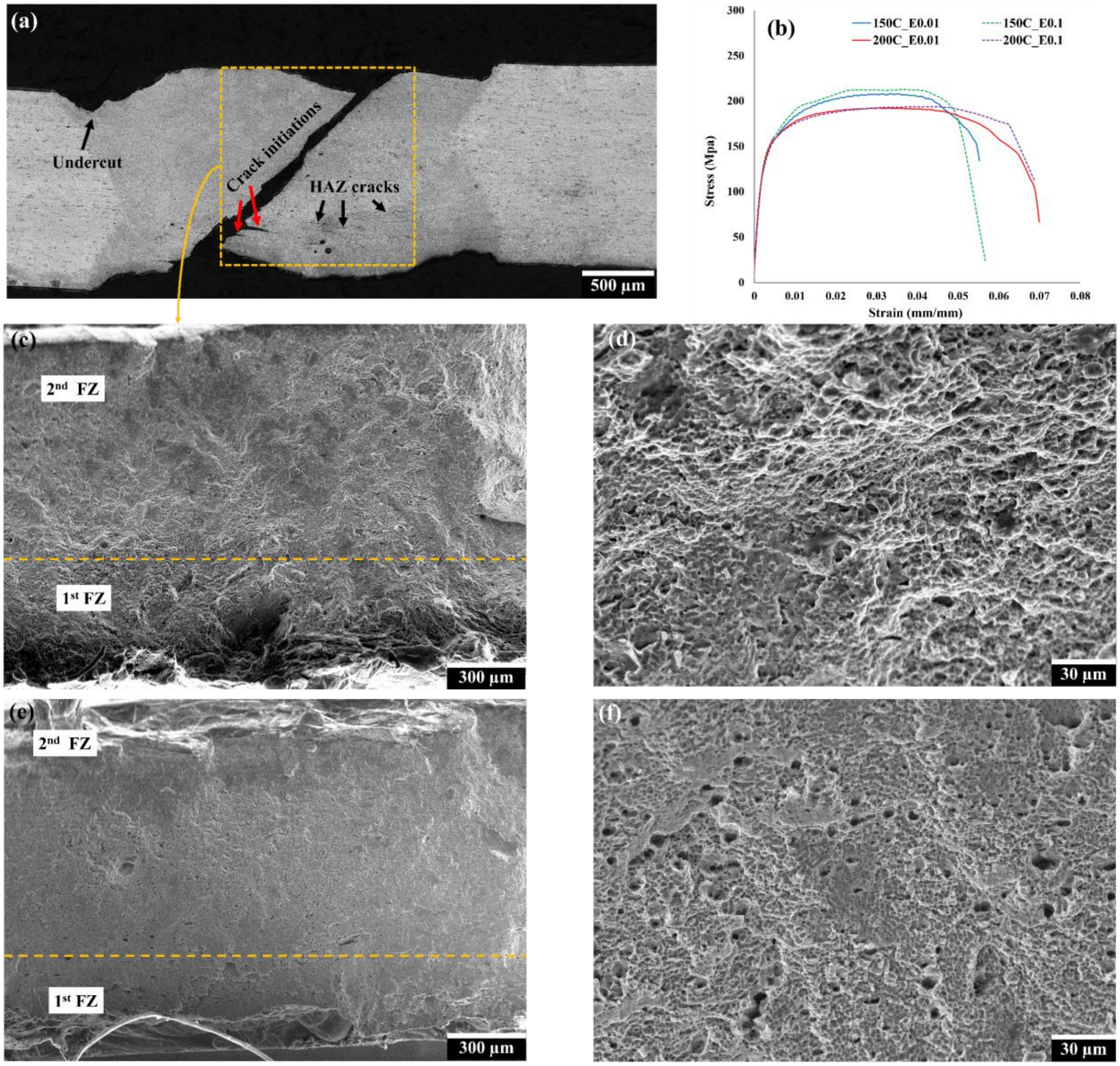

Figure 2-9. (a) Fractured area from FZ at 150°C, (b) Tensile test diagram, (c) Top view of the fractured surface at 150°C at low magnification, (d) Top view of the fractured surface at 150°C at high magnification, (e) Top view of the fractured surface at 200°C at low magnification, (f) Top view of the fractured surface at 200°C at high magnification.

2.2.6 Conclusion

This study investigates the fracture behavior of double-sided butt joints in aluminum alloy 6061-T6 under tensile load at elevated temperatures ranging from 25°C to 200°C, with strain rates of 0.01 and 0.1 s^{-1}. The key conclusions drawn from the investigation are as follows:

- The microstructure analysis of double-sided laser-welded butt joint aluminum revealed an H-shaped HAZ that separated the FZs created by the two laser passes. While the welding parameters were optimized to prevent the formation of solidification cracks, the sequential laser passes led to the development of microcracks along the grain boundaries in the central part of the HAZ. The microhardness in this area was found to be minimized due to the formation of cracks.
- Regarding the effect of the temperature, as the temperature increases from room temperature to 200°C, a significant reduction in yield strength is observed, with a corresponding increase in strain and energy absorption.
- The strain rate range considered in this study (0.01–0.1 s^{-1}) is within the quasi-static regime, where the strain rate has a minimal effect on UTS and energy absorption. However, strain rate does significantly affect yield stress and fracture strain, with lower strain rates resulting in lower yield stress and higher fracture strain. These results suggest that strain rate is more influential on the plastic deformation characteristics than on strength or energy absorption in this strain rate range.
- Elevated temperatures have a significant impact on the principal fracture mechanism, transitioning from HAZ to FZ. At lower temperatures, geometrical defects like undercutting pose a greater risk of fracture, whereas, at higher temperatures (e.g., 150°C), fractures become less sensitive to geometrical defects and more sensitive to microstructural defects.

CHAPITRE 3
ANALYSE COMPARATIVE DES PROPRIETES EN TRACTION A HAUTE TEMPERATURE DES SOUDURES AU LASER DES ALLIAGES AA5052 ET AA6061 POUR DES APPLICATIONS AUTOMOBILES

Pedram Farhadipour[1], Narges Omidi[1], Noureddine Barka[1], Mohamad Idriss[2], François Nadeau[2], Abderrazak El Ouafi[1]

[1] Université du Québec à Rimouski, Québec, Canada

[2] Conseil national de recherches Canada, Québec, Canada

3.1 Résumé en français du troisième article

Cette étude examine les propriétés en traction à haute température des alliages d'aluminium AA5052-H36 et AA6061-T6 soudés au laser, en utilisant une analyse expérimentale et statistique. Des essais de traction ont été réalisés à des températures allant de 25°C à 300°C, avec des vitesses de déformation correspondantes de 0,01 s^{-1} et 0,1 s^{-1}. Les résultats montrent que l'AA5052-H36 présente une résistance mécanique supérieure à celle de l'AA6061-T6, avec une diminution quasi linéaire de la résistance ultime à la traction, passant d'environ 273 MPa à 100°C à 108 MPa à 300°C, soit une réduction d'environ 60 %. L'AA5052-H36 affiche également une augmentation constante de l'allongement à la rupture, passant de 0,14 à 100°C à 0,37 à 300°C. En revanche, l'AA6061-T6 présente une diminution non linéaire de la résistance ultime à la traction, réduite de 51 %, passant de 220 MPa à 100°C à 110 MPa à 300°C, ainsi qu'une augmentation de l'allongement à la rupture de 0,05 à 100°C à 0,07 à 300°C. Ce comportement non linéaire est lié à la dissolution des phases β'' et à la précipitation subséquente des phases β', comme révélé par la courbe de calorimétrie différentielle à balayage. L'analyse statistique confirme que la température est le facteur dominant influençant la performance en traction, avec une contribution notable des

transformations de phase observées sur la courbe de calorimétrie différentielle à balayage. L'analyse de l'absorption d'énergie met en évidence les avantages de l'AA5052-H36, qui absorbe beaucoup plus d'énergie avant rupture que l'AA6061-T6 en raison de sa plus grande capacité de déformation plastique. À 250°C, l'AA5052-H36 absorbe jusqu'à 13,3 J, tandis que l'AA6061-T6 atteint un maximum de 3,3 J à la même température. Les deux alliages présentent une absorption d'énergie maximale à 250°C, avec une augmentation progressive jusqu'à cette température. Toutefois, au-delà de 250°C, l'absorption d'énergie diminue considérablement. En conclusion, bien que l'AA5052-H36 puisse offrir de meilleures performances en traction à haute température par rapport à l'AA6061-T6, le choix de l'alliage pour des applications au-delà de 250°C doit être fait en tenant compte des compromis entre résistance, résistance à la corrosion et fabricabilité, afin d'éviter d'éventuelles défaillances liées au fluage.

Cet article, intitulé « *Comparative Analysis of the High-Temperature Tensile Properties of Laser-Welded AA5052 and AA6061 for Automotive Applications* », a été accepté pour publication dans *Proceedings of the Institution of Mechanical Engineers, Part C: Journal of Mechanical Engineering Science* et publié en ligne en mars 2025. En tant que premier auteur, mes contributions comprennent une recherche de pointe, la réalisation des essais expérimentaux, l'analyse statistique, l'interprétation des résultats et la rédaction du manuscrit. La Dr Narges Omidi, deuxième auteure, a révisé l'article. Le professeur Noureddine Barka, troisième auteur, a proposé l'idée originale, développé la méthodologie et révisé l'article. Dr Mohamad Idriss et Dr François Nadeau, respectivement quatrième et cinquième auteurs, ont apporté des conseils industriels, amélioré la méthodologie et contribué à la révision de l'article. Le professeur Abderrazak El Ouafi, sixième auteur, a également participé au développement de la méthodologie.

3.2 Comparative Analysis of the High-Temperature Tensile Properties of Laser-Welded AA5052 and AA6061 for Automotive Applications

3.2.1 Abstract

This study investigates the high-temperature tensile properties of laser-welded AA5052-H36 and AA6061-T6 aluminum alloys, utilizing experimental and statistical analysis. Tensile tests were conducted at temperatures ranging from 25℃ to 300℃ at corresponding strain rates of 0.01 s^{-1} and 0.1 s^{-1}. The results indicate that AA5052-H36 exhibits superior mechanical strength compared to AA6061-T6, with a near-linear decrease in ultimate tensile strength, showing a reduction of approximately 60% from 273 MPa at 100℃ to 108 MPa at 300℃. AA5052-H36 also shows consistent increases in fracture strain across the tested conditions, with fracture strain rising from 0.14 at 100℃ to 0.37 at 300℃. In contrast, AA6061-T6 displays a non-linear decline in UTS, dropping by 51%, from 220 MPa at 100℃ to 110 MPa at 300℃, and an increase in fracture strain from 0.05 at 100℃ to 0.07 at 300℃. This non-linear behavior is linked to the dissolution of β'' phases and the subsequent precipitation of β' phases, as revealed by the differential scanning calorimetry curve. Statistical analysis confirms that temperature is the dominant factor influencing tensile performance, with notable contributions from phase transformations observed in the DSC curve. Energy absorption analysis highlights the advantages of AA5052-H36, which absorbs considerably more energy before failure compared to AA6061-T6, due to its greater plastic deformation capacity. AA5052-H36 absorbs up to 13.3J at 250°C, while AA6061-T6 absorbs a maximum of 3.3J at the same temperature. Both alloys show maximum energy absorption at 250℃, with increasing temperature leading to a rise in absorbed energy up to 13.3J. However, beyond 250°C, the energy absorption decreases substantially. In conclusion, while AA5052-H36 may offer superior performance in high-temperature tensile loading compared to AA6061-T6, the choice of alloy for applications above 250°C should be made with careful consideration of the trade-offs, including strength, corrosion resistance, and manufacturability, to prevent possible creep-related failures.

Keywords: High-temperature tensile properties, Laser welding, AA5052-H36, AA6061-T6, Fractography

3.2.2 Abbreviations

AA	Aluminum alloy
Al	Aluminum
ANOVA	Analysis of variance
Cr	Chromium
Cu	Copper
CW	Continuous wave
DSC	Differential scanning calorimetry
EDS	Energy dispersive spectroscopy
Fe	Iron
FZ	Fusion zone
GP	Guinier-preston
HAZ	Heat-affected Zone
Mg	Magnesium
Mn	Manganese
SEM	Scanning electron microscopy
Si	Silicon
SR	Strain rate
UTS	Ultimate tensile strength
Zn	Zinc

3.2.3 Introduction

Aluminum alloys AA5052 and AA6061 are extensively utilized in the automotive industry, particularly in the fabrication of tailor-welded blanks [163–165]. AA6061-T6 aluminum alloy has an ultimate-to-yield strength ratio of 1.2, offering a balance of high strength, good ductility, and work-hardening capability. AA6061 is a heat-treatable alloy that benefits from precipitation hardening, significantly improving its strength and hardness [166]. The precipitation sequence in AA6061 aluminum alloy begins with the formation of

Guinier-Preston (GP) zones, which are small, coherent clusters of magnesium and silicon atoms within the aluminum matrix. As the alloy undergoes aging, these GP zones evolve into the metastable β'' phase, characterized by its needle-like morphology, which significantly enhances the alloy's strength by impeding dislocation motion. With further aging or at higher temperatures, the β'' phase transforms into the β' phase, which is less coherent but still contributes to the material's strength, albeit to a lesser degree. Eventually, the alloy reaches the stable β phase, marking the onset of overaging, where the strength of the material decreases due to the coarsening of precipitates. This sequence of precipitation phases is critical to the mechanical performance of AA6061, particularly in optimizing its strength and hardness through heat treatment [167–169]. This alloy is characterized by its high strength-to-weight ratio, good machinability, and superior weldability, making it suitable for various structural applications.

AA5052-H36 is renowned for its exceptional corrosion resistance, high fatigue strength, and excellent weldability, making it a preferred choice in marine and industrial applications. The alloy exhibits moderate ductility, allowing for some degree of plastic deformation before failure [166]. AA5052 is a non-heat-treatable aluminum alloy, with mechanical properties primarily derived from solid solution strengthening due to its magnesium content (2.2% to 2.8%). Magnesium atoms dissolve in the aluminum matrix, creating lattice distortions that increase yield and tensile strength without significantly reducing ductility. This gives AA5052 a good balance of strength and formability. The magnesium content is kept below the solubility limit, ensuring stability across a range of temperatures without the need for heat treatment [133,170]. Unlike precipitation-hardened alloys like AA6061, AA5052 remains stable under typical service conditions, making it a reliable choice for applications requiring consistent mechanical properties in varying environments [168].

Laser welding is an efficient and precise method for joining materials, particularly in the context of tailor-welded blanks within the automotive sector. The process offers several advantages, including high welding speeds, deep penetration, and minimal thermal distortion, making it an ideal technique for producing high-quality joints in components with varying thicknesses [73]. Previous studies have extensively investigated the laser welding of aluminum alloys such as AA5052 and AA6061, primarily focusing on their behavior at room temperature. For AA6061, it has been observed that the microstructure in the welding zone typically consists of a dendritic structure due to the rapid solidification of the molten metal during the welding process. The HAZ often experiences significant microstructural changes, including the dissolution of strengthening precipitates like β'' and β' phases, which can lead to a reduction in mechanical properties such as hardness and tensile strength [171]. At room temperature, AA6061 welds are characterized by lower strength and ductility compared to the base material, primarily due to the over aging effect in the HAZ and the presence of coarse precipitates in the welded metal. One key concern with AA6061 is the formation of porosity due to magnesium evaporation during the welding process. Narsimhachary et al. [172] investigated the impact of temperature control during welding to achieve a stable keyhole and minimize defects such as porosity and cracks. Their findings indicated that by optimizing temperature, porosity-free and crack-free welds could be achieved, although there was a significant drop in overall hardness in HAZ. Gündoğdu et al. [173] further explored the influence of laser welding speed on pore formation. Hirose et al. [174] reported that the softening observed in the HAZ is caused by the dissolution of strengthening β'' (Mg_2Si) precipitates due to the heat input from welding. They noted that this softening was linked to the reversion of β'' precipitates. Additionally, Wang et al. [74] studied the effect of beam oscillation patterns on weld quality, finding that circular oscillation resulted in the soundest welds with superior mechanical properties. These studies collectively highlight the challenges and considerations involved in optimizing the laser welding process for AA6061 to maintain its mechanical integrity. Similarly, studies on AA5052-H36 laser welds have shown that the microstructure is predominantly composed of elongated grains in the weld zone, with the HAZ displaying some grain growth due to the thermal cycles during welding. Unlike AA6061, AA5052 does not undergo significant precipitation hardening, and its mechanical properties are largely retained after welding. However, the weld zone often exhibits slightly reduced ductility and strength compared to the base material [175], attributed to the coarsening of grains and the loss of solid solution strengthening effects in the HAZ. Idriss et al. [86] found that the microstructure of laser-welded AA5052-H36 typically exhibits a dendritic structure in the FZ with equiaxed grains developing in the HAZ. The mechanical properties are notably affected by the welding process, with the base material having a yield strength of 230 MPa, UTS of 297 MPa, and a fracture strain at break of 7%. After welding, the microhardness in the FZ generally decreases due to the dissolution and evaporation of magnesium, which diminishes the solid solution strengthening effect. Despite this, the study noted that with optimal welding parameters, such as using an oscillatory welding pattern, the FZ and HAZ could achieve enhanced hardness values, sometimes even surpassing those of the base material, depending on the specific welding conditions.

Previous studies successfully optimized the processing parameters for welding, achieving maximum mechanical strength comparable to the base material while also reducing weld defects. However, in the production of tailor-welded blanks, post-welding hot deformation processes are often required, necessitating a comprehensive understanding of the mechanical properties of the welded materials at elevated temperatures. Despite the critical importance of this knowledge, there is a lack of extensive studies on the mechanical behavior of laser-welded AA5052 and AA6061 under high temperatures and tensile loads. This study aims to investigate the effects of temperature and strain rate on the tensile properties of these two aluminum alloys post-laser welding. By comparing the mechanical performance of the welded materials to their respective base metals, this research seeks to determine which alloy demonstrates superior mechanical properties, such as strength and ductility, under hot forming conditions. This comparative analysis will provide valuable insights for selecting the most suitable welded material for high-temperature applications, such as welded engine components and exhaust systems, in the automotive industry.

3.2.4 Materials and method

In this study, 1.5 mm thick sheets of AA5052-H36 and AA6061-T6 aluminum alloys were used. The elemental composition of these alloys were provided based on standard compositional data for these alloys, which was confirmed by datasheet from supplier and EDS analysis; presented in Figure 3-1a. Laser welding was performed as depicted in Figure 3-1b, using a Nd: YAG laser machine with an IPG Photonics YLS3000 laser source and a FANUC robotic arm with 0.07 mm precision. The process employed a 100 μm continuous wave (CW) Nd: YAG optical fiber with an oscillation frequency of 300 Hz. The laser welding parameters, optimized in previous research of the authors [133], were 2500 W laser power, 5 m/min travel speed, 6.0 mm focal position, and 1.5 mm oscillation amplitude.

Tensile test specimens were prepared according to the ASTM B557 standard [135] (Figure 3-1c) and tested at various temperatures (25°C, 100°C, 150°C, 200°C, 250°C, and 300°C) and strain rates (0.01 s^{-1} and 0.1 s^{-1}), with 3 repetition at each condition. The tests were conducted using an MTS 809 tensile test machine, which has a maximum load capacity of 100 kN. An induction heating machine was employed to achieve and maintain the desired test temperatures. The temperature of the specimens was monitored and controlled using thermocouples attached to the specimens. Microstructural observation was conducted using an optical microscopy, and fractography was performed using an SNE-4500M electron microscope. The Vickers microhardness profile of the welded area was measured using a Clemex MMT-X7B microhardness tester, applying a 100 g force indentation with a holding time of 10 seconds.

(a)

Element	Al	Cr	Cu	Fe	Mg	Mn	Si	Zn
AA5052 (wt. %)	Balance	0.35	0.1	0.4	2.6	0.1	0.25	0.1
AA6061 (wt. %)	Balance	0.3	0.25	0.2	1.2	0.1	0.75	0.2

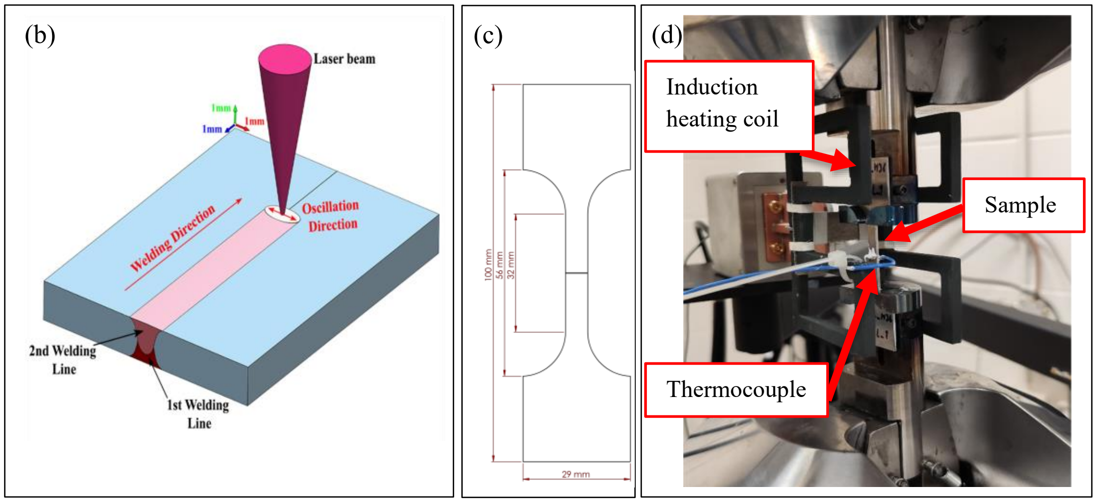

Figure 3-1. Experimental setup of the study: (a) chemical composition of the materials, (b) weld configuration, (c) tensile test sample's dimension, (d) high temperature tensile test setup

All DSC analyses were performed using a Mettler Toledo DSC instrument equipped with an HSS8 sensor. Samples analyzed consisted of 4 mm diameter disks punched directly from the heat-treated sheet samples. Standard 40 µL pure aluminum crucibles, in a semi-autogenic atmosphere, were used to contain the sample, while an empty pan (i.e., air) was used as a reference material. The temperature interval from -30°C to 500°C was considered at a 10°C/min heating rate. Nitrogen was allowed to circulate around the furnace area to prevent ice buildup while the instrument operated at temperatures below 0°C. The DSC curves obtained were normalized to the sample mass and a spline baseline was subtracted to eliminate any drift caused by the variation of the specific heat with the temperature.

Finally, the statistical analysis was used to validate and further analyze the experimental results, ensuring the reliability and robustness of the conclusions drawn from the data. statistical analysis using Analysis of Variance (ANOVA) was conducted to assess the influence of temperature and strain rate on the UTS and fracture strain of welded AA5052-H36 and AA6061-T6. The ANOVA table includes key terms such as DF (Degrees of Freedom), which represents the number of independent values that can vary; Seq SS (Sequential Sum of Squares), quantifying the variation attributed to each factor; and Contribution, indicating the percentage of total variation explained by each factor. Adj SS (Adjusted Sum of Squares) accounts for the influence of other factors, while Adj MS (Adjusted Mean Square) provides a measure of variance for each factor. The F-Value compares the variation due to the factor with the error, and the P-Value determines the statistical relevance of each factor, with values typically less than 0.05 indicating a substantial effect.

3.2.5 Result and discussion

3.2.5.1 Tensile test

Figure 3-2 shows the tensile test curves of the materials under different tensile condition. Figure 3-2a, b, and c present the tensile test results for AA6061-T6, while Figure 3-2d, e, and f show the results for AA5052-H36.

A comparison between the welded material and the base material clearly shows that the base material possesses better mechanical properties than the welded material across different temperatures. This difference is mainly attributed to the presence of weld defects, which leads to a reduction in mechanical properties. Additionally, the welding process introduces changes in the temper of the material and can lead to the evaporation of certain elements, depending on the specific grade of the material. This is evident in the case of AA6061, where Figure 3-2a illustrates the mechanical properties of the base material, and Figure 3-2b depicts those of the welded material, at various temperatures. The UTS and fracture strain are consistently lower in the welded material compared to the base material across this temperature range. For example, at 100°C, the UTS of the base material is 340 MPa, while it drops to 220 MPa in the welded material. At 300°C, the UTS of the base material is 120 MPa, whereas the welded material shows a slightly lower UTS of 110 MPa. Similarly, welding has a noticeable impact on fracture strain, with fracture strain increasing as the temperature rises. At 100°C, the fracture strain for the base material is 0.18, while it decreases to 0.05 for the welded material. At 300°C, the fracture strain for the base material is 0.32, compared to just 0.07 for the welded material. Notably, as the temperature increases from 100°C to 300°C, the difference in mechanical properties between the base and welded materials becomes smaller. This indicates that at higher temperatures, the mechanical properties of the base and welded materials converge, with the values getting closer to each other. This trend, as shown in Figure 3-3, suggests that the detrimental effects of welding on AA6061-T6 become less pronounced as the temperature increases.

Similarly, for AA5052-H36, a comparison between Figure 3-2d (base material) and Figure 3-2e (welded material) reveals a similar trend, though the reduction in mechanical properties due to welding is less severe. The UTS of the welded AA5052-H36 decreases slightly across the temperature range. For instance, at 100°C, the UTS of the base material is 330 MPa, while it drops to 273 MPa for the welded material. At 300°C, the UTS of the base material further decreases to 115 MPa, with the welded material showing a slightly lower UTS of 108 MPa. Similarly, the fracture strain is also affected by welding, though the differences become less pronounced at higher temperatures. At 100°C, the fracture strain of the base material is 0.22, while it decreases to 0.14 for the welded material. At 300°C, the fracture strain for the base material is 0.44, compared to 0.37 for the welded material. This indicates that, although the base material generally exhibits higher fracture strain than the welded material, the gap between them narrows as the temperature increases (Figure 3-3).

The effects of increasing the strain rate from 0.01 s^{-1} to 0.1 s^{-1} on the mechanical properties and tensile behavior of the materials are negligible. Both AA6061-T6 and AA5052-H36 consistently show similar behavior at higher strain rates as they do at lower strain rates. Figure 3-2c shows the effect of a higher strain rate on the welded AA6061-T6 material. When we compare this with Figure 3-2b, which represents a lower strain rate for the same material, we observe that increasing the strain rate from 0.01 s^{-1} to 0.1 s^{-1} has a negligible impact on the mechanical properties. The material's behavior remains almost unchanged, indicating that AA6061-T6 is not significantly affected by variations in strain rate. Similarly, Figure 3-2f illustrates the effect of a higher strain rate on the welded AA5052-H36 material. When compared to Figure 3-2e, which represents a lower strain rate for AA5052-H36, the results show a minimal change in mechanical properties with the increased strain rate. This consistency across different strain rates suggests that AA5052-H36, like AA6061-T6, maintains stable mechanical performance within the range of strain rates tested. This minimal variation can be attributed to the materials' relatively stable microstructure and the fact that the strain rate range tested is within the regime where strain rate sensitivity is minimal for these alloys. Such a finding is also reported in the literature [176,177]

Figure 3-3 illustrates the reduction trend in the UTS for all materials at a strain rate of 0.01 s^{-1}. Figure 3-3a shows the UTS reduction for both the welded and base AA6061-T6. This figure indicates an approximately linear reduction in UTS with increasing tensile temperature. It is also evident that as the temperature increases, the UTS values for the welded and base materials converge, indicating that the strength difference between the welded and base AA6061-T6 decreases at higher temperatures. Similarly, Figure 3-3b depicts the UTS reduction for both the welded and base AA5052-H36. This figure also demonstrates a linear reduction in UTS with increasing temperature. However, when comparing the trends for AA5052-H36 and AA6061-T6, it is clear that the UTS for the welded AA5052-H36 remains much closer to that of the base material across the temperature range. This indicates that AA5052-H36 retains more of its original strength after welding compared to AA6061-T6. The comparison between these two figures highlights that AA5052-H36 is a superior candidate for applications requiring high-temperature performance and post-welding strength retention. The smaller reduction in UTS and the closer alignment between the welded and base material strengths at elevated temperatures make AA5052-H36 more suitable than AA6061-T6 for such applications.

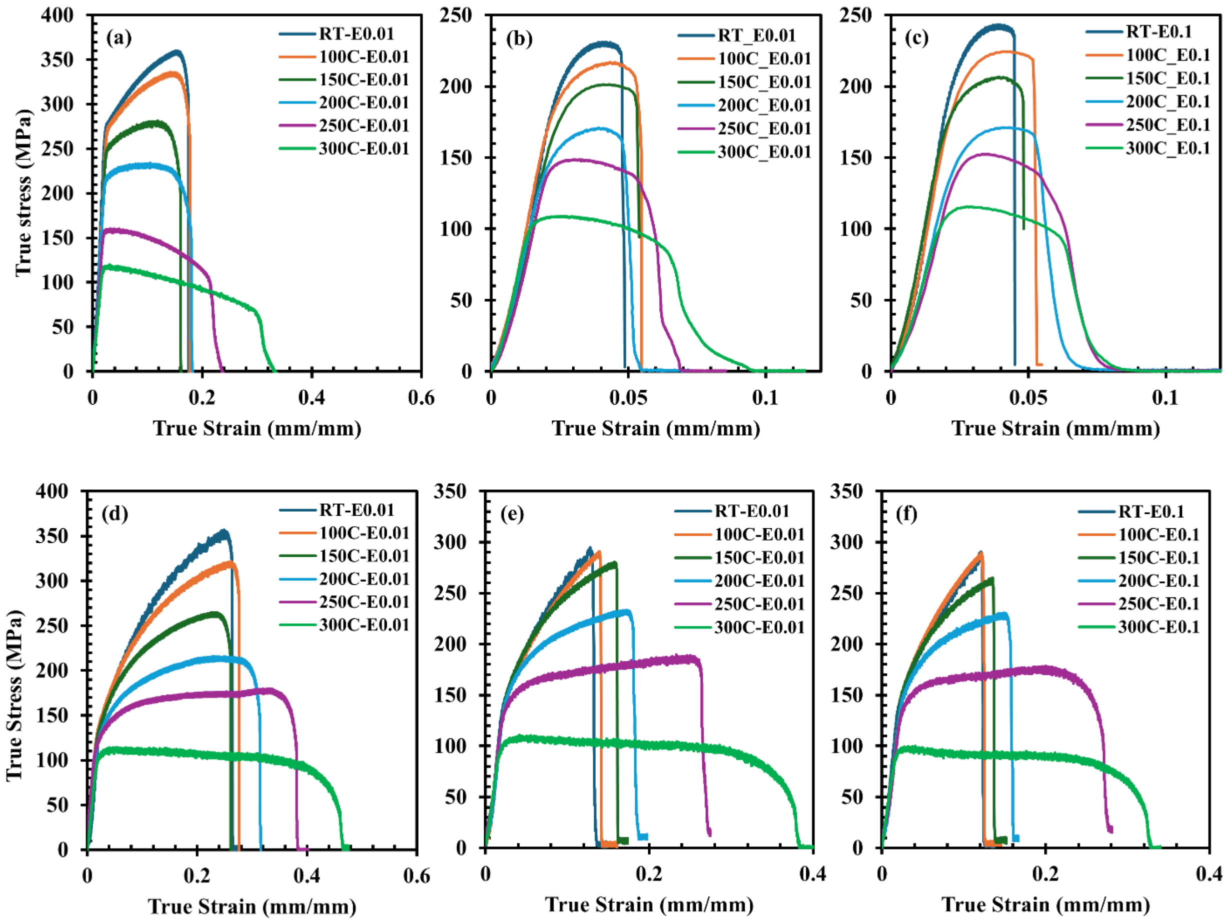

Figure 3-2. (a) Base Material AA6061-T6 at strain rate 0.01s^{-1} (b) Butt joint welded AA6061-T6 at strain rate 0.01s^{-1} (c) Butt joint welded AA6061-T6 at strain rate 0.1s^{-1} (d)Base Material AA5052-H36 at strain rate 0.01s^{-1} (e) Butt joint welded AA5052-H36 at strain rate 0.01s^{-1} (f) Butt joint welded AA5052-H36 at strain rate 0.1s^{-1}

Figure 3-3c and d illustrate the fracture strain behavior of AA6061 and AA5052 alloys across varying temperatures. In Figure 3-3c, which displays the fracture strain trends for AA6061, the base material shows a marked increase in fracture strain with rising temperature, reflecting enhanced ductility at elevated temperatures. In contrast, the welded AA6061 material consistently exhibits low fracture strain values, remaining below 0.1 across all temperatures. The reduction in fracture strain for the welded material is likely due to the evaporation of magnesium during the welding process, which has been shown to lead to the formation of porosities within the microstructure. Figure 3-3d shows the fracture strain behavior for AA5052. Unlike AA6061, the welded AA5052 material exhibits a significant increase in fracture strain at higher temperatures. As temperature rises, the fracture strain of the welded AA5052 material increases exponentially, approaching the values of the base material. This trend suggests that the welded AA5052 alloy retains and even improves its ductility at elevated temperatures, eventually displaying mechanical behavior similar to that of the base material.

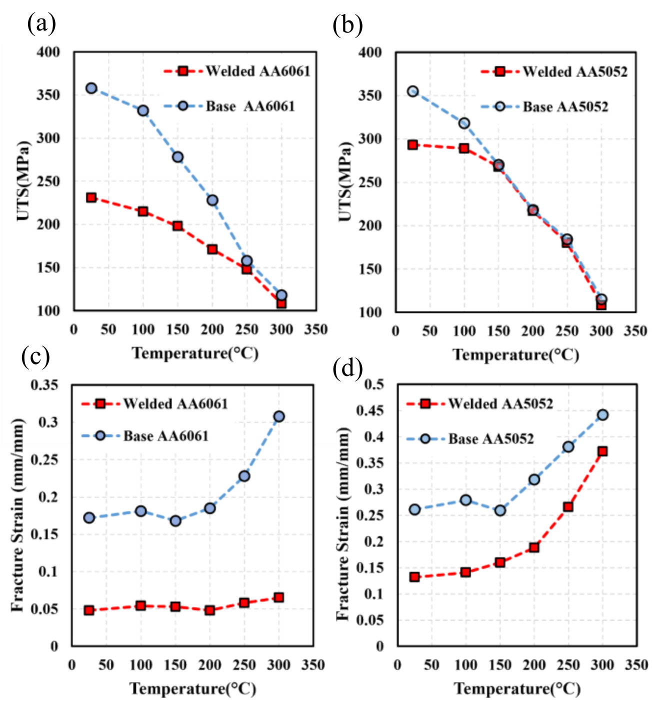

Figure 3-3. (a), (b) UTS, and (c), (d) fracture strain changes as a function of temperature and at a strain rate of 0.01 s^{-1}

3.2.5.2 Statistical analysis

In this study, a comprehensive statistical analysis was conducted to understand the influence of temperature and strain rate on the UTS and fracture strain of welded AA5052-H36 and AA6061-T6. Given the experimental observations that temperature exerts the most significant effect on mechanical properties, it was crucial to quantify the contribution of both temperature and strain rate to the variations in UTS and fracture strain. To achieve this, ANOVA was employed to determine the percentage contribution of each factor, providing a clear understanding of their relative impact. Additionally, regression models were developed to explore the relationship between temperature, strain rate, and mechanical properties. The nature of these relationships, whether linear, exponential, or otherwise, was characterized, and the effects of changes in temperature and strain rate on UTS and fracture strain were quantified using these models.

Table 3-1 presents the ANOVA results for AA6061-T6. The analysis reveals that temperature is the predominant factor influencing UTS, accounting for 95.09% of the variability, with a highly significant P-value of 0.000. This linear relationship between UTS and temperature suggests that the mechanical strength of AA6061-T6 is closely tied to microstructural changes, particularly the dissolution of strengthening precipitates as temperature increases. Strain rate, on the other hand, contributes a negligible 0.34% to UTS variability, indicating that UTS is largely unaffected by changes in strain rate. For fracture strain, temperature again plays a major role, contributing 65.16% to the variability, but with additional significant contributions from higher-order temperature terms (quadratic and cubic), which account for a combined 20.92% of the variability. This indicates a more complex, non-linear relationship between temperature and fracture strain, likely due to the sensitivity of fracture strain to microstructural defects and localized weaknesses in the material. The strain rate's impact on fracture strain is minor and not statistically significant.

Table 3-2 presents the ANOVA results for AA5052-H36. Similar to AA6061-T6, temperature is the most significant factor affecting UTS in AA5052-H36, contributing 87.04% of the variability, with a P-value of 0.000, indicating a strong linear relationship. However, the error term is slightly higher in this alloy, accounting for 12.95% of the variability, suggesting the presence of other influencing factors not captured in the model. For fracture strain, temperature is again the dominant factor, contributing 80.49% of the variability. However, unlike AA6061-T6, the strain rate in AA5052-H36 has a statistically significant, though small, effect on fracture strain, contributing 1.57% with a P-value of 0.029. The quadratic temperature term is also highly significant, contributing 16.15% to the variability, indicating a strong non-linear relationship between temperature and fracture strain in this alloy.

When comparing the ANOVA results for AA6061-T6 and AA5052-H36, several key differences emerge. While temperature is the dominant factor influencing UTS in both alloys, its impact is more pronounced in AA6061-T6, with a higher percentage contribution and lower error term, suggesting a more direct relationship. For fracture strain also, both alloys show significant non-linear relationships with temperature.

Table 3-1. ANOVA result for AA6061-T6

	Source	DF	Seq SS	Contribution	Adj SS	Adj MS	F-Value	P-Value
UTS	Regression	2	21336.7	95.42%	21336.7	10668.4	93.83	0.000
	T (°C)	1	21261.7	95.09%	21261.7	21261.7	187.01	0.000
	Strain rate (1/s)	1	75.0	0.34%	75.0	75.0	0.66	0.438
	Error	9	1023.3	4.58%	1023.3	113.7		
	Total	11	22360.0	100.00%				
fracture strain	Source	DF	Seq SS	Contribution	Adj SS	Adj MS	F-Value	P-Value
	Regression	4	0.000335	90.49%	0.000335	0.000084	16.65	0.001
	T (°C)	1	0.000241	65.16%	0.000037	0.000037	7.38	0.030
	Strain rate (1/s)	1	0.000016	4.42%	0.000016	0.000016	3.25	0.114
	T (°C)×T (°C)	1	0.000029	7.75%	0.000038	0.000038	7.53	0.029
	T (°C)×T (°C)×T(°C)	1	0.000049	13.17%	0.000049	0.000049	9.69	0.017
	Error	7	0.000035	9.51%	0.000035	0.000005		
	Total	11	0.000370	100.00%				

Table 3-2. ANOVA result for AA5052-H36

	Source	DF	Seq SS	Contribution	Adj SS	Adj MS	F-Value	P-Value
UTS	Regression	2	46636.4	87.05%	46636.4	23318.2	30.24	0.000
	T (°C)	1	46631.0	87.04%	46631.0	46631.0	60.48	0.000
	Strain rate (1/s)	1	5.3	0.01%	5.3	5.3	0.01	0.936
	Error	9	6939.3	12.95%	6939.3	771.0		
	Total	11	53575.7	100.00%				
fracture strain	Source	DF	Seq SS	Contribution	Adj SS	Adj MS	F-Value	P-Value
	Regression	3	0.074927	98.21%	0.074927	0.024976	146.58	0.000
	T (°C)	1	0.061402	80.49%	0.002072	0.002072	12.16	0.008
	Strain rate (1/s)	1	0.001200	1.57%	0.001200	0.001200	7.04	0.029
	T (°C)×T (°C)	1	0.012324	16.15%	0.012324	0.012324	72.33	0.000
	Error	8	0.001363	1.79%	0.001363	0.000170		
	Total	11	0.076290	100.00%				

The main effect plots presented in Figure 3-4 provide a comprehensive view of the impact of temperature and strain rate on the UTS and fracture strain of AA6061-T6 and AA5052-H36.

For AA6061-T6 (Figure 3-4a), the sharp decrease in UTS from approximately 250 MPa at 25℃ to about 125 MPa at 300℃ reflects the significant role of temperature as identified in the ANOVA analysis. The steep slope of the temperature effect curve underscores the high contribution of temperature to the variability in UTS, accounting for over 95% of the total variation, as highlighted in the ANOVA results. This statistical representation quantifies the impact of temperature, making it clear that the reduction in UTS is not just observable but statistically significant. The flat line representing strain rate, with UTS remaining around 170 MPa, confirms that strain rate contributes minimally to UTS, reinforcing its statistical insignificance in the model. For AA5052-H36 (Figure 3-4c), UTS decreases from approximately 350 MPa at 25℃ to around 250 MPa at 300℃. The less steep decline, compared to AA6061-T6, suggests a lower sensitivity to temperature, which is statistically validated by a lower contribution of temperature to the UTS variability in the ANOVA results. The near-horizontal line for strain rate indicates its negligible effect on UTS, statistically supporting the observation that strain rate does not significantly influence UTS in AA5052-H36.

For AA6061-T6 (Figure 3-4b), the fracture strain exhibits a complex, non-linear response to temperature. Initially, fracture strain decreases slightly as the temperature rises to around 150℃, but beyond this point, there is a significant increase, with fracture strain reaching approximately 0.065 mm/mm at 300℃. This non-linear trend reflects the material's transition from a more brittle to a more ductile failure mode as temperature increases. The ANOVA analysis supports this observation, revealing significant quadratic and cubic terms that statistically validate the temperature’s complex effect on fracture strain. The plot's curvature highlights the statistically significant non-linear relationship, which might not be as evident from initial tensile data alone. The slight negative impact of strain rate, with fracture strain decreasing from 0.053 mm/mm to 0.05 mm/mm as strain rate increases, is also confirmed by the ANOVA results, though its contribution is relatively minor compared to the overwhelming influence of temperature. In contrast, AA5052-H36 (Figure 3-4d) shows a robust, non-linear increase in fracture strain as temperature rises. The fracture strain increases markedly from approximately 0.12 mm/mm at lower temperatures to around 0.35 mm/mm at 300°C, indicating a significant enhancement in ductility with increasing thermal exposure. This strong non-linear behavior is statistically captured by the ANOVA model, where the quadratic term for temperature contributes significantly to the variability in fracture strain. This suggests that AA5052-H36 not only maintains but also improves its ductility at elevated temperatures, making it a more resilient option under thermal stress compared to AA6061-T6. The minimal impact of strain rate, with fracture strain slightly decreasing from 0.17 mm/mm to 0.1 mm/mm as strain rate increases, further emphasizes that temperature is the primary driver of ductility changes in AA5052-H36, a conclusion reinforced by the statistical insignificance of strain rate effects in the ANOVA results.

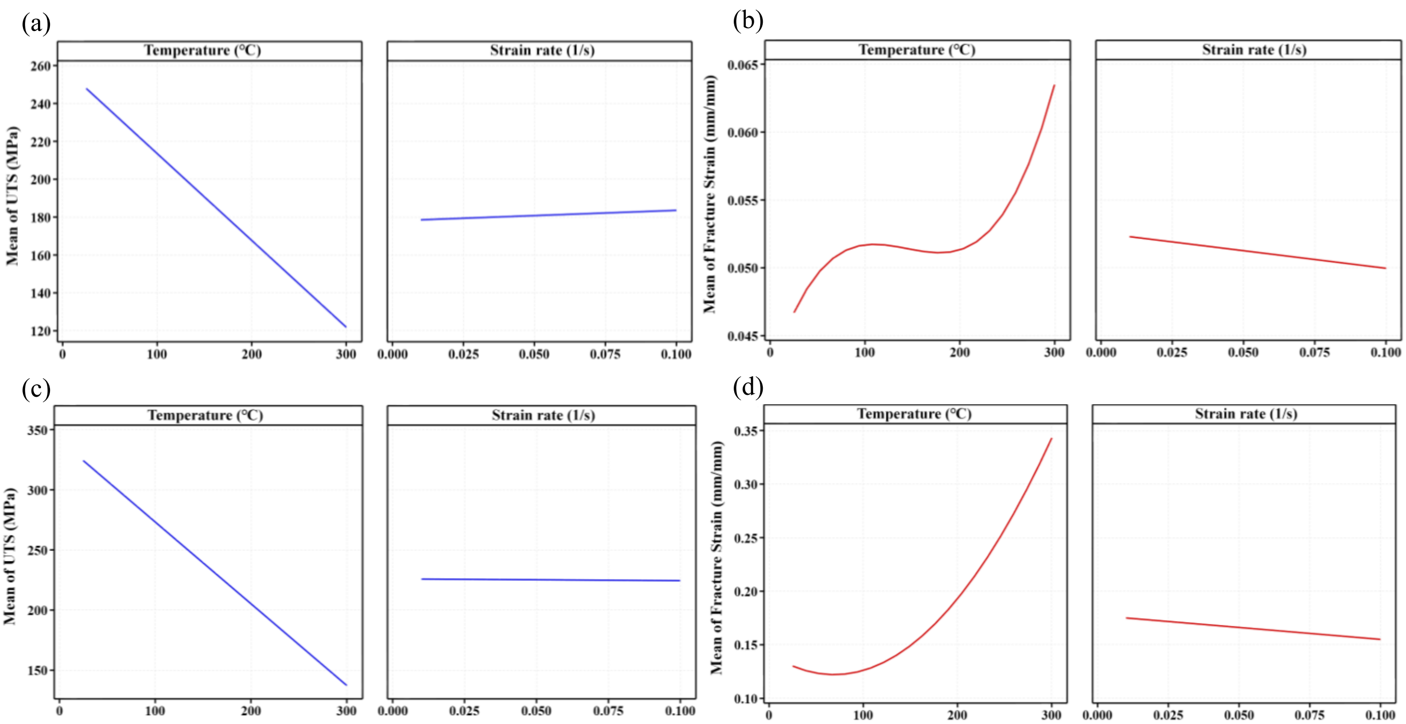

Figure 3-4. Main effect plots for (a) UTS of AA 6061-T6, (b) fracture strain of AA 6061-T6, (c) UTS of AA 5052-H36, and (d) fracture strain of AA 5052-H36

The non-linear behavior observed in the ANOVA analysis for AA5052-H36 and AA6061-T6 can be directly related to the differences in their microstructural evolution, as evidenced by the DSC curves. The ANOVA table for AA5052-H36, combined with DSC data from the literature [178], shows that this alloy does not undergo significant phase changes at the temperatures tested, primarily because AA5052-H36 is a non-heat-treatable alloy. The phases present in this material remain stable up to much higher temperatures, typically above 592°C [178], which is above the temperature in this study. In contrast, the higher sensitivity of AA6061-T6 to both quadratic and cubic temperature terms in the ANOVA results highlights the more complex and non-linear relationship between temperature and mechanical properties. This non-linear behavior is justified by the DSC curve of AA6061-T6, which shows distinct peaks corresponding to various precipitation phases. The DSC curve, shown in Figure 3-5, indicates that the first peak is related to the formation of Guinier-Preston (GP) zones, which contribute to the initial hardening of the material. As the temperature increases to around 206°C, the β'' phase begins to precipitate, which is the primary strengthening phase in AA6061-T6. The area under this peak suggests a significant volume fraction of β'' phase still left to form, explaining the initial retention of mechanical strength up to this temperature. As the temperature continues to rise to around 264°C, the β' phase starts to form, while the remaining β'' phase diminishes. This transition marks the beginning of the material's over-aging process, where the mechanical properties start to degrade more rapidly. Finally, at temperatures above 391°C, β' phase dissolute and the β phase becomes dominant, and the material undergoes significant grain coarsening and potential creep, leading to a further reduction in mechanical strength and ductility.

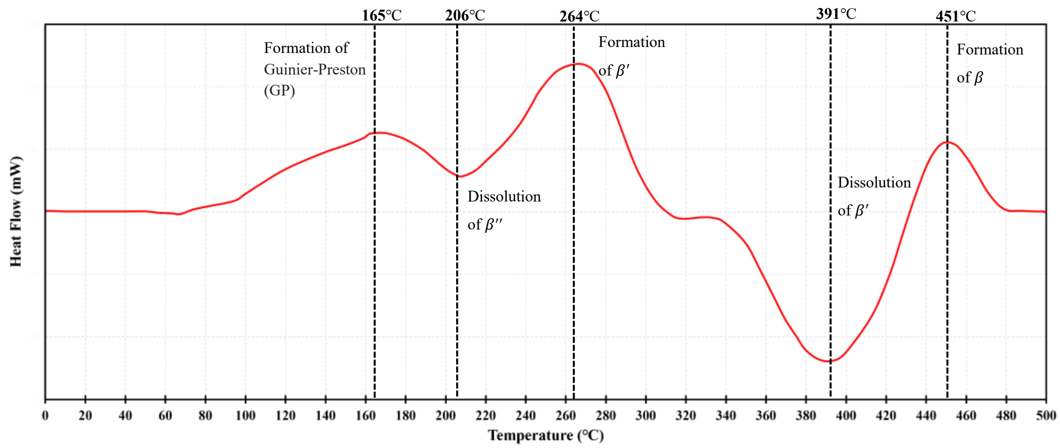

Figure 3-5. DSC thermal analysis of alloy AA 6061-T6 for heating

The tensile stress temperatures in this study are categorized in relation to significant phase transformation points, providing insight into the mechanical behavior of AA6061-T6 at each stage. From room temperature to 150°C, the material remains below the critical temperature of 165°C, where GP zones reach their peak formation. In this temperature range, the GP zones, which are small coherent precipitates, play a crucial role in strengthening the material by impeding dislocation movement, thereby enhancing hardness and tensile strength. However, because this range is below the dissolution temperature of the β'' phase (around 206°C), the primary strengthening mechanism remains intact, and the material exhibits robust mechanical properties. At 200°C, the temperature lies between the critical points of 165°C and 206°C, where the GP zones are fully formed and the β'' phase begins to dissolve. This temperature is critical as the dissolution of the β'' phase leads to a slight decrease in the material's strength, marking the onset of a transition from peak-aged to over-aged conditions. Despite this, the material retains a significant amount of its mechanical strength due to the presence of residual β'' phase and the fully formed GP zones. As the temperature increases to 250°C, the material falls between 206°C and 264°C, where the β'' phase continues to dissolve, and the β' phase starts to form. This transition from β'' to β' indicates the beginning of over-aging, characterized by a reduction in strength and hardness as the β' phase, which is less effective at blocking dislocations, becomes more prominent. The mechanical properties begin to degrade as the material shifts away from its peak strength condition. Finally, at 300°C, the temperature is between 264°C and 391°C, where the β' phase is fully formed and begins to dissolve, leading to the formation of the β phase. This range is associated with significant grain coarsening and the potential onset of creep, resulting in a marked decline in both strength and ductility. The dominance of the β phase, which is a less coherent precipitate, contributes to the further reduction of the material's mechanical properties, making it more susceptible to deformation under stress.

The regression models for UTS and fracture strain have been developed and are presented in Eq. 3-1 to Eq. 3-4.

$$UTS_{AA6061} = 256.31 - 0.4587 \times T + 55.6 \times SR \qquad \text{Eq. 3-1}$$

$$UTS_{AA5052} = 342 - 0.6793 \times T - 15 \times SR \qquad \text{Eq. 3-2}$$

$$Fracture\ Strain_{AA6061} = 0{,}04357888357138 + 0{,}00021996529436 \times T - 0{,}02592592592593 \times SR - 0{,}00000161971749 \times T \times T + 0{,}0000000037456 \times T \times T \times T \qquad \text{Eq. 3-3}$$

$$Fracture\ Strain_{AA5052} = 0{,}1539 - 0{,}000573 \times T - 0{,}2222\ \times SR +\ 0{,}000004 \times T \times T \qquad \text{Eq. 3-4}$$

Figure 3-6 shows the predicted values versus the actual values for UTS and fracture strain. Figure 3-6a displays the predicted versus actual values for UTS for both alloys, while Figure 3-6b presents the corresponding plot for fracture strain. The diagrams indicate a very high correlation between the actual and predicted values, demonstrating the precision of the regression model. The error line reflects a low level of errors, consistently less than 10%, in alignment with the ANOVA calculations. These accurate regression models were subsequently used for the extraction of the contour plots.

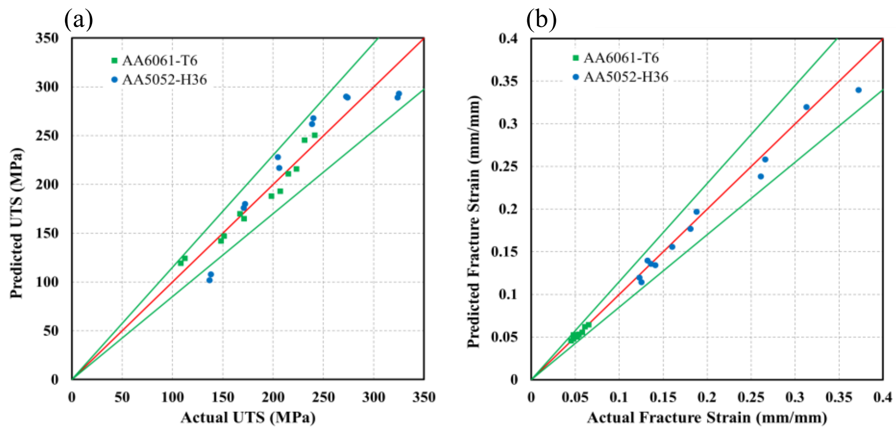

Figure 3-6. Predicted versus actual values for (a) UTS and (b) fracture strain of AA 6061-T6 and AA 5052-H36

While the regression models used to predict ultimate tensile strength UTS and fracture strain provide a good fit within the tested temperature and strain rate conditions, it is important to discuss their limitations, particularly with respect to extrapolation beyond the tested conditions. These models are based on the assumption that the relationship between the input variables (temperature, strain rate) and the output properties (UTS, fracture strain) is consistent across the tested range. However, this assumption may not hold true when applying the models to conditions outside of the experimental data range. Extrapolation beyond the tested conditions can lead to inaccuracies, as the relationship captured by the model may not reflect the material's true behavior under different conditions. The tested conditions in this study were limited to a specific temperature range (25°C to 300°C) and strain rates (0.01 s^{-1} and 0.1 s^{-1}), so predictions outside of these conditions should be made with caution. Additionally, the model assumes that the relationship between temperature, strain rate, and mechanical properties is linear. While this assumption holds within the tested ranges, it may not be valid if applied to a broader range of conditions. Non-linear behaviors, interactions between variables, or phase changes at different temperatures could affect the accuracy of predictions made using this model. There are also potential sources of error, such as measurement uncertainties and overfitting. Measurement uncertainties in the experimental data, including temperature and strain rate variations, can introduce minor errors in the model predictions. Overfitting, where the model captures noise or random fluctuations in the data rather than generalizable trends, can lead to less accurate predictions when the model is applied outside the tested conditions.

Figure 3-7a- Figure 3-7d present the contour plots extracted from the predicted model discussed in the previous sections. The unique advantage of these contour plots lies in their ability to elucidate the relationships between temperature, strain rate, and fracture strain. Figure 3-7a shows the relationship between UTS and temperature, clearly illustrating the consistent linear decrease in UTS with increasing temperature across all strain rates; a relationship that has been thoroughly discussed in the previous sections. Figure 3-7b illustrates the fracture strain of AA6061-T6 as a function of temperature and strain rate. The contour lines on the plot provide detailed insights into the relationships between strain rate, temperature, and fracture strain. When examining fracture strains below 0.048 mm/mm, the relationship between temperature, strain rate, and fracture strain appears linear, with temperature having a gradual, predictable effect on fracture strain. Similarly, at fracture strains above 0.054 mm/mm, the relationship once again becomes linear, but with a more pronounced influence of temperature on fracture strain. However, within the range between these two fracture strain values, specifically around 0.051 mm/mm, the relationship becomes notably complex. Here, the contour lines are curved, indicating that fracture strain is highly sensitive to both temperature and strain rate, unlike the linear behavior observed outside this range. This sensitivity suggests that within this range, small variations in temperature and strain rate can lead to significant and non-linear changes in fracture strain. This behavior is likely connected to the material transitions observed in the DSC curve, indicating that phase changes occurring within this temperature range contribute to the complexity of the relationship between fracture strain, temperature, and strain rate. The alignment of this complex relationship with the thermal transitions observed in the DSC analysis reinforces the model's accuracy in capturing the intricate effects of these factors on the material's fracture behavior. Similarly, the contour plots for AA5052-H36, shown in Figure 3-7c and 7d, reveal patterns akin to those observed for AA6061-T6. In Figure 3-7c, the linear relationship between UTS and temperature is evident across different strain rates, confirming the predictable decrease in UTS with increasing temperature. Figure 7d focuses on fracture strain, showing that for values below 0.15 mm/mm, the relationship between strain rate, temperature, and fracture strain is non-linear, as indicated by the curved contour lines. However, above 0.15 mm/mm, the contour lines become linear, suggesting that temperature and strain rate have a more straightforward and predictable influence on fracture strain in this range.

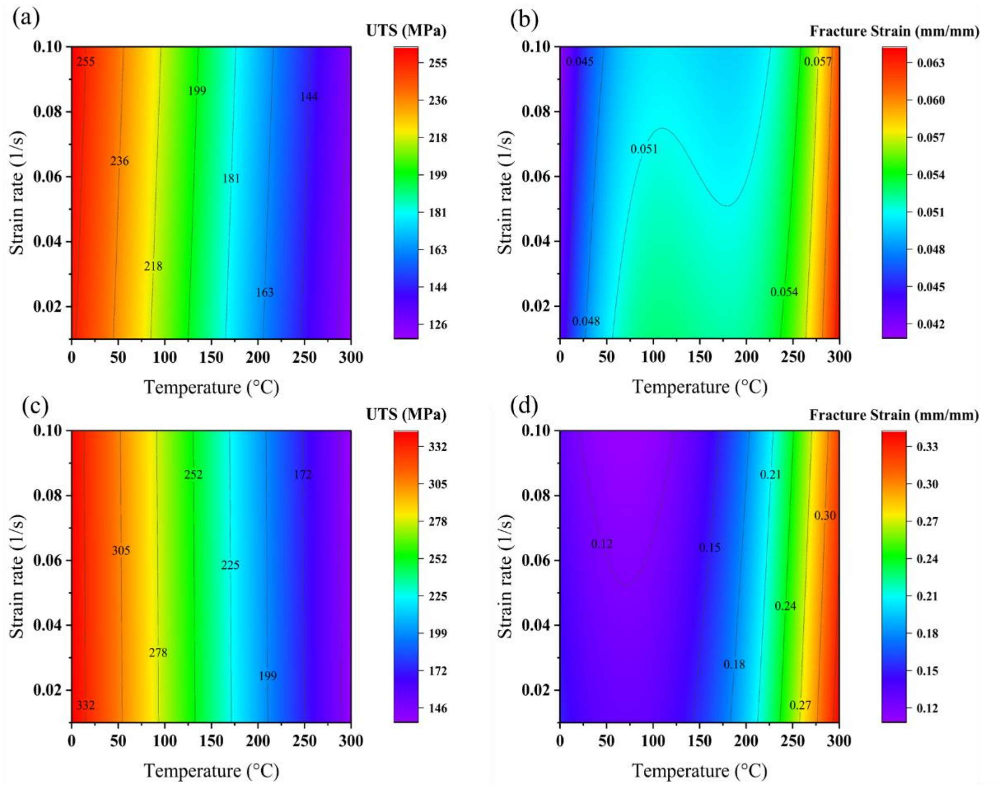

Figure 3-7. Contour plots of regression model: (a) UTS of AA 6061-T6, (b) fracture strain of AA 6061-T6, (c) UTS of AA 5052-H36, and (d) fracture strain of AA 5052-H36

3.2.5.3 Microstructure and Fractography

Figure 3-8 illustrates the fractography and microstructure of the welded AA6061-T6 at room temperature and 300°C. Figure 3-8a shows the macrostructure of the welded material. At room temperature the fracture occurs in the HAZ, which is commonly reported in the literature as the weakened part of the aluminum laser welded materials due to the residual stresses, grain growth, and the potential for defects like porosity and cracking [179,180].

When the temperature is increased to 300°C, the fracture location shifts from the HAZ to the FZ. This shift could be attributed to the changes in material properties and microstructural evolution with increasing temperature. Figure 3-8b depicts the microstructure of the material after fracture in the welded area. The microstructure of the HAZ at both room temperature and 300°C shows similar features, revealing an increase in oriented elongated grains in the welded area, aligning towards the heat flux direction, indicating significant thermal influence during welding.

Figure 3-8c and d show the fracture surfaces at room temperature. At low magnification (Figure 3-8c), the fracture surface exhibits a relatively flat and brittle fracture with shear lips at the edges. The SEM image in Figure 3-8d shows that the welded AA6061-T6 alloy at room temperature exhibits a complex fracture surface with both brittle and ductile features. The cleavage facets represent regions of brittle fracture where the material failed along specific crystallographic planes. In contrast, the microvoid coalescence and dimple formation indicate areas where the material underwent plastic deformation, leading to more ductile features of fracture. The coexistence of these fracture modes suggests that the material's response to tensile loading at room temperature involves both brittle and ductile mechanisms. This mixed-mode fracture behavior is significant because it indicates that while the material can absorb some energy through plastic deformation, it is also prone to abrupt brittle failure.

With an increase in temperature to 300°C, the fracture surface characteristics change significantly. Figure 3-8e (low magnification) at high temperature shows a more ductile fracture pattern, with two distinct fracture types. flat surfaces with cleavage facets indicating abrupt fractures and areas with severe plastic deformation alongside improved coarsening. The SEM image in Figure 3-8e demonstrates that the welded AA6061-T6 alloy at 300°C predominantly shows ductile fracture (compared to brittle fractures features) with significant plastic deformation. The presence of large dimples and coalesced microvoids indicates that the material absorbed considerable energy during deformation, resulting in a more ductile fracture mode. The mixed fracture modes, with some cleavage facets and shear lips, suggest that while ductile mechanisms dominate, brittle components are still present, albeit less pronounced than at lower temperatures. The thermal influence at 300°C enhances the material's ductility, allowing for more extensive plastic deformation before failure. This change in fracture behavior from brittle at room temperature to more ductile at elevated temperatures is crucial for understanding the material's performance in high-temperature applications. Figure 3-8f (high magnification) reveals very soft fracture features, including fine dimples and shear lines, indicative of severe plastic deformation and enhanced ductility at elevated temperatures.

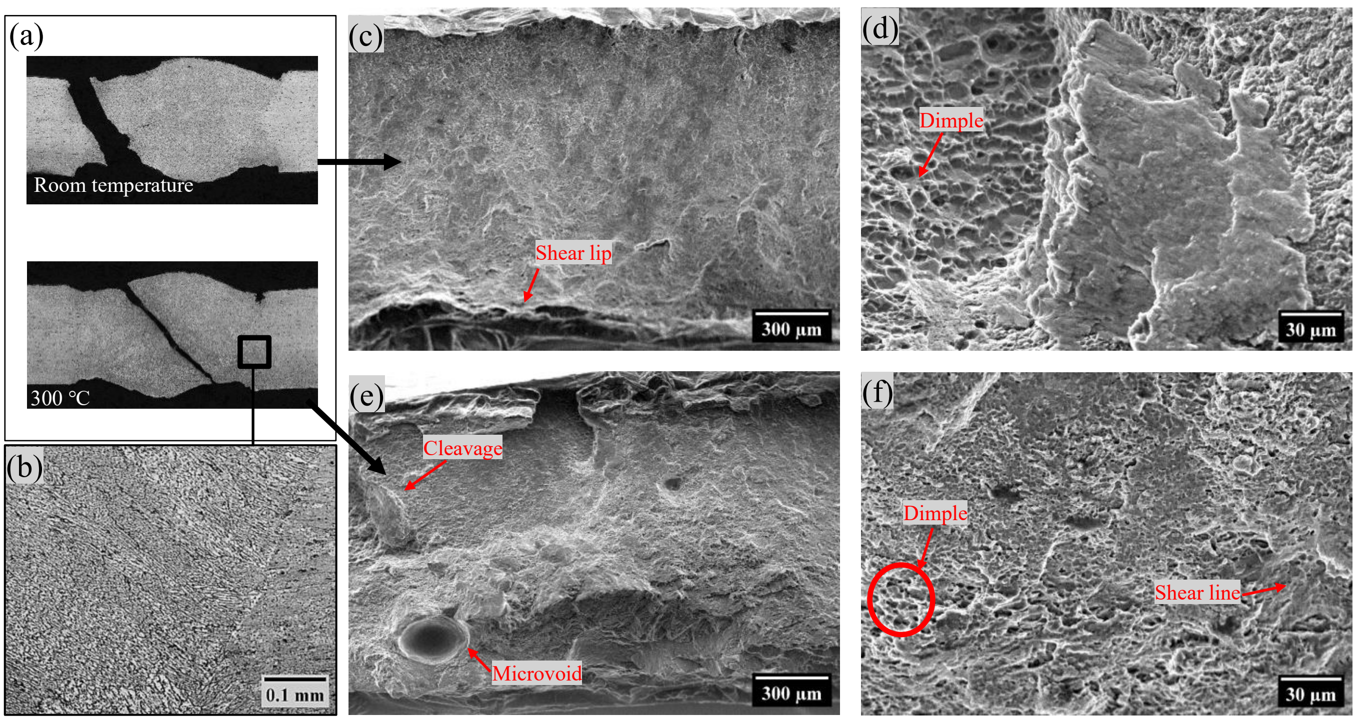

Figure 3-8. Optical microscopy image of AA6061-T6 (a) macrostructure, (b) microstructure, and SEM fractographic image at (c) low magnification at room temperature, (d) high magnification at room temperature, (e) low magnification at 300°C, (f) high magnification at 300°C

Figure 3-9 illustrates the fractography and microstructure of the welded AA5052-H36 at room temperature and 300°C. The observed features are like those of AA6061-T6, with some distinct differences. Figure 3-9a shows the macrostructure of the welded material after fracture at room temperature and 300°C. Unlike AA6061-T6, the fracture for AA5052-H36 occurs consistently at HAZ. The microstructure in Figure 3-9b reveals finer grains in the welded area compared to the base material, indicating significant grain refinement due to the welding process. Figure 3-9c and d show the low and high magnification images of the fractured surface at room temperature. The SEM image in Figure 3-9c demonstrates that the welded AA5052-H36 alloy at room temperature predominantly undergoes ductile fracture with significant plastic deformation. The presence of extensive dimples and microvoid coalescence indicates that the material can absorb considerable energy before fracturing, which is a hallmark of ductile behavior. The porous coarsening regions further support the observation of significant plastic deformation. The mixed-mode fracture features, with both ductile dimples and flat, cleavage-like regions, suggest a complex fracture mechanism where the material initially deforms plastically but also experiences brittle failure in certain areas. This combination of fracture modes indicates that while the material is generally ductile (with slight brittle fracture features), there are localized regions where brittleness can occur, potentially due to microstructural heterogeneities or stress concentrators. The microstructural stability observed in the fracture surface implies that the welding process has not significantly compromised the material's integrity. The finer grain structures in the welded area help maintain the material's ductility and toughness, making AA5052-H36 a suitable candidate for applications requiring both high strength and ductility at ambient temperatures. The SEM image in Figure 3-9d shows that the welded AA5052-H36 alloy at room temperature exhibits a highly ductile fracture mode. The fine dimple structure and coarse, porous areas indicate that the material absorbed considerable energy during deformation. The presence of shear lips further supports the observation of ductile shear failure. The SEM images in Figure 3-9e and f demonstrate that the welded AA5052-H36 alloy at 300℃ exhibits a predominantly ductile fracture mode (in the mixed mode fracture). The low magnification image (Figure 3-9e) highlights porous coarsening and cleavage facets, indicating a mixed-mode fracture with both ductile and brittle features. The high magnification image (Figure 3-9f) reveals a fine dimpled structure and shear lips, confirming the material's enhanced ductility at elevated temperatures.

The comparison between the AA5052-H36 and AA6061-T6 alloys shows that, for AA5052-H36, the fracture consistently occurs in the HAZ and the welded area exhibits finer grain structures. Additionally, the ductile fracture features at both room temperature and 300°C indicate that AA5052-H36 maintains its ductility under varying thermal conditions, making it a robust candidate for applications requiring thermal and mechanical resilience.

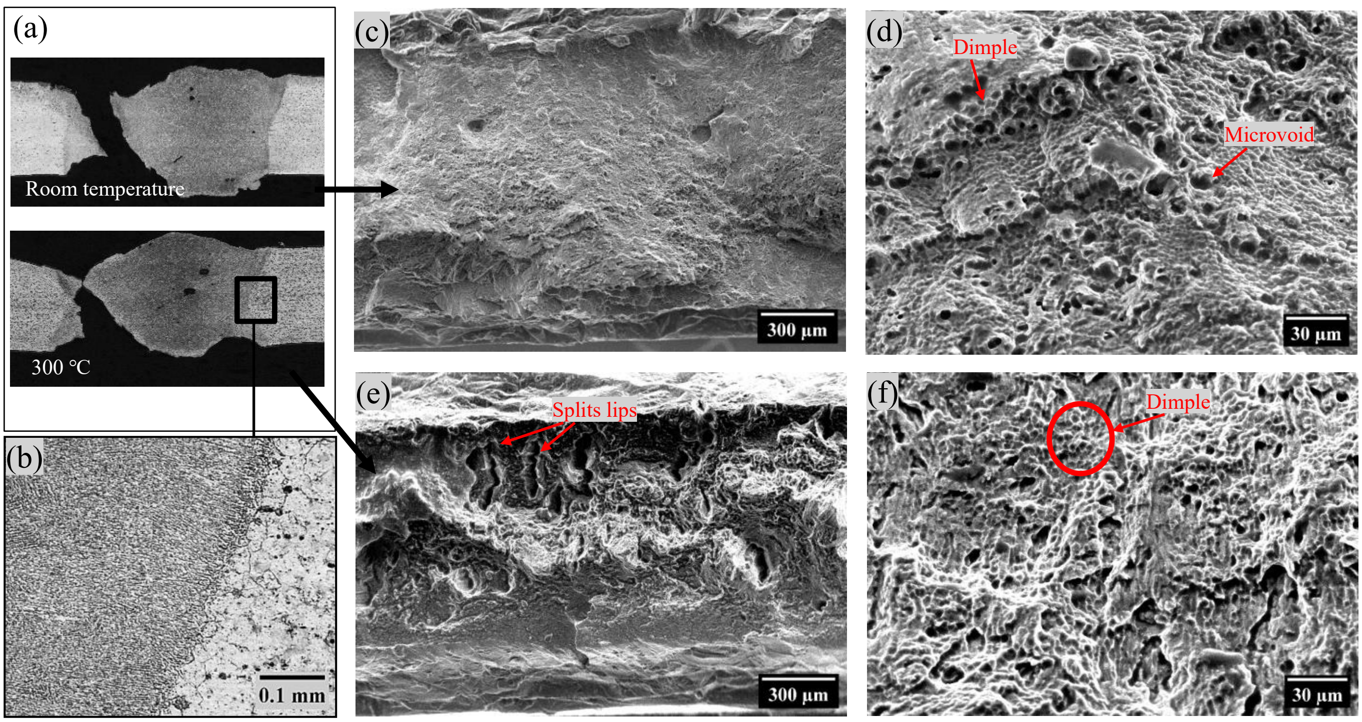

Figure 3-9. Optical microscopy image of AA5052-H36 (a) macrostructure, (b) microstructure, and SEM fractographic image at (c) low magnification at room temperature, (d) high magnification at room temperature, (e) low magnification at 300°C, (f) high magnification at 300°C

Figure 3-10 compares the energy absorption behavior of two welded aluminum alloys. The graph clearly indicates that AA5052-H36 demonstrates superior energy absorption capabilities, ranging from approximately 9 to 13 J at 0.01 s^{-1} and 7 to 11 J at 0.1 s^{-1}. In contrast, AA6061-T6 shows significantly lower energy absorption, approximately 2.5 to 3 J across the tested strain rates, which is roughly 3 to 4 times less than that of AA5052-H36. The higher energy absorption in AA5052-H36 is evident in the fracture surface analysis (Figure 3-9d), where the material at room temperature exhibits large, deep dimples averaging around 12 µm in size. These deep dimples are indicative of significant plastic deformation and contribute to higher energy absorption by dissipating the applied strain over a larger area. Conversely, in AA6061-T6, as seen in Figure 3-8d, the fracture surface at room temperature shows a mix of smaller dimples and flat, shiny areas (indicative of clustered shear). The smaller dimples and flat areas in AA6061-T6 suggest a less efficient energy absorption mechanism, where localized deformation occurs without extensive plastic flow, leading to lower overall energy dissipation.

Both materials exhibit peaks in energy absorption at specific temperatures AA5052-H36 at 250°C and AA6061-T6 at both 100°C and 250°C. For AA6061-T6, the initial peak at 100°C is followed by a reduction in energy absorption due to the dissolution of β'' zones, which are essential for maintaining the alloy's strength. As the temperature increases to 250°C, a second peak in energy absorption is observed, likely due to the temporary stabilization provided by the formation of β' precipitates. However, at temperatures of 250°C and above, creep-induced dissolution occurs, leading to a significant decrease in energy absorption. This behavior is mirrored in AA5052-H36, where the energy absorption peaks at 250°C before dropping sharply. The sharp decline in energy absorption beyond 250°C in both materials is indicative of the onset of creep [181], a deformation mechanism that becomes significant at high temperatures. The fracture features observed in the corresponding fracture surfaces at 300°C (Figure 3-8f and Figure 3-9f) provide further insight into this behavior. In AA6061-T6, the fracture surface at 300°C (Figure 3-8f) reveals a mixture of ductile and brittle fracture modes. The presence of elongated dimples and cleavage facets suggests that while the material exhibits some degree of plastic deformation, it also undergoes abrupt, brittle fracture due to the loss of mechanical integrity as the β phases begin to dissolve. The elongated dimples observed at 300°C in AA6061-T6 reflect the local plasticity, while the cleavage facets indicate the transition to brittle fracture as creep effects dominate. The onset of creep is further evidenced by the presence of intergranular fracture patterns, where the grain boundaries have weakened, leading to a reduction in the material's ability to absorb energy before fracture. In AA5052-H36 (Figure 3-9f), the fracture surface at 300°C also shows signs of creep, with the presence of coarse, elongated dimples. The material's ability to absorb energy is initially high at 250°C due to the balance between thermal softening and the material's inherent resistance to deformation. However, as the temperature rises further, the fracture surface begins to exhibit features typical of creep-induced failure, such as intergranular cracks and void coalescence, which lead to a rapid decrease in energy absorption. The coarse, elongated dimples in AA5052-H36 at 300°C suggest that the material is experiencing a high degree of localized plastic deformation before creep-induced failure mechanisms take over. Overall, AA5052-H36 outperforms AA6061-T6 at elevated temperatures, particularly in terms of energy absorption and ductility. However, temperatures above 250°C should be avoided in hot forming processes for both alloys due to the onset of creep, which significantly reduces mechanical integrity and leads to a sharp decline in energy absorption, increasing the risk of failure.

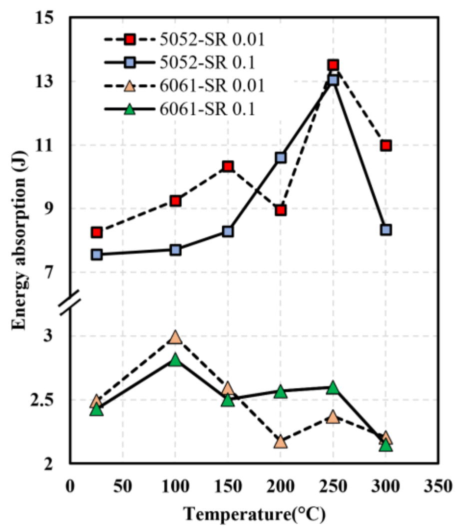

Figure 3-10. Energy absorbed before fracture in AA 5052-H36
and AA 6061-T6 at different strain rates and temperatures

3.2.5.4 Microhardness

Figure 3-11 shows the microhardness profile of the welded materials. The microhardness of the base material is calculated at a single point and shown as a reference with the dashed line.

For the welded AA6061-T6, the microhardness profile shows a notable reduction compared to the base material. Specifically, the microhardness of the base AA6061-T6 is 85 HV, whereas the microhardness in the welded area drops to 68 HV, representing a reduction of approximately 20%. This reduction is primarily attributed to magnesium evaporation in the weld zone, a phenomenon extensively reported in the literature and corroborated by the authors' previous work [182–186]. The loss of magnesium leads to a decrease in the volume fraction of Mg_2Si precipitates, which are crucial for the precipitation hardening of AA6061-T6. Additionally, grain coarsening during welding further contributes to the decrease in hardness which could be observed in Figure 3-8c.

In contrast, AA5052-H36, a non-heat-treatable alloy, does not rely on precipitation hardening for its strength. The microhardness profile of the welded AA5052-H36 shows an increase in microhardness value in FZ up to 102 HV, compared to 90 HV for the base material, which represents approximately a 13% increase. The observed increase in microhardness can be attributed to grain size reduction, as seen in Figure 3-9b. The finer grain structure in the welded area enhances the material's hardness through the Hall-Petch effect, where smaller grains result in higher strength [187]. However, the increase in microhardness is not consistent across the weld. In the HAZ, there is a noticeable reduction in hardness. This localized decrease is likely due to thermal effects that partially soften the material. Conversely, in the middle of the weld, the microhardness reaches values comparable to the base material, indicating effective grain refinement and retention of mechanical properties.

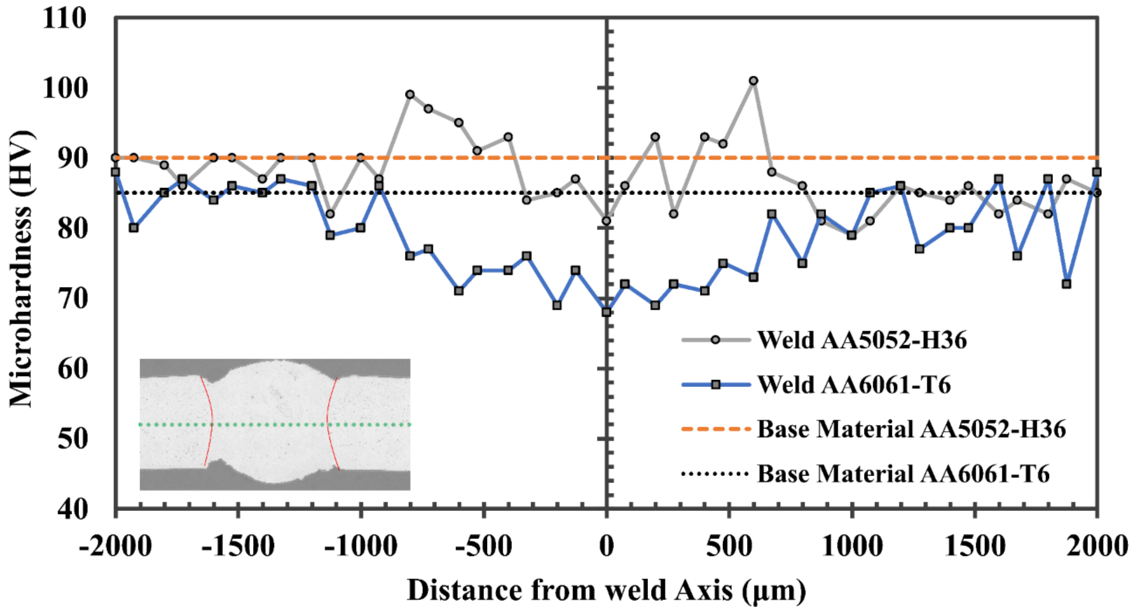

Figure 3-11. Microhardness profile of the welded materials

3.2.6 Conclusion

This study analyzed the mechanical properties of AA5052-H36 and AA6061-T6 aluminum alloys, which are widely used in the automotive industry, under high-temperature tensile tests to evaluate their behavior and compare them to their respective base materials. The mechanical properties of AA5052-H36 demonstrated superior UTS, fracture strain and absorbed energy before fracture compared to AA6061-T6.

The effects of strain rate on the mechanical properties were found to be minimal, with variations remaining within the error range of the testing. In contrast, temperature was observed to have a significant influence on material behavior, highlighting its importance as the primary factor in industrial applications. Therefore, temperature is considered the key parameter, with strain rate variations not being of major concern.

Under high-temperature tensile testing, ranging from 150°C to 300°C, AA5052-H36 consistently exhibited similar UTS and elongation to those of the base material. The UTS for both the base and welded material decreased to around 108 MPa, and the elongation increased to 0.37 mm/mm at 300°C. Conversely, AA6061-T6 exhibited lower UTS and elongation at lower temperatures, ranging from 25°C to 150°C, compared to the base material. As the temperature increased to 250-300°C, the UTS of AA6061-T6 approached that of the base material. However, the elongation remained significantly lower, around 0.07 mm/mm, compared to 0.32 mm/mm for the base material.

The microhardness profile further elucidated the differences between the two alloys. For AA5052-H36, the microhardness increased by around 13% in the FZ, suggesting enhanced grain refinement and stability post-welding. In contrast, AA6061-T6 showed a reduction in microhardness around 20%, primarily due to magnesium evaporation and the consequent reduction in precipitation hardening, which is crucial for its strength. This reduction in microhardness correlated with the observed decrease in mechanical performance at higher temperatures.

Fracture analysis revealed that both materials exhibited more ductile fracture characteristics, especially at temperatures above 250°C, where there was a significant reduction in energy absorption. This was accompanied by evidence of creep-induced fracture, indicating that temperatures above 250°C should be avoided in high-temperature tensile tests.

While the regression models provide valuable insights within the tested temperature and strain rate ranges, their applicability outside these conditions is limited. Future studies may explore a wider range of conditions or incorporate more complex models to account for non-linearities and variable interactions that might be present under different testing scenarios.

In summary, for high-temperature applications and forming processes, AA5052-H36 demonstrates better mechanical properties compared to AA6061-T6. The consistent performance of AA5052-H36 under thermal and mechanical stress, reflected in both its tensile behavior and microhardness profile, makes it a more reliable choice for high-temperature and welding-intensive applications. These findings provide essential insights for selecting suitable materials in the automotive industry, ensuring better performance and durability under demanding conditions.

CONCLUSION GÉNÉRALE

Le travail de recherche présenté dans cette étude a porté sur l'optimisation des procédés de soudage au laser et l'analyse des performances mécaniques des alliages d'aluminium AA5052 et AA6061 dans des conditions spécifiques, en vue d'applications industrielles exigeantes. Cette recherche s'est structurée en trois phases complémentaires. La première phase a consisté en une optimisation expérimentale des paramètres de soudage pour des feuilles en alliage AA5052-H32 de différentes épaisseurs, visant à réduire les défauts tels que l'entaillage et la porosité, tout en maximisant les performances mécaniques. La deuxième phase a exploré le comportement de fracture des joints soudés au laser sur l'alliage AA6061-T6 sous des températures élevées et des vitesses de déformation variables, offrant des perspectives sur l'influence des cycles thermiques et des contraintes résiduelles. Enfin, la troisième phase a comparé les propriétés en traction à haute température des alliages AA5052-H36 et AA6061-T6 soudés au laser, mettant en lumière les avantages spécifiques de l'AA5052-H36 dans des conditions thermiques critiques pour le secteur automobile. Ces résultats permettent de mieux appréhender les interactions complexes entre les paramètres de soudage, les propriétés des matériaux et les contraintes opérationnelles, fournissant ainsi des orientations précises pour l'amélioration des procédés industriels.

La première phase de cette étude a systématiquement examiné les principaux paramètres impliqués dans le soudage au laser en superposition des feuilles d'alliage d'aluminium AA5052-H32 de différentes épaisseurs, en se concentrant sur l'optimisation de la qualité de la soudure et des performances mécaniques. Les résultats montrent que les paramètres sélectionnés, y compris la puissance du laser, la vitesse de déplacement, la position de focalisation, l'amplitude d'oscillation et le motif d'oscillation, influencent de manière significative l'efficacité de la soudure, la formation d'entaillage et les niveaux de porosité. Les résultats indiquent que le motif d'oscillation a une influence minimale sur la résistance mécanique de la soudure, tous les motifs produisant des ratios R similaires. Cependant, l'amplitude d'oscillation joue un rôle crucial dans le contrôle de l'entaillage, une amplitude minimale de 1,5 mm étant requise pour réduire les valeurs d'entaillage à moins de 0,25 mm. Les paramètres optimisés pour obtenir des soudures de haute qualité ont été déterminés comme étant une puissance de laser de 2500 W, une vitesse de déplacement de 5 m/min, une position de focalisation de 6 mm et une amplitude d'oscillation de 1,5 mm. Ces conditions ont permis d'atteindre une efficacité de soudure supérieure à 99%, assurant des joints solides et sans défaut. La plage d'intensité de puissance de 13,2 à 20 J/mm² a été identifiée comme optimale pour maintenir une efficacité de soudure au-dessus de 90%. Les intensités de puissance inférieures à 13,2 J/mm² ont entraîné une efficacité de soudure considérablement réduite, tombant à 20% dans certains cas. Le sur-soudage, caractérisé par une pénétration excessive de la soudure et des défauts, s'est produit lorsque l'intensité de puissance a dépassé 23,6 J/mm². Le profilage de la microdureté s'est révélé être un outil précieux pour détecter les défauts cachés, tels que la porosité sous-jacente et la distorsion due à un apport thermique excessif. Les joints de soudure avec des intensités de puissance plus élevées, spécifiquement dans la plage de 13,2 à 20 J/mm², ont montré une distribution uniforme de la microdureté et une porosité minimale, validant ainsi l'efficacité des paramètres sélectionnés. Dans l'ensemble, cette recherche a réussi à optimiser les paramètres de soudage pour le soudage au laser en superposition des feuilles d'alliage d'aluminium AA5052-H32 de différentes épaisseurs. Les résultats fournissent des informations précieuses pour les applications industrielles, en particulier dans la fabrication automobile, où une haute efficacité de soudure et des défauts minimaux sont cruciaux. Les recherches futures se concentreront sur le perfectionnement de ces paramètres pour des facteurs de performance supplémentaires, tels que les propriétés à haute température et la durabilité mécanique à long terme.

La deuxième phase de cette étude a fourni une analyse approfondie du comportement de fracture des soudures en double face d'alliage d'aluminium 6061-T6, sous différentes températures et taux de déformation. Les résultats montrent qu'à mesure que la température augmente, la résistance mécanique du matériau, y compris la résistance à la traction ultime et la contrainte d'écoulement, diminue en raison du ramollissement thermique, tandis que sa ductilité, caractérisée par la déformation et l'absorption d'énergie, s'améliore. Plus précisément, l'étude a identifié une transition claire du comportement de fracture fragile à ductile lorsque la température dépassait 150°C, le matériau montrant une augmentation de la déformation plastique avant la rupture. Ce changement est attribué aux modifications microstructurales, en particulier la formation de microfissures dans la zone affectée par la chaleur centrale, où les contraintes résiduelles provenant du processus de soudage jouent un rôle significatif dans l'initiation et la propagation des fissures. L'analyse microstructurale a révélé une HAZ en forme de H avec des grains recristallisés dans la zone centrale, qui sont devenus des sites d'initiation de fissures à des températures élevées. À des températures plus basses, l'initiation des fissures était plus sensible aux défauts géométriques dans la ZAC, tandis qu'à des températures plus élevées, les fissures provenaient principalement des défauts microstructuraux au sein de la zone de fusion. Ces résultats soulignent l'impact critique des contraintes résiduelles induites par le soudage et des cycles thermiques sur le comportement de fracture des joints soudés. De plus, les essais de traction ont montré que les propriétés mécaniques des soudures, y compris la résistance à la traction ultime, la contrainte d'écoulement et la déformation, étaient très sensibles aux variations de température, mais moins influencées par les variations de taux de déformation dans la gamme testée. Cela suggère que, bien que des températures élevées favorisent une plus grande plasticité, la performance mécanique globale des soudures reste robuste sous diverses conditions de chargement. L'analyse de la microdureté a également montré une chute significative de la dureté dans la ZAC, en particulier dans les zones affectées par le deuxième passage du laser, où le matériau a subi des régions adoucies en raison de la transformation des phases de renforcement. Dans l'ensemble, cette phase fournit des informations précieuses sur la mécanique de fracture des soudures en double face d'aluminium 6061-T6, soulignant l'importance de contrôler la température et de comprendre l'évolution microstructurale pendant le soudage. Les résultats ont des implications significatives pour l'optimisation des processus de soudage afin d'améliorer la performance et la fiabilité des soudures en aluminium dans des applications critiques telles que les industries automobile et aérospatiale.

Les études futures sont recommandées pour explorer les effets d'autres configurations de soudage et combinaisons de matériaux, ainsi que la durabilité à long terme sous des charges cycliques et des conditions environnementales, afin de peaufiner davantage les modèles prédictifs pour le soudage de l'aluminium.

La troisième phase de cette étude présente une analyse comparative détaillée des propriétés de traction à haute température des alliages d'aluminium AA5052-H36 et AA6061-T6 soudés au laser, en se concentrant sur leur performance dans les applications automobiles. Les essais de traction ont révélé que l'AA5052-H36 surpassait constamment l'AA6061-T6 en termes de résistance à la traction ultime et de déformation de rupture à des températures élevées. Par exemple, la déformation de rupture de l'AA5052-H36 à 300°C était de 0,37 mm/mm, significativement plus élevée que les 0,07 mm/mm observés pour l'AA6061-T6, ce qui indique une ductilité supérieure de l'AA5052-H36. L'analyse microstructurale a révélé que l'AA5052-H36 conservait une structure de grain plus stable sous stress thermique, avec moins d'affinement des grains et moins de transformations de phases, tandis que l'AA6061-T6 subissait la dissolution des phases de renforcement β'' et la formation des phases β', ce qui contribuait à la dégradation du matériau. L'analyse de l'absorption d'énergie a également soutenu la supériorité de l'AA5052-H36, avec une absorption d'énergie atteignant 13,3 J à 250°C, contre environ 3 J pour l'AA6061-T6 à la même température. L'analyse statistique utilisant l'ANOVA a confirmé que la température était le facteur dominant affectant les propriétés mécaniques des deux alliages, avec la température contribuant à 95,09% de la variation de la RTA pour l'AA6061-T6 et 87,04% pour l'AA5052-H36. Le taux de déformation avait un impact négligeable sur la RTA et la déformation de rupture dans les deux alliages, sa contribution étant inférieure à 1%. Dans l'ensemble, l'AA5052-H36 a présenté des performances supérieures à haute température, ce qui en fait le matériau le plus adapté pour les applications automobiles exposées à des températures élevées, telles que les composants de moteur et les systèmes d'échappement. Ces résultats soulignent l'importance de la sélection des matériaux en fonction des exigences thermiques et mécaniques spécifiques de l'application, l'AA5052-H36 étant un choix plus fiable pour maintenir l'intégrité structurelle sous stress thermique par rapport à l'AA6061-T6.

Pour faire progresser la compréhension et l'optimisation du soudage au laser des alliages d'aluminium, les recherches futures pourraient se concentrer sur la réalisation de répétitions expérimentales supplémentaires et de tests de validation au-delà des paramètres explorés dans cette étude. Cela aiderait à renforcer et confirmer les modèles prédictifs développés pour la performance du soudage. De plus, l'intégration de techniques d'intelligence artificielle, telles que les réseaux neuronaux et les algorithmes d'apprentissage automatique, pourrait être précieuse pour prédire et optimiser les paramètres de soudage et les propriétés mécaniques. Cette approche pourrait permettre un contrôle plus précis de la qualité du soudage et de la résistance mécanique. En outre, il est essentiel d'explorer d'autres paramètres de performance critiques tels que la résistance à la corrosion, la résistance à la fatigue et la durabilité à long terme, qui sont cruciaux pour les applications automobiles et aérospatiales, mais n'ont pas été examinés de manière approfondie dans ce contexte. En élargissant le champ d'études pour inclure ces propriétés, les recherches futures pourraient fournir une compréhension plus complète de la performance et de la fiabilité des alliages d'aluminium soudés au laser dans les applications industrielles avancées.

RÉFÉRENCES BIBLIOGRAPHIQUES

1. Sheng ZQ. Formability of tailor-welded strips and progressive forming test. *J Mater Process Technol*. 2008;205(1-3):81-88.

2. Miller WS, Zhuang L, Bottema J, et al. Recent development in aluminium alloys for the automotive industry. *Materials Science and Engineering: A*. 2000;280(1):37-49.

3. Kim D, Lee W, Kim J, et al. Macro-performance evaluation of friction stir welded automotive tailor-welded blank sheets: Part II--Formability. *Int J Solids Struct*. 2010;47(7-8):1063-1081.

4. Choi HS, Ko DC, Kim BM. Effect of Weld Line Orientation on Formability of Tailor Welded Blank of 22MnB5 at Elevated Temperature. *Advances in Mechanical Engineering (Hindawi Publishing Corporation)*. Published online 2014.

5. Pastor M, Zhao H, Martukanitz RP, DebRoy T, others. Porosity, underfill and magnesium lose during continuous wave Nd: YAG laser welding of thin plates of aluminum alloys 5182 and 5754. *Welding Journal-New York-*. 1999;78:207--s.

6. Leitao C, Em'ilio B, Chaparro BM, Rodrigues DM. Formability of similar and dissimilar friction stir welded AA 5182-H111 and AA 6016-T4 tailored blanks. *Mater Des*. 2009;30(8):3235-3242.

7. Sato YS, Sugiura Y, Shoji Y, Park SHC, Kokawa H, Ikeda K. Post-weld formability of friction stir welded Al alloy 5052. *Materials Science and Engineering: A*. 2004;369(1-2):138-143.

8. Schubert E, Klassen M, Zerner I, Walz C, Sepold G. Light-weight structures produced by laser beam joining for future applications in automobile and aerospace industry. *J*

Mater Process Technol. 2001;115(1):2-8. doi:https://doi.org/10.1016/S0924-0136(01)00756-7

9. Rath W. CO2 Laser--Workhorse for Industrial Manufacturing: Flexible, reliable and well proven tool for a large variety of laser processing systems. *Laser Technik Journal*. 2009;6(3):32-38.

10. Behler K, Berkmanns J, Ehrhardt A, Frohn W. Laser beam welding of low weight materials and structures. *Mater Des*. 1997;18(4):261-267. doi:https://doi.org/10.1016/S0261-3069(97)00085-X

11. Kashaev N, Ventzke V, Çam G. Prospects of laser beam welding and friction stir welding processes for aluminum airframe structural applications. *J Manuf Process*. 2018;36:571-600. doi:10.1016/J.JMAPRO.2018.10.005

12. Verhaeghe G. Laser welding automotive steel and aluminium. In: *Make It with LasersTM Workshop*. ; 2000.

13. Katayama S. *Handbook of Laser Welding Technologies*. Elsevier; 2013.

14. Badini C, Pavese M, Fino P, Biamino S. Laser beam welding of dissimilar aluminium alloys of 2000 and 7000 series: effect of post-welding thermal treatments on T joint strength. *Science and Technology of Welding and Joining*. 2009;14(6):484-492.

15. Oladimeji OO, Taban E. Trend and innovations in laser beam welding of wrought aluminum alloys. *Welding in the World 2016 60:3*. 2016;60(3):415-457. doi:10.1007/S40194-016-0317-9

16. Alfieria V, Caiazzoa F, Sergi V. Autogenous laser welding of AA 2024 aluminium alloy: process issues and bead features. *Procedia CIRP*. 2015;33:406-411.

17. Ahn J, Chen L, He E, Davies CM, Dear JP. Effect of filler metal feed rate and composition on microstructure and mechanical properties of fibre laser welded AA 2024-T3. *J Manuf Process*. 2017;25:26-36.

18. Enz J, Khomenko V, Riekehr S, Ventzke V, Huber N, Kashaev N. Single-sided laser beam welding of a dissimilar AA2024--AA7050 T-joint. *Mater Des*. 2015;76:110-116.

19. Wang L, Wei Y, Zhao W, Zhan X, She L. Effects of welding parameters on microstructures and mechanical properties of disk laser beam welded 2A14-T6 aluminum alloy joint. *J Manuf Process*. 2018;31:240-246.

20. Daneshpour S, Koçak M, Langlade S, Horstmann M. Effect of overload on fatigue crack retardation of aerospace Al-alloy laser welds using crack-tip plasticity analysis. *Int J Fatigue*. 2009;31(10):1603-1612.

21. Viscusi A, Leitão C, Rodrigues DM, Scherillo F, Squillace A, Carrino L. Laser beam welded joints of dissimilar heat treatable aluminium alloys. *J Mater Process Technol*. 2016;236:48-55.

22. Kashaev N, Chupakhin S, Enz J, et al. Fatigue and fatigue crack propagation of laser beam-welded AA2198 joints and integral structures. In: *Advanced Materials Research*. Vol 891. ; 2014:1457-1462.

23. Kashaev N, Riekehr S, Erdmann K, et al. Fracture mechanical behaviour of laser beam-welded AA2198 butt joints and integral structures. *International Journal of Structural Integrity*. Published online 2015.

24. Enz J, Riekehr S, Ventzke V, Kashaev N, Huber N. Process optimisation for the laser beam welding of high-strength aluminium-lithium alloys. *Schweißen und Schneiden*. 2012;64(8):482-485.

25. Enz J, Riekehr S, Ventzke V, Kashaev N. Influence of the local chemical composition on the mechanical properties of laser beam welded Al-Li alloys. *Phys Procedia*. 2012;39:51-58.

26. NVvL E, Fokkerweg A. 5th CEAS Air \& Space conference Challenges in European aerospace. *Delft University of Technology*. 2015;7:11.

27. Zhang X, Huang T, Yang W, Xiao R, Liu Z, Li L. Microstructure and mechanical properties of laser beam-welded AA2060 Al-Li alloy. *J Mater Process Technol*. 2016;237:301-308.

28. Zhang X, Yang W, Xiao R. Microstructure and mechanical properties of laser beam welded Al--Li alloy 2060 with Al--Mg filler wire. *Mater Des*. 2015;88:446-450.

29. Han B, Tao W, Chen Y, Li H. Double-sided laser beam welded T-joints for aluminum-lithium alloy aircraft fuselage panels: Effects of filler elements on microstructure and mechanical properties. *Opt Laser Technol*. 2017;93:99-108.

30. Ning J, Zhang L jie, Bai Q lin, Yin X qing, Niu J, Zhang J xun. Comparison of the microstructure and mechanical performance of 2A97 Al-Li alloy joints between autogenous and non-autogenous laser welding. *Mater Des*. 2017;120:144-156.

31. Fu B, Qin G, Meng X, Ji Y, Zou Y, Lei Z. Microstructure and mechanical properties of newly developed aluminum--lithium alloy 2A97 welded by fiber laser. *Materials Science and Engineering: A*. 2014;617:1-11.

32. Yan J, Gao M, Li G, Zhang C, Zeng X, Jiang M. Microstructure and mechanical properties of laser-MIG hybrid welding of 1420 Al-Li alloy. *The International Journal of Advanced Manufacturing Technology*. 2013;66(9-12):1467-1473.

33. Braun R. Nd: YAG laser butt welding of AA6013 using silicon and magnesium containing filler powders. *Materials Science and Engineering: A*. 2006;426(1-2):250-262.

34. Oliveira AC, Siqueira RHM, Riva R, Lima MSF. One-sided laser beam welding of autogenous T-joints for 6013-T4 aluminium alloy. *Materials \& Design (1980-2015)*. 2015;65:726-736.

35. Fabrègue D, Deschamps A, Suéry M. Influence of the silicon content on the mechanical properties of AA6xxx laser welds. *Materials Science and Engineering: A*. 2009;506(1-2):157-164.

36. Pakdil M, Çam G, Koçak M, Erim S. Microstructural and mechanical characterization of laser beam welded AA6056 Al-alloy. *Materials Science and Engineering: A*. 2011;528(24):7350-7356.

37. Zhang H, Wang M, Zhang X, Yang G. Microstructural characteristics and mechanical properties of bobbin tool friction stir welded 2A14-T6 aluminum alloy. *Materials \& Design (1980-2015)*. 2015;65:559-566.

38. Enz J, Kumar M, Riekehr S, Ventzke V, Huber N, Kashaev N. Mechanical properties of laser beam welded similar and dissimilar aluminum alloys. *J Manuf Process*. 2017;29:272-280.

39. Becker MN. Aluminum: New challenges in downstream activities. *JOM*. 1999;51(11):26-38.

40. Roth R, Clark J, Kelkar A. Automobile bodies: can aluminum be an economical alternative to steel? *Jom*. 2001;53(8):28-32.

41. Muraoka Y, Miyaoka H. Development of an all-aluminum automotive body. *J Mater Process Technol*. 1993;38(4):655-674.

42. Ito K, Kobayashi H. Production and fabrication technology development of aluminum useful for automobile lightweighting. *Adv Eng Mater*. 2006;8(9):828-835.

43. Dieffenbach JR. Not the Delorean Revisited: An Assessment of the Competitive Position of a Stainless Steel Body-in-White. In: *International Body Engineering Conference \& Exposition*. ; 1998.

44. Graham MP, Hirak DM, Kerr HW, Weckman DC. Nd: YAG laser welding of coated sheet steel. *J Laser Appl*. 1994;6(4):212-222.

45. Chen G, Mei L, Zhang M, Zhang Y, Wang Z. Research on key influence factors of laser overlap welding of automobile body galvanized steel. *Opt Laser Technol*. 2013;45:726-733.

46. Gu H. Laser lap welding of zinc coated steel sheet with laser-dimple technology. *J Laser Appl*. 2010;22(3):87-91.

47. Bley H, Weyand L, Luft A. An alternative approach for the cost-efficient laser welding of zinc-coated sheet metal. *CIRP annals*. 2007;56(1):17-20.

48. Pieters R, Bakels JG, Hermans MJM, Den Ouden G. Laser welding of zinc coated steels in an edge lap configuration. *J Laser Appl*. 2006;18(3):199-204.

49. Chen W, Ackerson P, Molian P. CO2 laser welding of galvanized steel sheets using vent holes. *Mater Des*. 2009;30(2):245-251.

50. Iqbal S, Gualini MMS, ur Rehman A. Dual beam method for laser welding of galvanized steel: Experimentation and prospects. *Opt Laser Technol*. 2010;42(1):93-98.

51. Dasgupta A, Mazumder J. A novel method for lap welding of automotive sheet steel using high power CW CO2 laser. In: *Proceedings of the 4th International Congress on Laser Advanced Materials Processing*. ; 2006:1-5.

52. Li X, Lawson S, Zhou Y, Goodwin F. Novel technique for laser lap welding of zinc coated sheet steels. *J Laser Appl*. 2007;19(4):259-264.

53. Tzeng YF, Chen FC. Effects of Operating Parameters on the Static Properties ofPulsed Laser Welded Zinc-Coated Steel. *The International Journal of Advanced Manufacturing Technology*. 2001;18(9):641-647.

54. Yih-fong T. Gap-free lap welding of zinc-coated steel using pulsed CO 2 laser. *The International Journal of Advanced Manufacturing Technology*. 2006;29(3):287-295.

55. Davis JR, others. *Aluminum and Aluminum Alloys*. ASM international; 1993.

56. Kim DHJWJ. Warm Temperature Deformation Behavior and Processing Maps of 5182 and 7075 Aluminum Alloy Sheets with Fine Grains. *Metals and Materials International*. 2018;24(3):455-463. doi:10.1007/s12540-018-0061-3

57. Li D, Ghosh AK. Effects of temperature and blank holding force on biaxial forming behavior of aluminum sheet alloys. *J Mater Eng Perform*. 2004;13(3):348-360.

58. Li D, Ghosh A. Tensile deformation behavior of aluminum alloys at warm forming temperatures. *Materials Science and Engineering: A*. 2003;352(1-2):279-286.

59. Ozturk F, Toros S, Kilic S. Tensile deformation behavior of AA5083-H111 at cold and warm temperatures. 2010;101.

60. Ghosh M, Miroux A, Kestens LAI. Experimental study and modelling of the role of solutes, precipitates and temperature on the work-hardening of AA6xxx aluminium alloys. *Materials Science and Engineering: A*. 2021;805:140615.

61. Ghosh M, Miroux A, Sidor J, Kestens L. Deformation textures and plastic anisotropy of AA6XXX at warm temperature. In: *Symposium on Aluminum Alloys-Fabrication, Characterization and Applications*. ; 2009:101-106.

62. Morris LR, George RA. *Warm Forming High-Strength Aluminum Automotive Parts*.; 1977.

63. Ayres RA, Lanning HW, Taylor B, Heimbuch R, Brazier WG. Warm forming the GM V-6 oil pan in aluminum. *SAE Transactions*. Published online 1978:702-706.

64. Andrews T, Roberts WT, Rodrigues PMB, Wilson D V. Aluminum Technology'86. *Institute of Metals, London*. Published online 1986:581.

65. Chan KS, Koss DA, Ghosh AK. Localized necking of sheet at negative minor strains. *Metallurgical Transactions A*. 1984;15(2):323-329.

66. Burford DA, Narasimhan K, Wagoner RH. A theoretical sensitivity analysis for full-dome formability tests: parameter study forn, m, r, and $μ$. *Metallurgical Transactions A*. 1991;22(8):1775-1788.

67. Li L, Peng G, Wang J, Gong J, Meng S. Numerical and experimental study on keyhole and melt flow dynamics during laser welding of aluminium alloys under subatmospheric pressures. *Int J Heat Mass Transf*. 2019;133:812-826. doi:10.1016/J.IJHEATMASSTRANSFER.2018.12.165

68. El-Batahgy A, Kutsuna M. Laser beam welding of AA5052, AA5083, and AA6061 aluminum alloys. *Advances in Materials Science and Engineering*. 2009;2009. doi:10.1155/2009/974182

69. Ahn J, Chen L, He E, Dear JP, Davies CM. Optimisation of process parameters and weld shape of high power Yb-fibre laser welded 2024-T3 aluminium alloy. *J Manuf Process*. 2018;34:70-85. doi:10.1016/J.JMAPRO.2018.05.028

70. Benedyk JC. Aluminum alloys for lightweight automotive structures. *Materials, Design and Manufacturing for Lightweight Vehicles*. Published online January 1, 2010:79-113. doi:10.1533/9781845697822.1.79

71. Sun X, Han X, Dong C, Li X. Applications of Aluminum Alloys in Rail Transportation. In: *Advanced Aluminium Composites and Alloys*. IntechOpen; 2021:251-268. doi:10.5772/intechopen.96442

72. Yang YS, Lee SH. A study on the joining strength of laser spot welding for automotive applications. *J Mater Process Technol*. 1999;94(2-3):151-156. doi:10.1016/S0924-0136(99)00094-1

73. Cao X, Wallace W, Poon C, Immarigeon JP. Research and Progress in Laser Welding of Wrought Aluminum Alloys. I. Laser Welding Processes. *Materials and Manufacturing Processes*. 2003;18(1):1-22. doi:10.1081/amp-120017586

74. Wang L, Gao M, Zhang C, Zeng X. Effect of beam oscillating pattern on weld characterization of laser welding of AA6061-T6 aluminum alloy. *Mater Des*. 2016;108:707-717. doi:10.1016/J.MATDES.2016.07.053

75. Geng S, Jiang P, Guo L, Gao X, Mi G. Multi-scale simulation of grain/sub-grain structure evolution during solidification in laser welding of aluminum alloys. *Int J Heat Mass Transf*. 2020;149:119252. doi:10.1016/J.IJHEATMASSTRANSFER.2019.119252

76. Park YW, Rhee S. Process modeling and parameter optimization using neural network and genetic algorithms for aluminum laser welding automation. *The International Journal of Advanced Manufacturing Technology 2007 37:9*. 2007;37(9):1014-1021. doi:10.1007/S00170-007-1039-3

77. Miyagi M, Wang H, Yoshida R, Kawahito Y, Kawakami H, Shoubu T. Effect of alloy element on weld pool dynamics in laser welding of aluminum alloys. *Scientific Reports 2018 8:1*. 2018;8(1):1-10. doi:10.1038/s41598-018-31350-4

78. Niu J, Pan L, Wang M, Fu C, Meng X. Research on laser welding of aluminum matrix composite SiCw/6061. *Vacuum*. 2006;80(11-12):1396-1399. doi:10.1016/J.VACUUM.2006.01.023

79. Sokoluk M, Cao C, Pan S, Li X. Nanoparticle-enabled phase control for arc welding of unweldable aluminum alloy 7075. *Nature Communications 2019 10:1*. 2019;10(1):1-8. doi:10.1038/s41467-018-07989-y

80. Zheng T, Pan S, Liu J, et al. Study on nano-treating of Al-Mg-Si-Cu alloys with TiC nanoparticles. *J Alloys Compd*. 2023;947:169405. doi:10.1016/J.JALLCOM.2023.169405

81. Chen GC, Li X. Effect of TiC Nano-treating on the Fluidity and Solidification Behavior of Aluminum Alloy 6063. *J Mater Process Technol*. Published online November 29, 2023:118241. doi:10.1016/J.JMATPROTEC.2023.118241

82. Sokoluk M, Yuan J, Pan S, Li X. Nanoparticles Enabled Mechanism for Hot Cracking Elimination in Aluminum Alloys. *Metallurgical and Materials Transactions A*. 2021;52(7):3083-3096. doi:10.1007/s11661-021-06302-9

83. Cunningham R, Zhao C, Parab N, et al. Keyhole threshold and morphology in laser melting revealed by ultrahigh-speed x-ray imaging. *Science (1979)*. 2019;363(6429):849-852.

84. Arya PK, Kumar V, Sathiaraj D, Palani IA, Jain NK. Microstructural and Mechanical Properties Analysis of Fibre Laser Welding of Dissimilar AA6061 and AA2024 Aluminium Alloy. In: *Lecture Notes in Mechanical Engineering*. Springer Science and Business Media Deutschland GmbH; 2022:681-688. doi:10.1007/978-981-16-7787-8_55

85. Li Y, Xiong M, He Y, Xiong J, Tian X, Mativenga P. Multi-objective optimization of laser welding process parameters: The trade-offs between energy consumption and welding quality. *Opt Laser Technol*. 2022;149:107861. doi:10.1016/J.OPTLASTEC.2022.107861

86. Idriss M, Mirakhorli F, Desrochers A, Maslouhi A. Overlap laser welding of 5052-H36 aluminum alloy: experimental investigation of process parameters and mechanical designs. *The International Journal of Advanced Manufacturing Technology*. 2022;119(11-12):7653-7667. doi:10.1007/s00170-022-08783-3

87. Hou J, Li R, Xu C, Li T, Shi Z. A comparative study on microstructure and properties of pulsed laser welding and continuous laser welding of Al-25Si-4Cu-Mg high silicon aluminum alloy. *J Manuf Process*. 2021;68:657-667. doi:10.1016/J.JMAPRO.2021.05.064

88. Kim J, Lim H, Cho J, Kim C. Weldability during the laser lap welding of Al 5052 sheets. *Archives of Materials Science and Engineering*. 2008;31(2):113-116. Accessed October 11, 2022.

89. Abioye TE, Mustar N, Zuhailawati H, Suhaina I. Prediction of the tensile strength of aluminium alloy 5052-H32 fibre laser weldments using regression analysis. *International Journal of Advanced Manufacturing Technology*. 2019;102(5-8):1951-1962. doi:10.1007/S00170-019-03310-3

90. Ramiarison H, Barka N, Amira S. Optimization of parameters in laser welding of aluminum alloy 5052-H32 using beam oscillation technique for mechanical performance improvement. *International Journal of Lightweight Materials and Manufacture*. 2022;5(4):470-483. doi:10.1016/J.IJLMM.2022.05.006

91. Gook S, Üstündağ Ö, Gumenyuk A, Rethmeier M. Avoidance of end crater imperfections at high-power laser beam welding of closed circumferential welds. *Welding in the World*. 2020;64(2):407-417. doi:10.1007/S40194-019-00841-X

92. Broitman E. Indentation Hardness Measurements at Macro-, Micro-, and Nanoscale: A Critical Overview. *Tribol Lett*. 2017;65(1):23. doi:10.1007/s11249-016-0805-5

93. American National Standards Institute. *Standard Practice for Instrumented Indentation Testing (ASTM E2546-07)*.; 2007.

94. Sattarpanah Karganroudi S, Feujofack Kemda VB, Barka N. A novel method of identifying porosity during laser welding of galvanized steels using microhardness pattern matrix. *Manuf Lett*. 2020;25:98-101. doi:10.1016/J.MFGLET.2020.08.008

95. American National Standards Institute. *Standard Test Methods for Tension Testing Wrought and Cast Aluminum- and Magnesium-Alloy Products (ASTM B557-15)*.; 2015.

96. The American Society Of Mechanical Engineers - ASME. *ASME B&PV Code: Section VIll, Division 1, Design & Fabrication of Pressure Vessels*.

97. Cabibbo M, Forcellese A, Simoncini M, Pieralisi M, Ciccarelli D. Effect of welding motion and pre-/post-annealing of friction stir welded AA5754 joints. *Mater Des*. 2016;93:146-159. doi:10.1016/J.MATDES.2015.12.099

98. Sathish T, Sevvel P, Sudharsan P, Vijayan V. Investigation and optimization of laser welding process parameters for AA7068 aluminium alloy butt joint. *Mater Today Proc*. 2021;37(Part 2):1672-1677. doi:10.1016/J.MATPR.2020.07.196

99. *ISO 13919-2:2021 - Electron and Laser-Beam Welded Joints — Requirements and Recommendations on Quality Levels for Imperfections — Part 2: Aluminium, Magnesium and Their Alloys and Pure Copper*. 2nd ed.; 2021. Accessed October 12, 2022.

100. Schaefer M, Kessler S, Fetzer F, Graf T. Influence of the focal position on the melt flow during laser welding of steel. *J Laser Appl*. 2017;29(1):12010. doi:10.2351/1.4972098/222477

101. Zhao H, Niu W, Zhang B, Lei Y, Kodama M, Ishide T. Modelling of keyhole dynamics and porosity formation considering the adaptive keyhole shape and three-phase coupling during deep-penetration laser welding. *J Phys D Appl Phys*. 2011;44(48):485302. doi:10.1088/0022-3727/44/48/485302

102. Kumar NMS, Pramod GK, Samrat P, Sadashiva M. A critical review on heat treatment of aluminium alloys. *Mater Today Proc*. 2022;58:71-79.

103. Li Z, Zhang Z, Zhou G, Zhao P, Jia Z, Poole WJ. The effect of Mg and Si content on the microstructure, texture and bendability of Al–Mg–Si alloys. *Materials Science and Engineering: A*. 2021;814:141199.

104. You DY, Gao XD, Katayama S. Review of laser welding monitoring. *Science and technology of welding and joining*. 2014;19(3):181-201.

105. Ko DC, Ko DH, Kim JH, Park JH. Development of a partition panel of an Al6061 sheet metal part for the improvement of formability and mechanical properties by hot forming quenching. *Advances in Mechanical Engineering*. 2017;9(2):1687814017691213.

106. Narsimhachary D, Bathe RN, Padmanabham G, Basu A. Influence of temperature profile during laser welding of aluminum alloy 6061 T6 on microstructure and mechanical properties. *Materials and Manufacturing Processes*. 2014;29(8):948-953.

107. Fan C, Yang S lei, Duan C feng, Zhu M qi, Bai Y shan. Microstructure and mechanical properties of 6061 aluminum alloy laser-MIG hybrid welding joint. *J Cent South Univ*. 2022;29(3):898-911.

108. Chu Q, Bai R, Jian H, Lei Z, Hu N, Yan C. Microstructure, texture and mechanical properties of 6061 aluminum laser beam welded joints. *Mater Charact*. 2018;137:269-276.

109. Sun T, Franciosa P, Sokolov M, Ceglarek D. Challenges and opportunities in laser welding of 6xxx high strength aluminium extrusions in automotive battery tray construction. *Procedia CIRP*. 2020;94:565-570. doi:10.1016/J.PROCIR.2020.09.076

110. Wang L, Gao M, Zhang C, Zeng X. Effect of beam oscillating pattern on weld characterization of laser welding of AA6061-T6 aluminum alloy. *Mater Des*. 2016;108:707-717. doi:10.1016/J.MATDES.2016.07.053

111. Chu Q, Bai R, Jian H, Lei Z, Hu N, Yan C. Microstructure, texture and mechanical properties of 6061 aluminum laser beam welded joints. *Mater Charact*. 2018;137:269-276. doi:10.1016/J.MATCHAR.2018.01.030

112. Deng A, Chen H, Zhang Y, et al. Prediction of the influence of welding metal composition on solidification cracking of laser welded aluminum alloy. *Mater Today Commun*. 2023;35:105556. doi:10.1016/J.MTCOMM.2023.105556

113. Karami S, Yousefieh M, Naffakh-Moosavy H. The effect of laser welding parameters on mechanical properties and microstructure evolution of multi-layered 6061 aluminum alloy. *Journal of Advanced Joining Processes*. 2025;11:100275. doi:10.1016/J.JAJP.2024.100275

114. Rakhi K, Kang S, Shin J. Hot-Cracking Mechanism of Laser Welding of Aluminum Alloy 6061 in Lap Joint Configuration. *Materials 2023, Vol 16, Page 6426*. 2023;16(19):6426. doi:10.3390/MA16196426

115. Su C, Zhou JZ, Ye YX, Huang S, Meng XK. Study on Fiber Laser Welding of AA6061-T6 Samples through Numerical Simulation and Experiments. *Procedia Eng*. 2017;174:732-739. doi:10.1016/J.PROENG.2017.01.213

116. Kim YG, Kim MH, Joo SM. Experimental Investigation on the Laser Welding Characteristics of 6061-T6 Aluminum Alloy Sheets. *Mater Trans*. 2018;59(9):1446-1451. doi:10.2320/MATERTRANS.M2018048

117. Kang Y, Zhan X, He S, Liu T, Sun L. Porosity-grain growth relationships in the laser beam deep penetration welding of 6061 aluminum alloy. *J Adhes Sci Technol*. 2021;35(13):1372-1392. doi:10.1080/01694243.2020.1844970

118. Miyagi M, Wang H, Yoshida R, Kawahito Y, Kawakami H, Shoubu T. Effect of alloy element on weld pool dynamics in laser welding of aluminum alloys. *Scientific Reports 2018 8:1*. 2018;8(1):1-10. doi:10.1038/s41598-018-31350-4

119. Yang Z, Tao W, Li L, Chen Y, Shi C. Numerical simulation of heat transfer and fluid flow during double-sided laser beam welding of T-joints for aluminum aircraft fuselage panels. *Opt Laser Technol*. 2017;91:120-129. doi:10.1016/J.OPTLASTEC.2016.12.018

120. Yang Z, Zhao X, Tao W, et al. Comparative study on successive and simultaneous double-sided laser beam welding of AA6056/AA6156 aluminum alloy T-joints for

aircraft fuselage panels. *International Journal of Advanced Manufacturing Technology*. 2018;97(1-4):845-856. doi:10.1007/S00170-018-1996-8/METRICS

121. Yang Z, Zhao X, Tao W, Jin C. Effects of keyhole status on melt flow and flow-induced porosity formation during double-sided laser welding of AA6056/AA6156 aluminium alloy T-joint. *Opt Laser Technol*. 2019;109:39-48. doi:10.1016/J.OPTLASTEC.2018.07.065

122. Han B, Tao W, Chen Y. New technique of skin embedded wire double-sided laser beam welding. *Opt Laser Technol*. 2017;91:185-192. doi:10.1016/J.OPTLASTEC.2016.12.023

123. Qi N, Wang L, Zhao Y, Tian S, Zhan X. The tensile properties of 2219 aluminum alloy plate butt joint welded by novel laser mirror welding. *Opt Laser Technol*. 2022;149:107796. doi:10.1016/J.OPTLASTEC.2021.107796

124. Zhang Y, Tao W, Chen Y, Nan T. Effects of heat treatment on microstructure and mechanical properties of double-sided laser-welded AA2060/AA2099 T-Joint. *J Mater Process Technol*. 2020;285:116777. doi:10.1016/J.JMATPROTEC.2020.116777

125. Xia P, Xiong L, Hu Y, Feng X, Wang C. Effect of laser oscillation and beam incident angle on porosity in double-sided filler welding of 2219 aluminum alloy T joint. *Opt Laser Technol*. 2023;166:109581. doi:10.1016/J.OPTLASTEC.2023.109581

126. Narsimhachary D. *Effect of Laser Welding Parameters on 6061 Aluminium Alloy*. 2014.

127. Han B, Tao W, Chen Y, Li H. Double-sided laser beam welded T-joints for aluminum-lithium alloy aircraft fuselage panels: Effects of filler elements on microstructure and mechanical properties. *Opt Laser Technol*. 2017;93:99-108.

128. Li M, Li Z, Zhao Y, Li H, Wang Y, Huang J. Influence of welding parameters on weld formation and microstructure of dual-laser beams welded T-joint of aluminum alloy. *Advances in Materials Science and Engineering*. 2011;2011.

129. Yang ZB, Tao W, Li LQ, Chen YB, Li FZ, Zhang YL. Double-sided laser beam welded T-joints for aluminum aircraft fuselage panels: Process, microstructure, and mechanical properties. *Mater Des*. 2012;33:652-658.

130. Kermanidis AT, Tzamtzis A. An experimental approach for estimating the effect of heat affected zone (HAZ) microstructural gradient on fatigue crack growth rate in aluminum alloy FSW. *Materials Science and Engineering: A*. 2017;691:110-120.

131. Bussu G, Irving PE. The role of residual stress and heat affected zone properties on fatigue crack propagation in friction stir welded 2024-T351 aluminium joints. *Int J Fatigue*. 2003;25(1):77-88.

132. Janasekaran S, Fadzil Jamaludin M, Ridha Muhamad M, Yusof F, Hamdi Abdul Shukor M. Autogenous double-sided T-joint welding on aluminum alloys using low power fiber laser. *SpringerS Janasekaran, MF Jamaludin, MR Muhamad, F Yusof, MH Abdul ShukorThe International Journal of Advanced Manufacturing Technology, 2017•Springer*. 2017;90(9-12):3497-3505. doi:10.1007/s00170-016-9677-y

133. Farhadipour P, Omidi N, Barka N, Nadeau F, Idriss M, Ouafi A El. Systematic approach to improve overlap laser welding of AA5052-H32 with dissimilar thickness by evaluation of mechanical performance, undercut, and welding penetration. *The International Journal of Advanced Manufacturing Technology*. Published online 2024:1-13.

134. Farhadipour P, Omidi N, Barka N, Idriss M, Nadeau F, Ouafi A El. Comparative analysis of the high-temperature tensile properties of laser-welded AA5052 and AA6061 for automotive applications. *Proc Inst Mech Eng C J Mech Eng Sci*. Published online March 3, 2024. doi:10.1177/09544062251321757

135. American National Standards Institute. *Standard Test Methods for Tension Testing Wrought and Cast Aluminum- and Magnesium-Alloy Products (ASTM B557-15)*.; 2015. doi:10.1520/B0557-15R23

136. Vyskoč M, Sahul M, Dománková M, et al. The effect of process parameters on the microstructure and mechanical properties of AW5083 aluminum laser weld joints. *Metals (Basel)*. 2020;10(11):1443.

137. Chen L, Wang C, Xiong L, Zhang X, Mi G. Microstructural, porosity and mechanical properties of lap joint laser welding for 5182 and 6061 dissimilar aluminum alloys under different place configurations. *Mater Des*. 2020;191:108625.

138. Beiranvand ZM, Ghaini FM, Naffakh-Moosavy H, Sheikhi M, Torkamany MJ. Magnesium loss in Nd: YAG pulsed laser welding of aluminum alloys. *Metallurgical and materials transactions B*. 2018;49:2896-2905.

139. Zhou L, Zhang M, Jin X, Zhang H, Mao C. Study on the burning loss of magnesium in fiber laser welding of an Al-Mg alloy by optical emission spectroscopy. *The International Journal of Advanced Manufacturing Technology*. 2017;88:1373-1381.

140. Blake A, Mazumder J. Control of magnesium loss during laser welding of Al-5083 using a plasma suppression technique. Published online 1985.

141. Cao X, Jahazi M, Immarigeon JP, Wallace W. A review of laser welding techniques for magnesium alloys. *J Mater Process Technol*. 2006;171(2):188-204. doi:10.1016/j.jmatprotec.2005.06.068

142. Beiranvand ZM, Ghaini FM, Moosavy HN, Sheikhi M, Torkamany MJ, Moradi M. The relation between magnesium evaporation and laser absorption and weld penetration in pulsed laser welding of aluminum alloys: Experimental and numerical investigations. *Opt Laser Technol*. 2020;128:106170.

143. Cieslak MJ, Fuerschbach PW. On the weldability, composition, and hardness of pulsed and continuous Nd: YAG laser welds in aluminum alloys 6061, 5456, and 5086. *Metallurgical Transactions B*. 1988;19:319-329.

144. Zhao H, Debroy T. Weld metal composition change during conduction mode laser welding of aluminum alloy 5182. *Metallurgical and Materials Transactions B 2001 32:1*. 2001;32(1):163-172. doi:10.1007/S11663-001-0018-6

145. Garcia C, Lotz T, Martinez M, Artemev A, Alderliesten R, Benedictus R. Fatigue crack growth in residual stress fields. *Int J Fatigue*. 2016;87:326-338.

146. Colegrove P, Ikeagu C, Thistlethwaite A, et al. Welding process impact on residual stress and distortion. *Science and Technology of Welding and Joining*. 2009;14(8):717-725. doi:10.1179/136217109X406938

147. De A, DebRoy T. A perspective on residual stresses in welding. *Science and Technology of Welding and Joining*. 2011;16(3):204-208. doi:10.1179/136217111X12978476537783

148. LI Y, GAN W, ZHOU W, LI D. Review on residual stress and its effects on manufacturing of aluminium alloy structural panels with typical multi-processes. *Chinese Journal of Aeronautics*. 2023;36(5):96-124. doi:10.1016/J.CJA.2022.07.020

149. Zhao H, Zhang G, Yin Z, Wu L. Three-dimensional finite element analysis of thermal stress in single-pass multi-layer weld-based rapid prototyping. *J Mater Process Technol*. 2012;212(1):276-285. doi:10.1016/J.JMATPROTEC.2011.09.012

150. Rong Y, Huang Y, Wang L. Evolution Mechanism of Transient Strain and Residual Stress Distribution in Al 6061 Laser Welding. *Crystals 2021, Vol 11, Page 205*. 2021;11(2):205. doi:10.3390/CRYST11020205

151. Ivanov SY, Panchenko O V, Mikhailov VG. Comparative analysis of non-uniformity of mechanical properties of welded joints of Al–Mg–Si alloys during friction stir welding and laser welding. *Metal Science and Heat Treatment*. 2018;60:393-398.

152. Liu YL, Kang SB, Kim HW. The complex microstructures in an as-cast Al–Mg–Si alloy. *Mater Lett*. 1999;41(6):267-272.

153. Karpov E V, Malikov AG, Orishich AM, Annin BD. Temperature Effect on the Fracture of Laser Welded Joints of Aviation Aluminum Alloys. *Journal of Applied Mechanics and Technical Physics*. 2018;59:934-940.

154. Roy BK, Korkolis YP, Arai Y, Araki W, Iijima T, Kouyama J. Plastic deformation of AA6061-T6 at elevated temperatures: Experiments and modeling. *Int J Mech Sci*. 2022;216:106943.

155. Davies RG, Magee CL. The effect of strain-rate upon the tensile deformation of materials. Published online 1975.

156. Chen Y, Clausen AH, Hopperstad OS, Langseth M. Stress–strain behaviour of aluminium alloys at a wide range of strain rates. *Int J Solids Struct*. 2009;46(21):3825-3835. doi:10.1016/J.IJSOLSTR.2009.07.013

157. Scapin M, Manes A. Behaviour of Al6061-T6 alloy at different temperatures and strain-rates: Experimental characterization and material modelling. *Materials Science and Engineering: A*. 2018;734:318-328. doi:10.1016/J.MSEA.2018.08.011

158. Carden AE, Williams PE, Karpp RR. Comparison of the Flow Curves of 6061 Aluminum Alloy at High and Low Strain Rates. *Shock Waves and High-Strain-Rate Phenomena in Metals*. Published online 1981:37-50. doi:10.1007/978-1-4613-3219-0_3

159. Fan XH, Li M, Li DY, Shao YC, Zhang SR, Peng YH. Dynamic recrystallisation and dynamic precipitation in AA6061 aluminium alloy during hot deformation. *Materials*

Science and Technology (United Kingdom). 2014;30(11):1263-1272. doi:10.1179/1743284714Y.0000000538

160. Materials MRM of TD, 2019 undefined. Dynamic mechanical characterization of aluminum: Analysis of strain-rate-dependent behavior. *SpringerM RahmatMechanics of Time-Dependent Materials, 2019•Springer*. 2019;23(4):385-405. doi:10.1007/s11043-018-9393-0

161. Dorbane A, Ayoub G, Mansoor B, Hamade R, Kridli G, Imad A. Observations of the mechanical response and evolution of damage of AA 6061-T6 under different strain rates and temperatures. *Materials Science and Engineering: A*. 2015;624:239-249. doi:10.1016/J.MSEA.2014.11.074

162. Hallbäck N, Nilsson F. Mixed-mode I/II fracture behaviour of an aluminium alloy. *J Mech Phys Solids*. 1994;42(9):1345-1374.

163. Ghadmode MM, Sonawane BU, Bhapkar US. Experimental investigation of tailor welded blanks of dissimilar aluminum alloys. *Mater Today Proc*. 2022;56:2785-2793. doi:10.1016/J.MATPR.2021.10.095

164. Bagheri B, Abbasi M, Hamzeloo R. Comparison of different welding methods on mechanical properties and formability behaviors of tailor welded blanks (TWB) made from AA6061 alloys. *Proc Inst Mech Eng C J Mech Eng Sci*. 2021;235(12):2225-2237. doi:10.1177/0954406220952504

165. Basile D, Sesana R, De Maddis M, Borella L, Russo Spena P. Investigation of Strength and Formability of 6016 Aluminum Tailor Welded Blanks. *Metals 2022, Vol 12, Page 1593*. 2022;12(10):1593. doi:10.3390/MET12101593

166. Sun Y. The use of aluminum alloys in structures: Review and outlook. *Structures*. 2023;57:105290. doi:10.1016/J.ISTRUC.2023.105290

167. Perovic A, Perovic DD, Weatherly GC, Lloyd DJ. Precipitation in aluminum alloys AA6111 and AA6016. *Scr Mater*. 1999;41(7):703-708. doi:10.1016/S1359-6462(99)00204-3

168. Hakem M, Lebaili S, Mathieu S, Miroud D, Lebaili A, Cheniti B. Effect of microstructure and precipitation phenomena on the mechanical behavior of AA6061-T6 aluminum alloy weld. *International Journal of Advanced Manufacturing Technology*. 2019;102(9-12):2907-2918. doi:10.1007/S00170-019-03401-1

169. Hillel G, Kalabukhov S, Frage N, Zaretsky E, Meshi L. Direct observation of initial stages of precipitation hardening process in commercial Al 6061 alloy. *J Mater Sci*. 2022;57(22):10395-10406. doi:10.1007/s10853-022-07341-2

170. Wang B, Chen XH, Pan FS, Mao JJ, Fang Y. Effects of cold rolling and heat treatment on microstructure and mechanical properties of AA 5052 aluminum alloy. *Transactions of Nonferrous Metals Society of China*. 2015;25(8):2481-2489. doi:10.1016/S1003-6326(15)63866-3

171. Hirose A, Todaka H, Kobayashi KF. CO2 laser beam welding of 6061-T6 aluminum alloy thin plate. *Metall Mater Trans A Phys Metall Mater Sci*. 1997;28(12):2657-2662. doi:10.1007/S11661-997-0022-9

172. Narsimhachary D, Bathe RN, Padmanabham G, Basu A. Influence of Temperature Profile during Laser Welding of Aluminum Alloy 6061 T6 on Microstructure and Mechanical Properties. *Materials and Manufacturing Processes*. 2014;29(8):948-953. doi:10.1080/10426914.2013.872258

173. Emine Gündoğdu, Topuz P, Akman E, Yilmaz M. Effect of laser welding speed on pore formation in AA 6061 T6 alloy. *Materialpruefung/Materials Testing*. 2020;62(10):979-984. doi:10.3139/120.111573

174. Hirose A, Todaka H, Yamaoka H, Kurosawa N, Kobayashi KF. Quantitative evaluation of softened regions in weld heat-affected zones of 6061-T6 aluminum alloy

- characterizing of the laser beam welding process. *Metall Mater Trans A Phys Metall Mater Sci*. 1999;30(8):2115-2120. doi:10.1007/S11661-999-0022-Z

175. Ramiarison H, Barka N, Pilcher C, Stiles E, Larrimore G, Amira S. Weldability improvement by wobbling technique in high power density laser welding of two aluminum alloys: Al-5052 and Al-6061. *J Laser Appl*. 2021;33(3). doi:10.2351/7.0000353/222591

176. Chen Y, Clausen AH, Hopperstad OS, Langseth M. Stress–strain behaviour of aluminium alloys at a wide range of strain rates. *Int J Solids Struct*. 2009;46(21):3825-3835. doi:10.1016/J.IJSOLSTR.2009.07.013

177. Djapic Oosterkamp L, Ivankovic A, Venizelos G. High strain rate properties of selected aluminium alloys. *Materials Science and Engineering: A*. 2000;278(1-2):225-235. doi:10.1016/S0921-5093(99)00570-5

178. Engler O, Kuhnke K, Westphal K, Hasenclever J. Impact of chromium on the microchemistry evolution during solidification and homogenization of the Al-Mg alloy AA 5052. *J Alloys Compd*. 2018;744:561-573. doi:10.1016/J.JALLCOM.2018.02.125

179. Liu C, Northwood DO, Bhole SD. Tensile fracture behavior in CO2 laser beam welds of 7075-T6 aluminum alloy. *Mater Des*. 2004;25(7):573-577. doi:10.1016/J.MATDES.2004.02.017

180. Shakeri HR, Buste A, Worswick MJ, et al. Study of damage initiation and fracture in aluminum tailor welded blanks made via different welding techniques. *Journal of Light Metals*. 2002;2(2):95-110. doi:10.1016/S1471-5317(02)00028-7

181. Wang GS, Liu K, Wang SL. Evolution of Elevated-Temperature Strength and Creep Resistance during Multi-Step Heat Treatments in Al-Mn-Mg Alloy. *Materials*. 2018;11(7). doi:10.3390/MA11071158

182. Cieslak MJ, Fuerschbach PW. On the weldability, composition, and hardness of pulsed and continuous Nd:YAG laser welds in aluminum alloys 6061,5456, and 5086. *Metallurgical Transactions B*. 1988;19(1):319-329. doi:10.1007/BF02654217

183. Zhan X, Chen J, Liu J, Wei Y, Zhou J, Meng Y. Microstructure and magnesium burning loss behavior of AA6061 electron beam welding joints. *Mater Des*. 2016;99:449-458. doi:10.1016/J.MATDES.2016.03.058

184. Cui M, Zheng Z, Du P, Chang L. A double molten pool laser welding process for joining magnesium alloys and aluminum alloys: The process, microstructure and mechanical properties of joints. *Mater Today Commun*. 2023;35:106116. doi:10.1016/J.MTCOMM.2023.106116

185. Malekshahi Beiranvand Z, Malek Ghaini F, Naffakh Moosavy H, Sheikhi M, Torkamany MJ, Moradi M. The relation between magnesium evaporation and laser absorption and weld penetration in pulsed laser welding of aluminum alloys: Experimental and numerical investigations. *Opt Laser Technol*. 2020;128:106170. doi:10.1016/J.OPTLASTEC.2020.106170

186. Cao X, Jahazi M, Immarigeon JP, Wallace W. A review of laser welding techniques for magnesium alloys. *J Mater Process Technol*. 2006;171(2):188-204. doi:10.1016/J.JMATPROTEC.2005.06.068

187. Cordero ZC, Knight BE, Schuh CA. Six decades of the Hall–Petch effect – a survey of grain-size strengthening studies on pure metals. *International Materials Reviews*. 2016;61(8):495-512. doi:10.1080/09506608.2016.1191808